



UNIVERSITY OF WEST ATTICA

SCHOOL OF ENGINEERING

DEPARTMENT OF NAVAL ARCHITECTURE
DIVISION OF MARINE ENGINEERING

Thesis Diploma

**Assessment of flow energy harvesting in a duct
by means of CFD numerical simulations**

Marios - Vasileios N. Benetatos
15063

Supervisor:

Dimitrios Koubogianis


Athens, March 2023

Approved by the selection board on March 2023.

.....
Dimitrios Koubogiannis
Associate Professor

.....
Theodoros Gerostathis
Associate Professor

.....
Sofia Peppa
Associate Professor



.....
Marios - Vasileios Benetatos
Department of Naval Architecture
University of West Attica

Copyright © Marios - Vasileios Benetatos, 2023
All rights reserved.

Copying is prohibited, storage and distribution of the present work, wholly or in part, for commercial purposes. Reprint is allowed, storage and distribution for non-profit purposes, educational or research nature, provided that the source of origin is indicated and to keep this message. Questions concerning the use of work for profit-making purposes should be addressed to the author. The views and conclusions contained in this document express the author and should not be interpreted as representing the official positions of the University of West Attica.

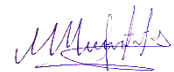
ΔΗΛΩΣΗ ΣΥΓΓΡΑΦΕΑ ΔΙΠΛΩΜΑΤΙΚΗΣ ΕΡΓΑΣΙΑΣ

Ο κάτωθι υπογεγραμμένος Μάριος - Βασίλειος Μπενετάτος του Νικολάου, με αριθμό μητρώου 51115063 φοιτητής του Πανεπιστημίου Δυτικής Αττικής της Σχολής Μηχανικών του Τμήματος Ναυπηγών Μηχανικών, δηλώνω υπεύθυνα ότι:

«Είμαι συγγραφέας αυτής της διπλωματικής εργασίας και ότι κάθε βοήθεια την οποία είχα για την προετοιμασία της είναι πλήρως αναγνωρισμένη και αναφέρεται στην εργασία. Επίσης, οι όποιες πηγές από τις οποίες έκανα χρήση δεδομένων, ιδεών ή λέξεων, είτε ακριβώς είτε παραφρασμένες, αναφέρονται στο σύνολό τους, με πλήρη αναφορά στους συγγραφείς, τον εκδοτικό οίκο ή το περιοδικό, συμπεριλαμβανομένων και των πηγών που ενδεχομένως χρησιμοποιήθηκαν από το διαδίκτυο. Επίσης, βεβαιώνω ότι αυτή η εργασία έχει συγγραφεί από μένα αποκλειστικά και αποτελεί προϊόν πνευματικής ιδιοκτησίας τόσο δικής μου, όσο και του Ιδρύματος.

Παράβαση της ανωτέρω ακαδημαϊκής μου ευθύνης αποτελεί ουσιώδη λόγο για την ανάκληση του διπλώματός μου».

Ο Δηλών



Μάριος Βασίλειος Ν. Μπενετάτος

*”Κι εγώ που ξέχασα ποιος είμαι που πηγαίνω,
λαθρεπιβάτης σ’ ένα πλοίο παροπλισμένο.
Απόψε σ’ άκουσα να λες απ’ τα ηχεία,
για να χαράξεις μες στο πουθενά πορεία,
χόρευε πάνω στο φτερό του καρχαρία.”*
N. Καββαδίας - Α. Αλκαίος

Αφιερώνεται στην αδελφή μου

Acknowledgements

I would like to express my deepest gratitude and appreciation to everyone who has supported me during the course of this thesis. I would like to extend my gratefulness to my advisor, Professor Dimitrios Koubogiannis, for his invaluable guidance, support, and mentorship throughout the entire process. His expert advice, constructive criticism, and unwavering encouragement have been essential for completing this work. I would also like to express my gratitude to Professor Theodoros Gerostathis for his valuable guidance on the LaTeX environment in which the present work has been written.

I would also like to acknowledge the support and encouragement of my colleagues in Argo Navis, all my friends, and especially my parents and my sister for their patience throughout this journey. I would like to thank my family for their unwavering love and support, and for being my rock through the peaks and valleys of this work. I am truly grateful to have them in my life.

This work is the last chapter in the University of West Attica and with the finalization of the current project, a big chapter of my life ends and thus a new one begins. The knowledge and skills acquired during my studies in the Dpt. of Naval Architect–Engineering shall prove to be invaluable assets in my professional endeavors. I am deeply grateful to all of my professors for their dedicated efforts in imparting their knowledge to the next generation of students.

Περίληψη

Οι συσκευές συγκομιδής ενέργειας μικρής κλίμακας (miniature devices), χρησιμοποιούν και μετατρέπουν την ενέργεια που υπάρχει ελεύθερη στο περιβάλλον -προερχόμενη από πηγές όπως το φως ή θερμότητα, οι μηχανικές δονήσεις κ.α.- σε ηλεκτρική ενέργεια που μπορεί να χρησιμοποιηθεί για παροχή ισχύος σε αισθητήρες και ηλεκτρικές μικροσυσκευές. Έχουν προσελκύσει το ενδιαφέρον των ερευνητών από τις αρχές του 21ου αιώνα, λόγω του δυναμικού τους να τροφοδοτούν αυτόνομα και ασύρματα δίκτυα αισθητήρων για πληθώρα βιομηχανικών εφαρμογών και προσφέρουν την δυνατότητα παρακολούθησης πολύπλοκων συστημάτων, ειδικά σε μέρη όπου η ανθρώπινη πρόσβαση είναι δυσχερής.

Οι συσκευές αυτές αποτελούνται συνήθως από έναν μετατροπέα, ο οποίος μετατρέπει την ενέργεια που αντλείται από το περιβάλλον σε ηλεκτρική ενέργεια. Επιπροσθέτως, είναι εφοδιασμένες με ειδικά ηλεκτρικά κυκλώματα διαχείρισης ισχύος, τα οποία είναι υπεύθυνα για τη διανομή της ηλεκτρικής ενέργειας στον εκάστοτε καταναλωτή. Τα τελευταία χρόνια έχουν αναπτυχθεί διάφοροι τύποι μετατροπέων, όπως για παράδειγμα τα φωτοβολταϊκά κύτταρα, οι θερμοηλεκτρικές και πιεζοηλεκτρικές γεννήτριες κ.α. Είναι σαφές ότι ο εκάστοτε από τους προαναφερθέντες τύπους παρουσιάζει τα δικά του πλεονεκτήματα και μειονεκτήματα.

Είναι προφανές ότι ο σχεδιασμός και η βελτιστοποίηση των συσκευών συγκομιδής ενέργειας μικρής κλίμακας, συνεπάγεται πολλές προκλήσεις, όπως ο στόχος για μεγιστοποίηση της απόδοσης, η ελαχιστοποίηση των απωλειών ισχύος, η κατάλληλη εγκατάσταση τους ανάλογα με το περιβάλλον και τις ανάγκες της εκάστοτε εφαρμογής κ.α. Παρόλα αυτά, η ανάπτυξη και ο βέλτιστος σχεδιασμός αυτών των συστημάτων προσφέρουν μια ελπιδοφόρα λύση για την τροφοδότηση συσκευών χαμηλών ενεργειακών απαιτήσεων, με αυτόνομο τρόπο.

Στην παρούσα διπλωματική εργασία μελετάται με αριθμητικές προσομοιώσεις μια συσκευή συγκομιδής ενέργειας, η οποία έχει προταθεί και έχει μελετηθεί πειραματικά στη βιβλιογραφία [26]. Αυτή αποτελείται από δυο τριγωνικά σώματα (bluff bodies), τοποθετημένα σε ένα κανάλι ροής αέρα, και ένα εύκαμπτο διάφραγμα, το οποίο είναι τοποθετημένο στον πάνω τοίχο του καναλιού. Η ροή του αέρα μέσα στο κανάλι δημιουργεί πίσω από τα σώματα έναν δρόμο δινών που με τη σειρά του δημιουργεί μηχανικές ταλαντώσεις / δονήσεις στο εύκαμπτο διάφραγμα. Το διάφραγμα αυτό είναι κατάλληλα συνδεδεμένο με μια πιεζοηλεκτρική μεμβράνη, η οποία μετατρέπει τη μηχανική ενέργεια σε ηλεκτρική μέσω του πιεζοηλεκτρικού φαινομένου. Παρόλο που η κατασκευή και η τοποθέτηση της συγκεκριμένης συσκευής είναι εύκολη, η αποδιδόμενη τελική ισχύς που προσφέρει είναι αρκετά χαμηλή, γεγονός που δικαιολογεί την περαιτέρω ερεύνα. Η ίδια συσκευή είχε μελετηθεί στο παρελθόν από τον Επιβλέποντα της παρούσας διπλωματικής εργασίας [21], όπου και έγινε διερεύνηση για να βρεθεί το βέλτιστο σχήμα και η διάταξη των μη αεροδυναμικών σωμάτων, καταλήγοντας σε δυο σώματα τριγωνικής διατομής. Σε συνέχεια της παραπάνω μελέτης, στην παρούσα εργασία αναπτύσσεται περαιτέρω ένα δισδιάστατο μοντέλο CFD, που βασίζεται σε εμπορικό λογισμικό. Αυτό δοκιμάζεται ως προς την ανεξαρτησία πλέγματος και την επιλογή του χρονικού βήματος. Στη συνέχεια, με χρήση του μοντέλου CFD, όπως διαμορφώνεται πραγματοποιείται μια παραμετρική μελέτη στο μοντέλο προσομοίωσης, για την αξιολόγηση των επιδόσεων της συσκευής. Ως παράμετροι επιλέγονται ο αριθμός Reynolds (διαφορετική ταχύτητα εισόδου του ρευστού στον αγωγό) και τα διαφορετικά μεγέθη τριγώνου σε αναλογία με το ύψος του αγωγού (blockage ratio). Τέλος μελετάται το φαινόμενο της καταστολής δινών στον αγωγό ως συνέπεια αύξησης του blockage ratio και τα αποτελέσματα συγκρίνονται με αντίστοιχα αποτελέσματα της βιβλιογραφίας.

Λέξεις Κλειδιά: υπολογιστική ρευστομηχανική, ενέργεια μικρης κλιμακας, ασύρματα δίκτυα αισθητήρων, μη αεροδυναμικα σωματα, ροη σε αγωγο, πιεζοηλεκτρικο φαινόμενο, μηχανικές δονήσεις, απόρριψη δινών, ηλεκτρική ενέργεια

Abstract

Micro-energy harvesting devices are small-scale devices that convert ambient energy from the environment, such as light, heat, or mechanical vibrations, into electrical energy that can be used to power small electronic devices. These devices have gained increasing attention in recent years due to their potential to power autonomous microsystems, such as wireless sensors and implantable medical devices, without the need for external power sources or batteries.

Micro-energy harvesting devices typically consist of a transducer that converts the ambient energy into electrical energy, a power management circuit that regulates and stores the electrical energy, and an output circuit that delivers the energy to the load. Various types of transducers have been developed, including photovoltaic cells, thermoelectric generators, and piezoelectric generators, each of which has its own advantages and limitations.

The design and optimization of micro-energy harvesting devices involve many challenges, such as maximizing the energy conversion efficiency, minimizing the power losses, and ensuring the compatibility between the transducer and the load. Nonetheless, micro-energy harvesting devices offer a promising solution for powering low-power electronics in a sustainable and self-sufficient manner, and their development is expected to have a significant impact on a wide range of applications in the future.

A miniature device, harvesting energy from the flow in a micro-channel that has been proposed and experimentally studied in the literature, is numerically studied herein. The device consists of two bluff bodies installed in the flow and a flexible diaphragm at the channel upper wall, above the bodies. Vortex shedding behind the bodies induces pressure fluctuation and causes vibration of the diaphragm; the latter is connected to a piezoelectric membrane converting mechanical energy to electrical. Although the device is easy to fabricate and install, its power output is low, justifying further research. This device has been numerically studied in the past in [21], where various bluff body shapes and configurations had been considered for a fixed inlet Reynolds number and conclusions were drawn concerning the more effective configuration with respect to body geometry and diaphragm position. The above study is continued herein by further testing the CFD model for various grid sizes and assessing the device performance for various flow Reynolds numbers, and various blockage ratios. Additionally, the vortex shedding suppression in the device is studied, and the results are compared with the bibliography outcomes for the same device.

Keywords: Computational Fluid Dynamics (CFD), Navier Stokes equation (NS), Reynolds Average Navier Stokes (RANS), k-epsilon turbulence model, micro energy harvesting, Wireless Sensor Networks (WSN), Piezoelectric Energy Harvesting (PEH), Von-Karman vortex street, Vortex-Induced Vibrations (VIV), flow past bluff bodies, electrical energy

Contents

Acknowledgements	iii
Περίληψη	v
Abstract	vii
Contents	x
List of Figures	xiv
List of Tables	xv
1 Introduction	1
1.1 Motivation	1
1.2 Wireless sensor networks	2
1.2.1 Architecture of Wireless Sensor Network	2
1.2.2 Architecture of Wireless Sensor Nodes in Wireless Sensor Network	4
1.2.3 Wireless Sensor Networks applications	5
1.2.4 Problems in powering the Wireless Sensor Network	7
1.3 Overview of energy harvesting systems - Sources of microenergy harvesting	8
1.3.1 Mechanical Energy Harvesting	10
1.3.2 Dynamic Fluid Energy Harvesting	12
1.4 Piezoelectric Phenomenon and Piezoelectric Energy Harvesters (PEH)	14
1.4.1 Piezoelectric Phenomenon	14
1.4.2 Piezoelectric Energy Harvesters	15
1.5 Karman vortex street and vortex-induced vibrations (VIV)	18
1.6 Energy harvesting techniques using bluff bodies - Literature review	20
1.7 Thesis outline	30
2 Theoretical framework: Governing Equations and Computational Fluid Dynamics	31
2.1 Governing Equations	33
2.1.1 Conservation of mass: Continuity Equation	33
2.1.2 Conservation of momentum: Navier Stokes momentum equation	34
2.2 Computational Fluid Dynamics	36
2.2.1 Reynolds averaged Navier Stokes Equations (RaNS)	36
2.2.2 Turbulence modeling	37
2.2.3 Computational grids	37
2.2.4 Spatial discretization methods	38
2.2.5 Time discretization methods	40
2.3 Definition of Reynolds number	41
2.4 Definition of Strouhal number for periodic flow motion	41

3	Description of case studies and setup of the CFD model	43
3.1	Description and production of the flow domain geometry	43
3.2	Governing equations and numerical solver	47
3.3	Description of case studies	48
3.3.1	Cases to study the effect of blockage ratios and Reynolds numbers	48
3.3.2	Cases to find the value of blockage ratio causing suppression of vortex shedding	48
3.4	Fluid data for the simulations	49
3.5	Assumptions involved in the simulation	49
3.6	Definition of metrics to assess the energy harvesting potential of the device	49
3.7	Selection of mesh size - mesh generation	50
3.7.1	Denser meshes generation for mesh independence study	54
3.7.2	Mesh independence study results	56
3.8	Time step selection - temporal discretization	58
3.9	Set up of Fluent model	61
3.10	Post processing of the simulations	66
3.10.1	Fundamental frequency and Strouhal number estimation	66
4	Parametric studies for various Reynolds numbers and Blockage Ratios	71
4.1	Effect of Reynolds numbers for various blockage ratios	73
4.2	Effect of blockage ratio for various Reynolds numbers	79
5	Investigation of vortex shedding suppression due to blockage ratio increase	83
6	Conclusions and future research	89
6.1	Conclusions	89
6.2	Future research	93
	Bibliography	95

List of Figures

Figure 1.1.	Sensor nodes scattered in a sensor field.[42], [2]	3
Figure 1.2.	Sensor networks protocol stack.[42], [2]	3
Figure 1.3.	Block diagram of a wireless sensor node [42]	5
Figure 1.4.	Forest fire detection with WSNs [20]	6
Figure 1.5.	General types of portable energy systems [42]	7
Figure 1.6.	General structure diagram of an energy harvesting system [52]	9
Figure 1.7.	Key components of a self-powered wireless sensor node [42]	10
Figure 1.8.	Block diagram of micro wind power system [52].	13
Figure 1.9.	Quartz	14
Figure 1.10.	Rochelle Salt	14
Figure 1.11.	SiO_2	14
Figure 1.12.	15
Figure 1.13.	15
Figure 1.14.	15
Figure 1.15.	Equivalent model for a piezoelectric vibration energy harvesting system [37]	16
Figure 1.16.	A standard energy harvesting circuit. [37]	16
Figure 1.17.	Piezoelectric coupling modes.[32]	17
Figure 1.18.	The structures and characteristics of piezoelectric transducers.[52]	18
Figure 1.19.	Vortex created by the passage of an aircraft wing, revealed by colored smoke	19
Figure 1.20.	Drawing of water vortex by Leonardo Da Vinci, ca. 1510-1513	19
Figure 1.21.	Geometry of oscillating membrane behind a flat plate [4].	20
Figure 1.22.	(a) Formation of von Karman vortex street without membrane and (b) the formation of a coherent wake behind the bluff body with a flexible membrane present[4].	20
Figure 1.23.	Eel system deployed [46].	20
Figure 1.24.	Eel movement behind bluff body [46].	20
Figure 1.25.	View of a flexible cantilevered in axial flow[43].	21
Figure 1.26.	Piezoelectric beam in the wake of a circular cylinder [1].	21
Figure 1.27.	(a) Schematic view of the final device (b) Photo of the actual device [53].	22
Figure 1.28.	Operation of a piezoelectric energy generator [26]	23
Figure 1.29.	An assembled energy generator. [26]	24
Figure 1.30.	Assembled energy generator. [26]	24
Figure 1.31.	Photo of the experimental set up [26]	25
Figure 1.32.	Computational domain for flow over two bluff bodies in tandem arrangement. [26]	25
Figure 1.33.	(a)Mesh near the two bodies. (b) Mesh near the single body.	25
Figure 1.34.	Focused view of the grid in the vicinity of the bluff bodies. [21]	26

Figure 1.35.	The computational flow domain used for the numerical simulations in [21]	27
Figure 1.36.	Locations of points p0, p1,..., p10 along the diaphragm, where the pressure evolution was computed for the case A2. Point p6 is the center S of the diaphragm.	28
Figure 2.1.	a left: Finite control volume approach - Eulerian representation, a right: Finite control volume approach - Lagrangian representation b left: Infinitesimal fluid element - Eulerian representation, b right: Infinitesimal fluid element - Lagrangian representation	32
Figure 2.2.	Turbulent velocity fluctuation in pipe flow as a function of time	36
Figure 2.3.	Unstructured grid around NACA 0012 airfoil in 2-dimensions	38
Figure 2.4.	a: structured quadrilateral grid, b: structured triangular grid, c: unstructured triangular grid [14]	39
Figure 2.5.	Typical choice of nodes in the FVM. The marked nodes are used in the flux balance of the control volume.[14]	40
Figure 2.6.	Variation of Strouhal number [19]	42
Figure 3.1.	Typical CFD modeling workflow	44
Figure 3.2.	Exploded view of the energy generator proposed in [26]	44
Figure 3.3.	The computational flow domain used for the numerical simulations.	45
Figure 3.4.	SpaceClaim GUI environment	45
Figure 3.5.	Creation of the computational domain 1/4	46
Figure 3.6.	Creation of the computational domain 2/4	46
Figure 3.7.	Creation of the computational domain 3/4	47
Figure 3.8.	Creation of the computational domain 4/4 - Final 2D domain	47
Figure 3.9.	Positions P1, P2,..., P21 along the diaphragm.	50
Figure 3.10.	Step list for CFD simulations with ANSYS fluent	51
Figure 3.11.	Mesh generation 1/3	51
Figure 3.12.	Mesh generation 2/3	52
Figure 3.13.	Mesh generation 3/3	52
Figure 3.14.	Denser mesh details on four front edges	53
Figure 3.15.	Denser mesh details on two base edges	53
Figure 3.16.	Final initial mesh	53
Figure 3.17.	Denser mesh around bluff bodies	53
Figure 3.18.	Final initial mesh details	54
Figure 3.19.	Grids corresponding to mesh size values of 1mm (top left) to 0.2mm (bottom left).	55
Figure 3.20.	Position of maximum pressure fluctuation amplitude along the diaphragm for various grid sizes.	56
Figure 3.21.	Average pressure drop in time predicted for the various grid sizes.	57
Figure 3.22.	Local pressure evolution in time for grids $G_{1,0}$ to $G_{0,3}$ at point P5	57
Figure 3.23.	Local pressure evolution in time for grids $G_{0,3}$ to $G_{0,2}$ at point P5	58
Figure 3.24.	Local pressure evolution in time at point P5 for BR=0.24 and case (a) C3, (b) C4, (c) C5, (d) C6, (e) C7. The blue curve concerns results obtained with $\Delta t = \Delta t_{bsl} = 10^{-5}s$, while the red one corresponds to results obtained with $\Delta t = \Delta t_c < \Delta t_{bsl} = 10^{-5}s$	59
Figure 3.25.	Local pressure evolution in time at point P5 for BR=0.27 and case (a) C5, (b) C6, (c) C7. The blue curve concerns results obtained with $\Delta t = \Delta t_{bsl} = 10^{-5}s$, while the red one corresponds to results obtained with $\Delta t = \Delta t_c < \Delta t_{bsl} = 10^{-5}s$	60

Figure 3.26.	ANSYS Fluent graphical user interface	61
Figure 3.27.	Set up of turbulence model and wall treatment	62
Figure 3.28.	Working fluid definition	62
Figure 3.29.	Velocity Inlet task page	63
Figure 3.30.	Pressure Outlet task page	63
Figure 3.31.	Computational domain walls definition	63
Figure 3.32.	Pressure evolution monitoring points	64
Figure 3.33.	Hybrid Initialization of flow field flow	65
Figure 3.34.	Pressure evolution in time for case C4	67
Figure 3.35.	FFT set up	68
Figure 3.36.	Spectral analysis (a) X-axis frequency (b) X-axis Strouhal	68
Figure 4.1.	Generated grids for various values of BR	71
Figure 4.2.	Iso-velocity contours predicted at 14ms in the baseline geometry (BR=0.27) for cases C1 to C7.	73
Figure 4.3.	Pressure fluctuation amplitude versus distance from the beginning of the diaphragm for BR=0.270	74
Figure 4.4.	Pressure fluctuation amplitude versus distance from the beginning of the diaphragm for BR=0.330	74
Figure 4.5.	Comparative pressure evolution at P5 for cases (a) C1-C2 (b) C3-C4 (c) C5-C6 (d) C7	75
Figure 4.6.	Variation of pressure amplitude with respect to inlet velocity	76
Figure 4.7.	Non-dimensional pressure amplitude coefficient with respect to Reynolds number.	76
Figure 4.8.	Variation of frequency with respect to inlet velocity	77
Figure 4.9.	Variation of non-dimensional frequency (Strouhal) with respect to Reynolds number	77
Figure 4.10.	Variation of average pressure drop with respect to inlet velocity	78
Figure 4.11.	Variation of non-dimensional average pressure drop with respect to Reynolds number	78
Figure 4.12.	Variation of pressure amplitude with BR for various Re numbers.	79
Figure 4.13.	Variation of pressure amplitude coefficient with BR for various Re numbers.	79
Figure 4.14.	Variation of frequency with BR for various Re numbers.	80
Figure 4.15.	Variation of Strouhal number with BR for various Re numbers.	80
Figure 4.16.	Variation of average pressure drop with BR for various Re numbers.	81
Figure 4.17.	Variation of average pressure drop coefficient with BR for various Re numbers.	81
Figure 4.18.	Surface plot of amplitude of the pressure signal at point P5, where maximum pressure amplitude occurs, as a function of BR and Re.	82
Figure 4.19.	Surface plot of frequency of the pressure signal at point P5, where maximum pressure amplitude occurs, as a function of BR and Re.	82
Figure 5.1.	Definition of S point (center of the diaphragm)	83
Figure 5.2.	Change in mean value and amplitude of pressure at the center of the diaphragm with BR increase from [26].	84
Figure 5.3.	Generated grids for vortex shedding suppression study	84
Figure 5.4.	(a) BR 0.240 - BR 0.300 S Point Pressure Evolution, (b)BR 0.330 - BR 0.390 S Point Pressure Evolution (c) BR 0.420 - BR 0.650 S Point Pressure Evolution, (d) BR 0.655 - BR 0.663 S Point Pressure Evolution	85

Figure 5.5.	Iso-velocity field on 25ms. (a) BR=0.420, (b) BR=0.550, (c) BR=0.662. $V_{in} = 20.7m/s$ const.	86
Figure 5.6.	Change in mean value and amplitude of pressure at the center of the diaphragm with BR increase by the present method.	86
Figure 5.7.	Focus on the range of BR values near that leading to vortex shedding suppression.	86
Figure 5.8.	Pressure amplitude on the center of the diaphragm and average channel pressure drop as functions of BR for constant inlet velocity.	87
Figure 5.9.	Frequency of the pressure signal at the center of the diaphragm as functions of BR for constant inlet velocity.	88
Figure 5.10.	Strouhal number of the pressure signal at the center of the diaphragm as functions of BR for constant inlet velocity.	88
Figure 6.1.	Average values of: Cp_{max} , Cp_{drop} , St with respect to Blockage Ratio	91
Figure 6.2.	Ratio of Δp_{max} to Δp_S with respect to Reynolds Number	91
Figure 6.3.	Ratio of Δp_{max} to Δp_{drop} with respect to Reynolds Number	92
Figure 6.4.	Average values of ratios: $\Delta p_{max} / \Delta p_S$ and $\Delta p_{max} / \Delta p_{drop}$, with respect to Blockage Ratio	92

List of Tables

Table 1.1.	Examples of prototyped applications for WSNs [22].	6
Table 1.2.	Comparison of power outputs from energy harvesting technologies.	9
Table 1.3.	Energy harvesting method corresponding to different vibration sources [52].	10
Table 1.4.	Nomenclature and description of cases simulated in [21].	27
Table 1.5.	Pressure amplitudes predicted at each case in [21]	28
Table 1.6.	Pressure amplitudes predicted for case A2 in[21]	28
Table 1.7.	Comparison of pressure variation amplitudes cases A2 and F2 at points upstream of S in [21]	29
Table 3.1.	Inlet velocity for the various Reynolds numbers and blockage ratios.	48
Table 3.2.	BR and Reynolds numbers with constant $V_{in} = 20.7m/s$	49
Table 3.3.	Mesh sizes	54
Table 3.4.	Fundamental Frequency and Strouhal number results of cases C1-C7 for constant BR=0.270	66
Table 5.1.	BR and Reynolds numbers with constant $V_{in} = 20.7m/s$	84

Chapter 1

Introduction

1.1 Motivation

In the last two decades, extensive research has been carried out, on power harvesting devices that exploit ambient surrounding energies to produce electricity. Micro-energy harvesting consists one of the most interesting perspectives of energy harvesting, having numerous applications; such a characteristic application is powering of Wireless Sensor Networks (WSN), where millimeter-scale energy harvesting devices are required. WSN comprises small dimension sensors that have been proposed and used in industrial process monitoring, control, machine health monitoring, structural health, bridge monitoring, predictive maintenance, environment monitoring, forest surveillance, intelligent buildings, etc. However, their main drawback is their limited duration of operation, thus, effective ways to recharge their batteries are sought. Furthermore, flow energy is readily available both outdoors and indoors in the form of air and water streams.

Various energy sources are offered for micro-energy harvesting: mechanical, flow, thermal, solar, electromagnetic, etc. In case of converting flow energy to electricity, the proposed miniature pneumatic power systems usually make use either of micro-turbines or bluff bodies. The former pose requirements for precise fabrication of millimeter-scale turbomachinery components, while the latter offer the advantages of simple design, easy fabrication and application. In case of using bluff bodies, one or more of them are appropriately installed into the flow in order to cause enhanced vortex shedding behind them for a wide range of Reynolds numbers. Vortex shedding induces pressure fluctuations that can be exploited by energy-converting materials to generate electrical power; such materials are for example piezoelectric membranes. Usually, flexible structures that can exploit fluid structure interaction phenomena, are used to utilize the piezoelectric effect and harvest flow energy. Various configurations using flexible membranes in conjunction with bluff bodies, both in external and internal flows, have been proposed and assessed in the literature, and will be analyzed on the next section. Often, fabricated prototype configurations are experimentally and/or numerically tested to assess their performance. Some of these studies aim to find the appropriate bluff body shape that produces significant vortex shedding; this is the same objective with that used in designing an effective flow meter. Furthermore, using multiple bluff bodies in tandem instead of one, consists an interesting perspective towards enhancing the associated vortex shedding.

In [26], a miniature pneumatic energy generating device was originally proposed and tested. This device utilizes one or two bluff bodies in tandem installed in a micro-channel. A flexible diaphragm, with a piezoelectric film on it, is located above the bodies at the upper wall of the channel. Pressure fluctuation and unsteady forces induced on the diaphragm due to vortex shedding

causing vibrations to it and converting mechanical energy to electrical. Such a device, that involves ease fabrication and installation, facilitates miniaturization and massive production avoiding the need for micro-assembling processes, could be used in liquid or gas pipeline systems. The main drawback of it is its low power output, so further research is required to enhance its performance. This device was numerically studied in [21] by means of setting-up an appropriate CFD model aiming to assess its prospective operation and performance. A CFD model was appropriately set-up and validated for further investigation. While in [26] the device was experimentally tested (measuring actual electric power output), in [21] extensive use of the CFD model was made in order to study the driving force for the operation of the device, i.e. the flow-field in the channel.

1.2 Wireless sensor networks

In the last two decades, Wireless Sensor Networks (WSNs) have grown rapidly and made big progress in many applications. Unfortunately, the main drawback of these systems is the limited life from the powering aspect. Batteries as the power source of wireless sensor nodes which are part of wireless sensor networks have restricted the development and wide application of these systems, having in mind that in most cases a very long lifespan for better performance is required. For that reason, the research for an alternative energy source is more than critical. Nowadays, it is obvious that the computer is a pivotal component of human beings and involves in our daily routine. As humans, we use the computer for gathering information from the web, for entertainment purposes, or for running a business and making science [42]. Pervasive computing, also called ubiquitous computing, is the growing trend of embedding computational capability (generally in the form of microprocessors) into everyday objects to make them effectively communicate and perform useful tasks, in a way that minimizes the end user's need to interact with the computer. Pervasive computing devices are network-connected and constantly available [42]. In order to achieve the construction of this network, a lot of computational devices are integrated into everyday objects and activities, to allow better interaction between the end user and computer. All these devices are commonly equipped with microprocessors, and communication abilities. Such devices are known as wireless sensor nodes. A wireless sensor network consists of several wireless sensor nodes. It is worth mentioning that when sensor nodes are arranged in a network form, will exhibit more and better characteristics than an individual sensor node[42]. The main objective of WSN is to provide and help the user to build an intelligent and more understandable environment known as a smart environment. Still today the WSN is an open research field and according to several researchers is one of the world's ten top technologies in the 21st century. For the sake of completeness and for better understanding in the next subsection, the main architecture of a wireless sensor network and wireless sensor node will be given briefly. It is also noted that the study of WSNs is not the main objective of this thesis.

1.2.1 Architecture of Wireless Sensor Network

A WSN typically consists of several pervasive sensor nodes distributed in the sensor field, sink, public networks (Internet or Satellite) manager nodes, and end-user as reflected in the below Figure.

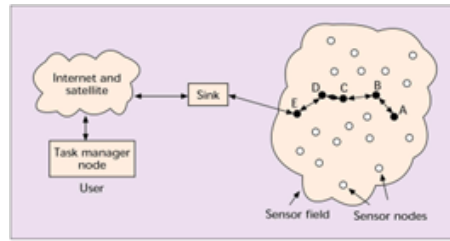


Figure 1.1. Sensor nodes scattered in a sensor field.[42], [2]

The main job of these nodes inside the sensor field is to collect data and route the useful information back to the end user. As we may observe from Figure 1.1 each node cooperates with each other via a wireless connection to set up a network in order to collect, disseminate and analyze data from the surrounding environment. For that reason, the data collected by node A is routed within the sensor field through other nodes. Node E is the boundary node and when the data reach this node is transferred to the sink for higher processing and communication with the task manager node. Namely, the sink serves as a gateway with higher processing capacity and communication abilities. The connection between the sink and task manager node and at the end with the user is established by using public networks such as the Internet or Satellite network. Finally, the end user will receive the information and valuable data and some post-processing of these data may be required. It is obvious that the sink is practically a coordinator between the sensor nodes and the end user. The communication of sensor nodes inside the sensor network is established via a wireless connection.

The basic concept and design of a WSNetwork are influenced by many factors, such as the location, sensor network topology, hardware constraint, transmission media, and most important for the current work the power consumption. Taking into consideration these parameters a design protocol or algorithm for the sensor network should be built up to manage all the processes described previously. In respect of that, a lot of research has been made to find a suitable protocol ideal for WSN applications. Wireless sensor networks follow the most common architecture OSI model. Basically, there are five layers in a sensor network. namely physical (lowest), data link, network, transport, and application (highest) layers, and three new elements: power management plane, mobility management plane, and task management plane [2].

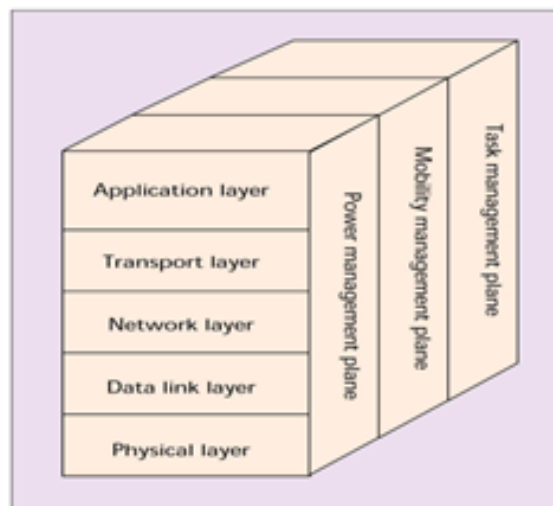


Figure 1.2. Sensor networks protocol stack.[42], [2]

A quick review of each layer and plane of the network protocol stack will be given here, starting

from the lowest level i.e physical layer to the highest level i.e application level.

1. **Physical layer** is to meet the needs of receiving and transferring collected data from the hardware. In order to achieve this process physical layer can provide an interface to transmit a stream of bits over physical medium, responsible for generating carrier frequency selection, signal detection, signal modulation, and data encryption.
2. **Data link layer** ensures reliable point-to-point and point-to-multipoint connections for the multiplexing data streams, data frames detection, medium access, and error control in the WSN.
3. **Network layer** takes care of routing the data supplied by the transport layer. There are various routing protocols available for this layer, they can be divided into flat routing such as direct diffusion, and hierarchal routing.
4. **Transport layer** the function of this layer is to provide congestion avoidance and reliability and there are a lot of protocols designed to provide this function are either applied on downstream and upstream. This layer is particularly needed when a system is organized to access other network. The basic function of this layer is to accept data from above layers and split it up into smaller units then pass these to the network layer and ensure the delivery of all pieces at the other end.
5. **Application layer**, is responsible for traffic management and provide software for different applications that translate the data in an understandable form or send queries to obtain information.

In addition to the above layers, there are three more cross planes involved in the stack protocol of the WSN which offers flexibility for WSN applications. These cross planes are the power management plane the mobility management plane and the task management plane. The three special planes in the stack help the sensor nodes to coordinate tasks and keep the power consumption low.

1. **Power management plane** is responsible for managing the power level of sensor nodes for processing, sensing, and communication.
2. **Mobility management plane** is responsible for detecting and recording the movement of sensor nodes to keep track of the route as well as the neighbors.
3. **Mobility management plane** is responsible for detecting and recording the movement of sensor nodes to keep track of the route as well as the neighbors.

In summary, the three management planes help the sensor nodes to work together in a power efficient way and share resources more wisely.

1.2.2 Architecture of Wireless Sensor Nodes in Wireless Sensor Network

A Wireless Sensor Network consists of many sensor nodes distributed throughout an area of interest i.e sensor field as reflected in Figure 1.1. Every wireless sensor node residing in the wireless sensor network is responsible to monitor quantities of interest of its local environment such as temperature vibrations humidity or other physical parameters. Upon the acquisition of these parameters, the nodes store the collected data in order to distribute them to the other sensor nodes via a wireless communication link. Figure 1.3 is the block diagram of each sensor node residing in the wireless sensor network. The nodes typically consist of four sub-units / blocks. These blocks are the sensor/transducer block, the data acquisition system, the microprocessor, and the radio communication block. The sensor, data acquisition, microprocessor, and radio communications are

all power sink modules because they need to consume electrical energy from the power source in order to operate. These sub-units of the sensor node are all energy hungry. Since the power source is driven by batteries, the energy-hungry sub-units would use up all the energy in the batteries after some time and the sensor node would then go into an idle state [20].

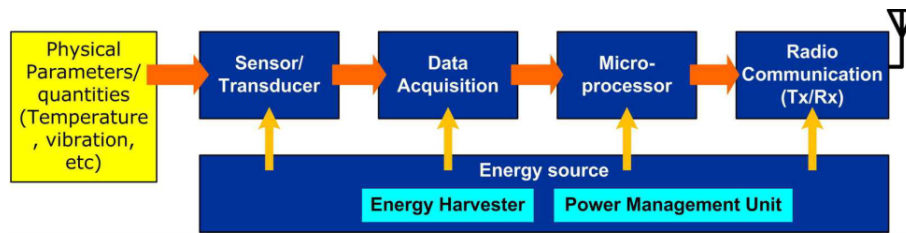


Figure 1.3. Block diagram of a wireless sensor node [42]

1. **Sensor/Transducer block:** Is responsible to convert an environmental sensing parameter to an electrical signal.
2. **Data Acquisition block:** Is incorporated in the sensor node to realize amplification and pre-processing of the output signals from sensors, for example, conversion from analog to digital form and filtering.
3. **Microprocessor block:** This makes the sensor node more intelligent and is responsible for data processing and time scheduling in the sensor node.
4. **Radio communication block:** Is responsible for the communication of the node with their neighbor nodes or the base station in a wireless manner.

The optimization of the sensor nodes in the respect of power consumption is a significant parameter for the better and more sustainable operation of the wireless sensor network. For the optimization process, there must be some considerations taken into account for example: how many sensor nodes are to be deployed in the network, should the nodes have to be active all the time, and how the communication between the nodes is achieved by consuming less power. It is obvious that all these requirements are case-specific and need to be addressed appropriately. According to the literature, there are plenty of applications involving sensor nodes where the nodes or part of them need to run only for a certain period, followed by a sleep cycle. This method is known as “duty cycling” which helps to extend the battery’s duration. It is also noted that according to [42] the energy consumption during sleep mode is in the μA while in operation mode the consumption is in the mA range. The problem with power consumption is becoming critical when the network becomes very dense with many sensor nodes.

1.2.3 Wireless Sensor Networks applications

With the development of microelectronics and wireless communication technology, WSNs are a hot research field all over the world. WSNs may be proved as a very valuable technology for critical fields such as **national defense and military applications, environment monitoring, healthcare, traffic control, industrial monitoring, target tracking, structural health monitoring, and so on**. In this section, some already existing applications will be presented emphasizing the importance of developing such networks for real applications. The major advantage of these networks is the ability to install them in places where wired connections are not possible, the terrain is inhospitable or the physical placement of the sensor is challenging. In addition to the above, the WSNs monitoring of the interest physical quantities can be achieved unattended without the

presence of humans. Some examples found in the literature of prototyped applications for WSNs are presented in Table 1.1

Application	Type	Requirements	Data amount and frequency	Scale and density
Great Duck Island [23]	Environmental monitoring	Data archiving, Internet access, long lifetime	Minimal, every 5–10 min, 2–4 h per day	32 nodes in 1 km ²
PODS in Hawaii [11]	Environmental monitoring	Digital images, energy-efficiency	Large data amounts, infrequently	30–50 nodes in 5 hectares
CORIE (Columbia River) [9]	Environmental monitoring	Base stations, lifetime	Moderate data amounts, infrequently	18 nodes in Columbia River
Peek value evaluation [13]	Environmental monitoring	Collaborative processing, minimal network traffic	Moderate data amounts, periodically	Case dependent
Flood detection [12]	Environmental monitoring	Current condition evaluation	50 bytes every 30 s	200 nodes 50 m apart
SSIM (artificial retina) [33]	Health	Image identification, realtime, complex processing	Large data amounts, frequently every 200 ms	100 sensors per retina
Human monitoring [15]	Health	Quality of data, security, alerts	Moderate data amounts, depend on the human stress level	Several nodes per human
WINS for military [24]	Military	Target identification, realtime, security, quality of data	Large data amounts, infrequently	Several distant nodes
Object tracking [29]	Military	Collaborative processing, realtime, location-awareness	Large data amounts with high frequency near an object	7 (prototype) nodes in proximity
Vehicle tracking [34]	Military	Identification and coordination, realtime	Large data amounts every 8 s near an object	1024 nodes in 40 km ²
WINS condition monitoring [24]	Machinery monitoring	Data aggregation, machinery lifetime projection	Depend on machinery complexity and its current status	Few nodes per machinery
Smart classrooms [51]	Education	Context-sensing, data exchange	Large data amounts in random frequency	Several nodes in classroom

Table 1.1. Examples of prototyped applications for WSNs [22].

In addition to the above examples of WSN, this technology may have a dominant role in a very critical problem especially here in Greece which is forest fires. Sensor nodes are randomly and densely deployed in a forest. Sensor nodes can broadcast the exact origin of the fire to the users before it spread uncontrollably. Most sensor nodes are equipped with optical systems. Also, they are equipped with power rummage methods such as solar cells for their power supply. The nodes will associate with each other to perform distributed sensing and overcome many obstacles [20].



Figure 1.4. Forest fire detection with WSNs [20]

1.2.4 Problems in powering the Wireless Sensor Network

One of the most important issues in our daily life is the reduction of the power consumption in the systems we use. The problem of energy consumption is one of the major issues in wireless sensor networks as well. The sensor nodes as described previously are hungry-energy devices and they are equipped with batteries as an energy source. These networks can be deployed in hazardous and inhospitable places where the recharging or replacing of batteries becomes a very difficult task. The energy consumption of the nodes depends upon major operations of the sensor nodes which are sensing of data processing, communication, and data transmission. The communication and transmission part of their operation needs a significant amount of energy. According to the literature, a non-rechargeable lithium battery can provide up to 800 WH/L (watt-hours per liter) or equivalent 2800 J/cm³. One possible solution to overcome the problem of batteries' poor energy density is the use of a wired power cable. Nevertheless, adopting this solution many of the advantages of WSNs such as self-autonomous and mobility of the sensors are sacrificed. So the use of power cables is not a preferable option for powering these systems knowing the advantages of the wireless option. In most applications, the lifetime of a sensor node should range from two to ten years depending on the requirements of the specific application. There is no doubt that batteries, rechargeable or not, are not able to meet this requirement without human presence for replacing or recharging. In Figure 1.5 are listed many types of portable energy systems that can be utilized as a powering system for WSNs. Our focus will be given to the energy harvesters and more specifically to the piezoelectric energy harvesters such as the device under consideration in the present work.

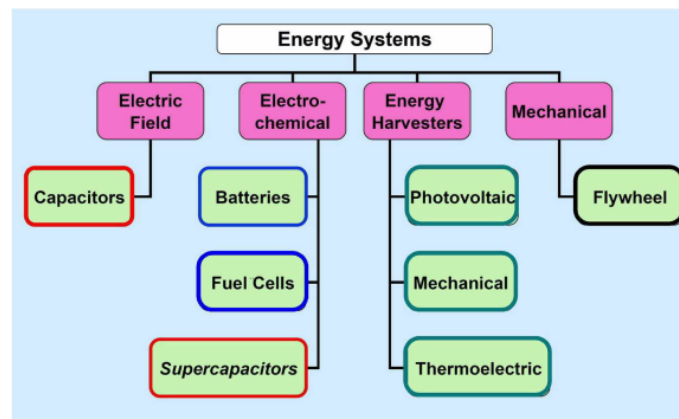


Figure 1.5. General types of portable energy systems [42]

It is clear that the performance of the wireless sensor nodes that are part of a wireless sensor network is inextricably linked with limitations coming with electrochemical energy systems. As discussed previously the energy storage capabilities of batteries and other systems such as supercapacitors impose constraints on the sustainable operation of the networks. It is also noted that the lifetime of the network is determined by the characteristics of the batteries used. To overcome this problem alternative solutions for the powering of the networks have been proposed in the literature. Some of these solutions are presented below.

The first proposed solution in the literature to overcome the aforementioned problem is the improvement of the performance of the finite power sources by increasing the energy density of the power sources [42][2]. The second “straightforward” solution is the reduction of the power consumption at different levels of the sensor nodes i.e signal processing algorithm, operating systems, the optimization of the various protocols, and communications activities. The last solution is the development of energy harvesting systems techniques that enable the system to generate the power that is needed by harvesting energy from the environment. The main issue of this thesis is

the primary study of an energy harvesting device from the surrounding environment. Thus special attention will be given to this solution [42].

Regarding the first proposed solution, a lot of research for the increase the storage density of batteries and electrochemical power systems has been conducted for many years. It is obvious that increasing of the storage density leads to extending the lifetime and duration of the nodes but of course, it is impossible to extend their lifetime indefinitely. The second solution i.e reducing the power consumption of sensor nodes, seems to be a sustainable solution utilizing the technique of duty cycle operation with which the sensor nodes are sleeping most of the time. Furthermore, the optimization of the algorithms and operating systems may lead to lower energy consumption. Besides the above, the solution of sustainable power sources for WSN utilizing the surrounding environment will give a permanent solution to the powering problem of the devices. The main idea behind this solution is that a node would convert renewable energy abundantly available in the environment into electrical energy using various conversion schemes and materials for use by the sensor nodes. This method is known as energy harvesting because the node is harvesting the energy from the environment. If this method is adopted for the powering of the networks, then the failure of any component of the system will be the only limit to its smooth operation. Nevertheless, the implementation of this method is quite tricky, having in mind that renewable energy sources are made up of different forms of ambient energy and thus there is no one solution for all applications. In the next section, a quick review of energy harvesting systems will be presented.

1.3 Overview of energy harvesting systems - Sources of microenergy harvesting

Energy harvesting is a technique that captures or harvests unused ambient energy from the environment and converts the captured energy into usable energy, in our case electrical energy, which is stored and used for powering the WSNs eliminating the limitations imposed by the batteries and other finite energy sources. The main disadvantage of this technique is that the harvesting energy is very small for miniaturized systems in comparison to large-scale applications. Furthermore, when we are dealing with large-scale applications the power stations are fixed at a given location in contrast with the small scale which is mainly portable. As mentioned earlier, the sustainable operation of the sensor nodes depends on the battery energy which is often limited. The development of energy harvesting techniques is a key factor for the extended operation of wireless system networks. We are lucky if we consider that our environment has plenty of unused ambient energy such as solar, wind, vibration, ocean waves, etc. These sources are already available in the environment without having to pay as in the case of fossil fuels used by internal combustion engines to create electrical energy i.e diesel generators. Finally, the WSNs need to be self-powered without the need for component replacement for for a long operation time.

There is a variety of methods to harvest energy in the ambient environment. In the literature, the classification of the methods is organized based on the different forms of energy. The most common methods and sources for harvesting energy are listed below. A swift review on mechanical and dynamic fluid energy harvesters will be presented on this section, while the piezoelectric energy harvesters will be presented in the next section as it is the dominant energy harvesting method, due to the device under investigation in the present work. The rest energy harvesting methods are presented on the below list for reference and completeness reasons only.

- Photovoltaics Power Generation
- Mechanical Energy Harvesters

1. Piezoelectric Energy Harvesters.

2. Electrostatic (Capacitive) Energy Harvesting.
 3. Electromagnetic Energy Harvesting.
- Thermoelectric Generators
 - Dynamic Fluid Energy Harvesting
 1. Micro Wind Harvester.
 2. Flowing Water Energy Harvesting.
 - The Acoustic Energy
 - Magnetic Energy Harvesting
 - Hybrid Power Source

The Table 1.2 depicts and compare the power output of different energy harvesting methods, while in Figure 1.6 the general structure of energy harvesting system is shown. It is worth mentioning, that the ambient harvested energy can be provided directly in the nodes or stored into energy devices according to the magnitude of output power. Furthermore, the key components of a self-powered wireless sensor node is depicted in Figure 1.7.

Harvesting Method	Power Density	References
Solar energy—outdoors	15mW/cm ³ - bright sunny day 0.15mW/cm ³ - cloudy day	[31]
Solar energy - indoors	10-100μW/cm ²	[49]
Vibrations (Piezoelectric - show inserts)	330mW/cm ³	[35]
Vibrations (Electrostatic conversion)	0.021μW/mm ³ - 105 Hz	[36]
Vibrations (electromagnetic conversion)	184μW/cm ³ - 10 Hz 306μW/cm ³ - 52Hz	[54]
Wind flow	16.2μW/cm ³ - 5m/s	[47]
Acoustic noise	3nW/cm ³ - 75 dB 960 nW/cm ³ - 100 dB	[31]
Magnetic field energy	130μW/cm ³ - 200μT, 60 Hz	[45]

Table 1.2. Comparison of power outputs from energy harvesting technologies.

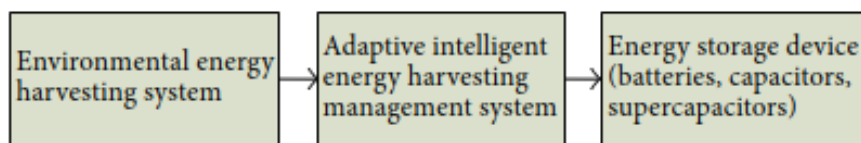


Figure 1.6. General structure diagram of an energy harvesting system [52]

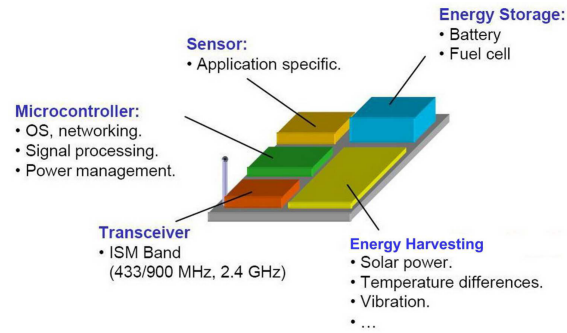


Figure 1.7. Key components of a self-powered wireless sensor node [42]

1.3.1 Mechanical Energy Harvesting

As is already known, mechanical energy is generated when an object is forced into some kind of movement or mechanical deformation. A very well-known example is the internal combustion engine where chemical energy is converted to mechanical energy through pistons' reciprocating motion. In that case, the pistons are forced into movement and finally, mechanical energy is produced. In the device under consideration in the current work, mechanical energy is generated when the piezoelectric membrane is subjected to periodic mechanical deformation, exploiting Karman vortex street generation behind the bluff bodies. The mechanical energy produced by the vibration can be converted into electrical energy by several methods such as piezoelectric, electrostatic, and electromagnetic conversion, in order to power the energy-hungry sensor nodes with the necessary amount of energy ensuring their sustainable and continuous operation. In our world vibration is the most prevalent energy source for it is available in many environments and structures such as buildings, bridges, vehicles, ships, and in many other kinds of everyday facilities. Apart from civil structures and machine monitoring, the vibration existence can also be utilized in the biomedical sciences for the monitoring of the crucial parameters of the human body, like blood pressure or blood sugar levels, etc. According to the force excitation and basic excitation (displacement and velocity), vibration sources act on the vibration energy harvesting system which converts the mechanical energy into electrical energy as shown in the below table [52].

Form of vibration sources	Energy harvesting method
Displacement excitation	Piezoelectric electrostatic energy harvesting method
Velocity excitation	Electromagnetic energy harvesting method
Force excitation	Piezoelectric energy harvesting method

Table 1.3. Energy harvesting method corresponding to different vibration sources [52].

As mentioned above, the methods that mechanical energy can be converted to electrical energy are mainly three. For the electrostatic and electromagnetic energy conversion, the basic working principles will be discussed in this section. The last method i.e piezoelectric energy harvesting will be discussed in more detail in the next section where the basic concept of the piezoelectric phenomenon is also presented.

An electrostatic (capacitive) energy harvesting system, generates voltage by changing the capacitance of the capacitor. It is broadly known that the capacitor is defined as a device that

consists of two conductors separated by a distance that can hold opposite charges. According to the bibliography on the matter, change in capacitance caused by change in distance or relative position between two conductors by external vibration, is the basic principle of capacitive energy harvesting, and the generated electrical power is provided to the sensors. In comparison with the other vibration energy harvesting methods, the current method has very good compatibility with integrated circuits (IC) and microelectromechanical systems (MEMS) technology. The power output of this technology is discussed in [36], where an electrostatic vibration energy harvester with a mass of 4.9mg delivers an average output of power of 0.0924 μ W when harvesting 10 μ m of motion at 105Hz, it is also noted that the size of the harvester in the subject work is 3000 μ m \times 3000 μ m \times 500 μ m. A lot of research has been already done both in the academic and the industry on the matter, and the reader may find in the literature some interesting papers [38], [36], [5].

Electromagnetic energy harvesting. Electromagnetic energy harvesting is a technology that relies on the principle of electromagnetic induction. This principle states that an electromotive force is generated in a conductor when the magnetic flux surrounding it changes. Electromagnetic energy harvesters can be packaged in a way that minimizes the risk of corrosion and eliminates temperature constraints. There is a significant amount of electromagnetic energy around us, mainly transmitted by communication devices. Some harvesting devices are able to capture this energy and convert it into electricity, which can then be stored in capacitors and batteries or used as a power source directly. There are several key factors to consider when designing and evaluating electromagnetic energy harvesters. One of the most important is the principle of magnetic induction, which refers to the process by which an electromotive force is generated in a conductor when the magnetic flux surrounding it changes. Other factors to consider include the frequency of the electromagnetic field, the amplitude of the field, the distance between the energy harvesting device and the source of the field, the load resistance of the device being powered, the overall efficiency of the energy harvesting process, and the cost of the energy harvesting device and its materials. All of these factors can impact the efficiency and feasibility of a particular energy harvesting technology.

Rahimi et al. published a study in which they described an electromagnetic (EM) energy harvester system that was able to power a 1.5 V, 15 μ A load with a conversion efficiency of 65%. This system had a ripple of 5% and was able to generate a maximum output power of 22.5 μ W when subjected to external vibrations at a frequency of 10 Hz [28].

Tao et al. proposed a micro electromagnetic vibration energy harvester that was only 4.5 x 4.5 x 1 mm in size, with a total volume of around 20 mm^3 . Testing showed that this device was able to generate a peak-peak voltage of 20.9 μ V at its resonance frequency of 365 Hz and an input acceleration of 1g. While this study demonstrated the potential for integrating electromagnetic harvesters with microelectromechanical systems (MEMS) technology, the generated energy is still quite limited [44]. It's important to note that among the three techniques for capturing mechanical energy, piezoelectric and electrostatic harvesters are capable of producing voltage levels between 2 and 10 V. However, electromagnetic harvesters have a maximum voltage output of only 0.1 V. Vibration energy harvesting systems are subject to random external excitations, so it is important that they have a good response to vibrations with a range of frequencies and amplitudes in order to maximize energy harvesting efficiency. When designing the system damping ratio, it is necessary to take into account both the output power of the system and the bandwidth of the resonant region. To maximize the generated energy, the following basic principles should be followed in the design of vibration energy harvesting systems such as the device under consideration.

- To achieve resonance, the frequency of the vibration energy harvesting system should match the frequency of the external excitation.
- To increase the efficiency of vibration energy harvesters with fixed structures, it is important to try to increase the relative motion transmissibility when the level of external excitation

remains constant.

- To optimize the performance of vibration energy harvesters with a fixed mass of inertial components, it is advisable to try to reduce the damping ratio of the system, provided that a certain bandwidth of the resonance region is maintained.

1.3.2 Dynamic Fluid Energy Harvesting

Dynamic fluid energy harvesting refers to the process of extracting energy from the motion or flow of a fluid, such as water or air. This type of energy harvesting is typically used to power small electronic devices or to charge batteries in situations where access to other sources of power is limited or unavailable. There are several different approaches to dynamic fluid energy harvesting, including the use of hydrokinetic turbines and anemometers. Hydrokinetic turbines use the kinetic energy of flowing water to generate electricity, while anemometers use the motion of wind to generate electricity. Dynamic fluid energy harvesting has the potential to be a renewable and sustainable source of energy, but current technology is often limited by low conversion efficiency and high cost. Further research is needed to improve the performance and cost-effectiveness of these systems in order to make them more practical for widespread use. According to the literature, fluid kinetic energy can be harvested through two methods. The first involves the use of mechanical components, such as micro turbine systems, to generate electricity. The second method employs nonmechanical elements that function similarly to mechanical energy harvesting technology, where the movement of flowing wind or water causes mechanical vibrations that can be converted into electricity through piezoelectric, electrostatic, or electromagnetic principles. The last two conversion methods are described above and the first i.e piezoelectric method will be described in the next section in greater detail. The potential output mechanical power of a fluid energy harvester, such as the device being studied in this project, can be calculated using the following equation.

$$P_m = \frac{1}{2} C_p \rho A v^3$$

where:

- C_p is the performance coefficient of the harvester which is equal to the efficiency of flowing energy converted to mechanical energy.
- ρ is the the flow density.
- A is the cross sectional area.
- v is the fluid velocity.

There are two main fluids that can be exploited for energy harvesting through fluid motion in nature: water and air. The device being examined in this project belongs to the first category, as it generates electricity through wind harvesting. A concise description of micro wind harvesters and flow water energy harvesters will be presented below for the powering of WSNs.

Micro Wind Harvesters: Wireless autonomous sensor nodes in outdoor, remote, or difficult-to-access locations can also use ambient air flow or forced convection as an energy source [25]. There are several methods for harvesting wind energy, including micro wind turbines, micro wind-belt generators, piezoelectric wind harvesters, and electromagnetic wind generators. While conventional wind turbines are the most commonly used method for wind energy harvesting, their efficiency decreases with size due to increased friction losses in bearings and reduced blade surface area. Additionally, the rotating components of conventional turbines are prone to fatigue and wear. Micro windbelt generators have higher output power at high wind speeds (>5.5 m/s), but their output power decreases significantly at low wind speeds (<3.5 m/s) and they can be very

noisy during operation [53]. Piezoelectric wind harvesters have several advantages, including a compact structure, sensitivity to low-speed wind, high efficiency, instant starting with no dead time, small size and lightweight, extremely low magnetic permeability, and almost no heat dissipation [41]. However, the poor piezoelectric strain coefficient of some materials can result in low output power, and piezoelectric materials only generate maximum power when vibrating at their resonant frequency. In Figure 1.8 the composition block diagram of micro wind power system is depicted. As we may observe, due to the intermittence and instability of the wind, an energy storage device is necessary in order to have a stable and continuous powering of the wireless sensor nodes.

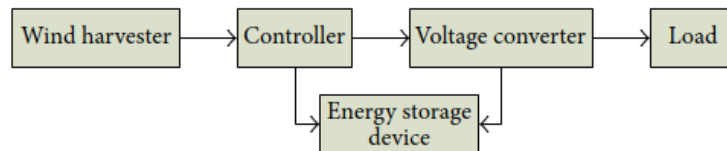


Figure 1.8. Block diagram of micro wind power system [52].

Wind energy has numerous benefits, including being limitless, renewable, and free to use. It is also environmentally friendly and widely available in many parts of the world. However, there are also some challenges to using wind energy. It has low energy density, which can lead to uneven electricity production. Additionally, wind speeds can vary significantly and are difficult to predict, leading to instability in the energy supply. Wind turbines may also produce noise due to their moving mechanical parts. The examined device of this project uses the wind energy in order to produce electricity for the powering of WSNs [].

Flowing water energy harvesting:Hydropower can be generated from the kinetic energy of flowing water, which is created by pressure fluctuations. This energy can be captured using energy harvesters and converted into electricity [50]. Flowing water is a clean, renewable, and reliable energy source for wireless sensor nodes. Additionally, hydropower can be developed in various sizes and scales, making it a suitable option for use in wireless sensor networks [40]. Hydropower systems can be used to power wireless sensor networks (WSNs) that are used to monitor the water quality and hydraulic state of water distribution systems, rivers, and other bodies of water. When selecting an energy harvester for these applications, it is important to consider the size and energy requirements of the system. While hydroturbines are capable of generating sufficient power for wireless sensors, they may be too large for easy installation in pipelines or integration with sensor nodes. On the other hand, flow-induced vibration energy harvesters are much smaller, but more research is needed to increase their conversion efficiency and optimize their output for use in powering WSNs.

1.4 Piezoelectric Phenomenon and Piezoelectric Energy Harvesters (PEH)

1.4.1 Piezoelectric Phenomenon

The piezoelectric phenomenon (or effect) is the ability of specific materials to produce/generate an electrical charge by applying mechanical stresses to them. The definition of the word piezoelectric is derived from Greek ‘πιεζω’ which means press or squeeze. The most important characteristic of this phenomenon is its reversibility, meaning that materials exhibit the direct piezoelectric effect (generation of electricity when mechanical stress is applied), also the converse piezoelectric effect (generation of mechanical stress when an electrical field is applied). Back in 1800 the brothers Pierre and Jacques Curie discovered the direct piezoelectric phenomenon. By utilizing their knowledge of pyroelectricity and crystal structures and behavior, the two brothers demonstrate the first piezoelectric effect by using crystals of Rochelle salt, quartz, topaz, tourmaline etc. On the first attempts, they supported that Rochelle salt and quartz exhibited the most piezoelectricity efficiency at the time.

Back in 1800 the brothers Pierre and Jacques Curie discovered the direct piezoelectric phenomenon. By utilizing their knowledge of pyroelectricity and crystal structures and behavior, the two brothers demonstrate the first piezoelectric effect by using crystals of Rochelle salt, quartz, topaz, tourmaline etc. On the first attempts, they supported that Rochelle salt and quartz exhibited the most piezoelectricity efficiency at the time.



Figure 1.9. Quartz

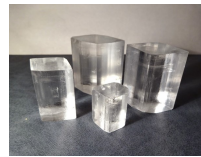


Figure 1.10. Rochelle Salt

The first practical application of the piezoelectric effect came with WWI where used in the development of sonar devices. This initial use of piezoelectricity in sonar created intense international developmental interest in piezoelectric devices. Over the next few decades, new piezoelectric materials and applications were explored and developed by scientists. In this study, the direct piezoelectric phenomenon will be utilized, to convert the flow energy into electricity, without this being the main purpose of the work. For clarity reason, a description of the direct effect will be presented below.

Firstly, an attempt will be made to explain the phenomenon by utilizing the quartz (silicon dioxide or SiO_2) piezoelectric material. The quartz element consists of silicon and oxygen atoms as reflected in Figure 1.11



Figure 1.11. SiO_2

The big question here is why the piezoelectric materials produce an electric field when mechanical stresses are applied to them. To get the answer to this question first we need to understand a concept called electronegativity. Electronegativity refers to the ability of an atom to attract shared electrons in a covalent bond. The higher the value of the electronegativity, the more strongly that element attracts the shared electrons. In our case, the oxygen and silicon atoms share one electron, and due to the smaller size of oxygen atoms, the shared electron is closer to the oxygen nucleus. In this respect, oxygen exerts more force on the electron than silicon as reflected in Figure 1.12.

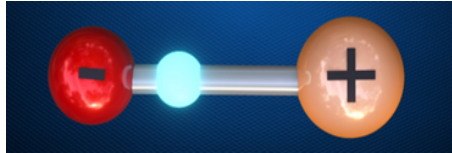


Figure 1.12

As a result, oxygen is more electronegative than silicon and will have a slightly negative charge and of course, the silicon atom will have a slight positive charge. As a result, the oxygen and the silicon atom together constitute a dipole. In the quartz crystal, these dipoles are arranged such that the center of charges of the negative and positive atoms coincide.

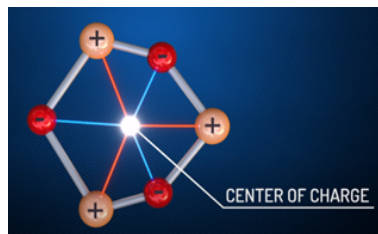


Figure 1.13

If we apply a compressive force across the molecules as shown in Figure the center of charges will not coincide anymore and will be a charge separation, and this phenomenon is called polarization. This means that an electric field will be created between the net positive and negative charges and this leads to the generation of a small voltage across it.

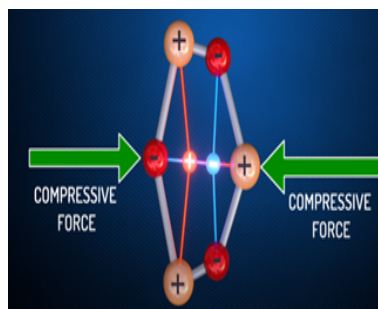


Figure 1.14

1.4.2 Piezoelectric Energy Harvesters

One of the appealing aspects of piezoelectric materials is their flexibility, which makes them well-suited for power harvesting. These materials have the ability to convert large amounts of mechanical energy into electrical energy and can withstand significant strain. It is worth mentioning that, in

recent years, the use of piezoelectric materials, along with advances in piezoelectric properties and the integration of low-power electronic devices, has attracted significant attention as a technology for piezoelectric harvesting. Furthermore, piezoelectric transduction is typically more effective in systems with reciprocating rather than rotating motions. There are several types of piezoelectric materials, including piezoelectric monocrystals, ceramics, polymers, and composites. Piezoelectric monocrystals are single crystals that exhibit piezoelectricity, which is the ability to generate a voltage in response to applied mechanical stress. Examples of piezoelectric monocrystals include quartz, tourmaline, and topaz. Piezoelectric ceramics are non-conductive, inorganic materials that exhibit piezoelectricity. Examples of piezoelectric ceramics include lead zirconate titanate (PZT) and barium titanate. Piezoelectric polymers are organic materials that exhibit piezoelectricity. Examples of piezoelectric polymers include polyvinylidene fluoride (PVDF) and polyurethane. Piezoelectric composites are materials that are made up of multiple components, one of which is a piezoelectric material. These composites can be designed to exhibit enhanced piezoelectric properties, making them attractive for use in various applications.

Currently, piezoelectric ceramics made from lead zirconate titanate (PZT) are the most commonly used piezoelectric materials. PZT ceramics have several advantages, including a well-established manufacturing process, low cost, high electromechanical coupling constants, and high energy conversion rates. On the other hand, PZT ceramics are fragile and are not able to withstand large amounts of strain. They are also prone to fatigue cracking and brittle fractures when subjected to high-frequency cyclic loads. It is also noted the PVDF has lower electromechanical coupling constants compared to PZT, but has several advantages, including good flexibility, high mechanical strength, good fatigue resistance, and chemical stability. Hence make it suitable for use in applications that involve high-frequency periodic loads.

A key factor in the design and optimization of a power generation device is the efficiency of converting mechanical energy into electrical energy. According to Shu [37], current piezoelectric-harvesting research falls mainly into two key areas: developing optimal energy harvesting structures; and secondly, developing highly efficient electrical circuits to store the generated charges. In her research, she modeled the piezoelectric generator as a mass+spring+damper+piezostructure and connect the arrangement to a storage circuit system see Figure 1.15.

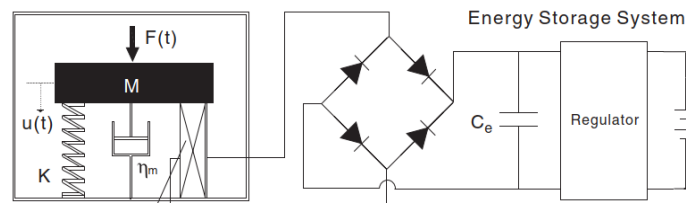


Figure 1.15. Equivalent model for a piezoelectric vibration energy harvesting system [37]

After conducting a mathematical analysis, an expression was derived to represent the average power produced from piezoelectricity-based vibration. This expression, which pertains to a standard electronic interface as depicted in Figure 1.16, helps to understand the key parameters that influence power generation using a piezoelectric device.

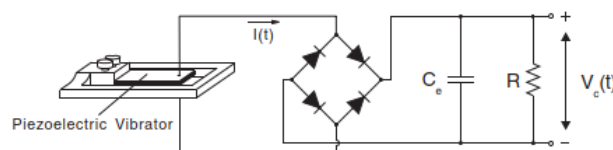


Figure 1.16. A standard energy harvesting circuit. [37]

$$\bar{P} = \frac{P}{\frac{F_0^2}{\omega_{sc} M}} = \frac{1}{\left(r\Omega + \frac{\pi}{2}\right)^2} \frac{k_e^2 \Omega^2 r}{\left\{ \left(2\zeta_m + \frac{2k_e^2 r}{\left(r\Omega + \frac{\pi}{2}\right)^2}\right)^2 \Omega^2 + \left(1 - \Omega^2 + \frac{k_e^2 r \Omega}{\left(r\Omega + \frac{\pi}{2}\right)^2}\right)^2 \right\}}$$

where:

- F_0 is the constant magnitude
- ω_{sc} is the natural oscillation frequency
- ζ_m is the mechanical damping ratio
- \varOmega is the the normalized frequency
- r is the normalized electric resistance
- k_e^2 is the alternative electrochemical coupling coefficient
- M is the oscillation proof mass

According to the abovementioned expression, the estimated generated power is influenced by various factors, including the frequency and acceleration of the input vibration, the electrical load, the oscillating proof mass, the natural frequency of the system, the mechanical damping ratio, and the electromechanical coupling coefficient. Thus for the better performance of the piezoelectric device these parameters should be studied very carefully during the design phase both of the device structure and electrical circuits.

Another important design parameter that must be taken into consideration is the piezoelectric coupling modes. For the applied phenomenon, there are mainly two piezoelectric coupling modes, as depicted in Figure 1.17. In the first mode, i.e., d33, the vibration force is applied in the same direction as the poling direction and perpendicular to the piezoelectric area. On the other hand, in the d31 mode, the force is applied perpendicular to the poling direction and parallel to the piezoelectric area. According to the literature, the d33 mode has a higher coupling coefficient compared to d31, but the latter is able to produce a larger strain with a small external force, which is preferable when designing energy harvesters for wireless sensor networks. Therefore, between the two modes, the mode d31 is most commonly used [32].

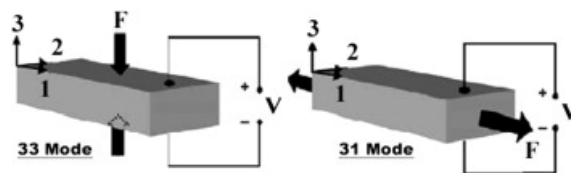


Figure 1.17. Piezoelectric coupling modes.[32]

After selecting the appropriate piezoelectric coupling mode, choosing the correct piezoelectric transducer is crucial for maximizing the harvesting of mechanical energy in energy harvesting devices. The transducer must be selected based on the environmental vibrations it will encounter and the structure of the device. There are several types of piezoelectric transducers available, as shown in the following Figure, which also includes a column detailing the characteristics of each type.







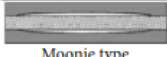
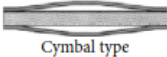
Piezoelectric transducers	Characteristics
 Unimorph	A highest power can be generated under lower excitation frequencies and load resistances, widely used in cantilever beam structure
 Bimorph	Variable range of resonant frequency: 5 Hz–100 Hz, can be used in various configuration such as cantilever beam and end-end clamped beam
 Rigid bimorph	Similar to bimorph but easier mounting, suitable for wide bandwidth, and widely used in cantilever beam structure
 Macrofiber composite (MFC)	Flexible, both d31 and d33 modes practicable, suitable for low strain and high frequency application, large area coverage, and can be used as a bimorph component
 Stack type	Suitable for the application of low frequency (~10 Hz) and large uniaxial stress, easy mounting
 Rainbow type	Ability to generate a higher output voltage in the given stress level, can be stacked to amplify output voltage
 Moonie type	Ability to withstand high stress, high output charge level, and adjustable resonance frequency
 Cymbal type	

Figure 1.18. The structures and characteristics of piezoelectric transducers.[52]

There are several benefits to using piezoelectric energy harvesting devices, including a straightforward design, low cost, lack of heat generation, absence of electromagnetic interference, ease of production, and relatively high output voltage level. Additionally, these devices have a high electromechanical conversion efficiency. Additionally, the piezoelectric harvesting system is able to produce a high level of output energy when it resonates with external vibration. However, it typically requires an energy harvesting circuit to regulate the output power, which can result in a significant energy loss due to the switch control circuit. This can significantly impact the efficiency of the energy harvesting system. It is obvious that, in order to improve the performance, efficiency, and practicality of piezoelectric energy harvesters, ongoing research focuses on enhancing the properties of existing piezoelectric materials, identifying new materials with high piezoelectric constant strain, electromechanical coupling coefficient, and low loss, and optimizing the structure of piezoelectric energy harvesters to increase output power. In addition to the above, the most important and crucial field of research, is on developing piezoelectric energy harvesters in order to meet the unknown or time-changing external excitation and wide band vibrations [52].

1.5 Karman vortex street and vortex-induced vibrations (VIV)

The vortex shedding phenomenon was described and painted firstly by Leonardo Da Vinci in ca. 1510 by drawing some very accurate sketches of the vortices in the flow behind bluff bodies. The term vortex shedding is meaning an oscillating flow that developed when a fluid (liquid or air) flows

past a bluff body at specific velocities. In the wake field past these bodies' vortices are created and detached periodically from both sides creating the Von Karman vortex street. The formation of vortices in the body wakes was described by the Hungarian-American mathematician, aerospace engineer, and physicist Theodore von Karman. In fluid dynamics, vortices are one of the most important and major components of turbulent flows. The distribution of velocity, vorticity (the curl of the flow velocity), as well as the concept of circulation are used to characterize vortices. In most vortices, the fluid flow velocity is greatest next to its axis and decreases in inverse proportion to the distance from the axis.



Figure 1.19. Vortex created by the passage of an aircraft wing, revealed by colored smoke



Figure 1.20. Drawing of water vortex by Leonardo Da Vinci, ca. 1510-1513

Vortex-induced vibrations (VIV) are oscillations that can occur in structures when they are subjected to a fluid flow, such as wind or water. These vibrations are caused by the interaction between the structure and the vortices that are shed from the structure as the fluid flows past it. In the case of a Karman vortex street, the alternating vortices that are formed behind a bluff or cylindrical object can induce vibrations in the object itself or in other nearby structures. These vibrations can be a problem if they become large enough, as they can lead to fatigue and potentially cause damage to the structure. VIV is a phenomenon that is of concern in the design of offshore structures, such as oil platforms and bridges, as well as in the design of ships and other marine vessels. Engineers use various methods to mitigate the effects of VIV, such as adding damping devices or modifying the shape of the structure to reduce the shedding of vortices. However, Vortex-induced vibrations (VIV) can potentially be used for micro energy harvesting, which is the process of collecting small amounts of energy from sources such as ambient vibrations or fluctuations in temperature. One way that VIV could be used for micro energy harvesting is by attaching piezoelectric materials to a structure that is subjected to fluid flow. These materials generate an electric charge when subjected to mechanical stress, such as the vibrations caused by the interaction between the structure and the vortices in a Karman vortex street. The generated electric charge can then be collected and used to power small electronic devices or to charge batteries. Researchers have been investigating the use of VIV for micro energy harvesting in recent years, and there have been some promising results. However, the efficiency of VIV-based micro energy harvesting systems is still relatively low compared to other methods, and further research is needed to improve the performance of these systems.

1.6 Energy harvesting techniques using bluff bodies - Literature review

Nowadays in order to address the need for micro-scale energy harvesting from fluid kinetic energy different devices and working principles are proposed in literature. In this subsection, a detailed literature review containing the main principles and outcomes of these devices will be developed. Nevertheless, this dissertation will be focused on micro-scale energy harvesting devices using bluff bodies proposed in the literature.

Back in 2001 Allen and Smits [4] examines the feasibility of placing a piezoelectric membrane or eel in the wake of a bluff body and using the von Karman vortex street forming behind the bluff body to induce oscillations in the membrane. They examined the response of the membrane to vortex shedding. The power output of this device is not presented.

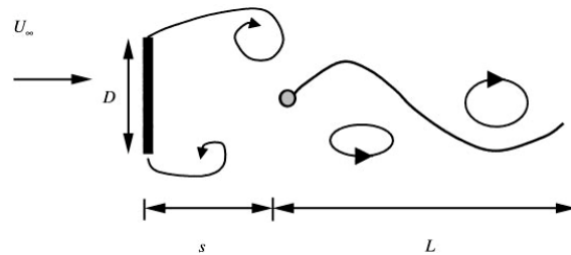


Figure 1.21. Geometry of oscillating membrane behind a flat plate [4].

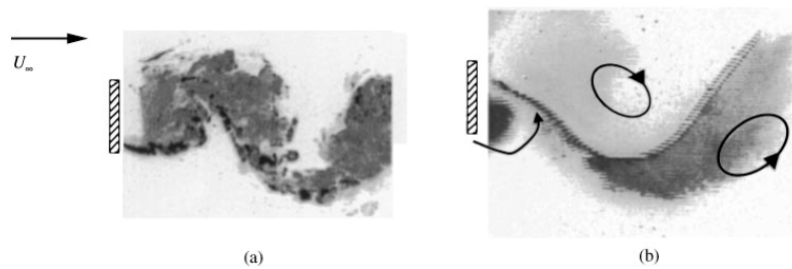


Figure 1.22. (a) Formation of von Karman vortex street without membrane and (b) the formation of a coherent wake behind the bluff body with a flexible membrane present[4].

Taylor et al. [46] developed an eel structure of piezoelectric polymer to convert mechanical flow energy to electrical power. They have focused on characterization and optimization of the individual subsystems of the eel system with a generation and storage units in a wave tank.

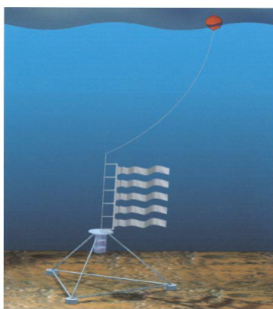


Figure 1.23. Eel system deployed [46].

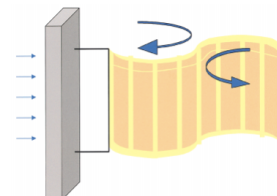


Figure 1.24. Eel movement behind bluff body [46].

To successfully transition the Eel from the flow tank to an estuary and then to the ocean, there will be several tasks that must be solved, such as the automatic orientation of the eel and bluff body to the direction of the flow, the construction of the device with resistance to the marine corrosive environment, waterproofing the flexible Eel body, eliminating cabling between the electronics housing and the Eel body.

In another study Tang et al. [43] designed a flutter-mill to generate electricity by extracting energy from fluid flow. Their structure is similar to the eel systems of Allen and Smits [4] and Taylor et al. [46]. The energy transfer between the structure and the fluid flow was investigated through an analytical approach by using a fluid-elastic model.

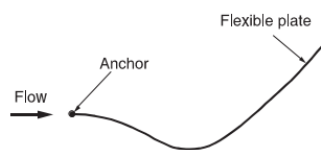


Figure 1.25. View of a flexible cantilevered in axial flow[43].

The eel structures of Allen and Smits [4], Taylor et al. [46], and Tang et al. [43] have the potential to generate power from milli-watts to many watts depending on system size and flow velocity.

Akaydin et al. [1] investigated energy harvesting from unsteady air flows using a piezoelectric cantilever beam in the wake of a circular cylinder. The beam is oriented parallel to the incoming flow and fixed at its downstream end. The distance of the beam from the vortices and their circulation affect the output power significantly. The reported values are as follows: The maximum output power was approximately $4\mu\text{W}$ with corresponding Reynolds number of 14800.

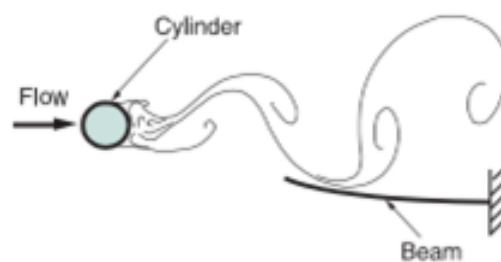


Figure 1.26. Piezoelectric beam in the wake of a circular cylinder [1].

Zhu et al.[53] attached an aerofoil to a cantilever which is placed behind a bluff body in a wind tunnel. Their electromagnetic generator can operate at a wind speed of 2.5 m/s with a corresponding electrical output power of $470\mu\text{W}$ and an initial displacement of the aerofoil is required for its operation.

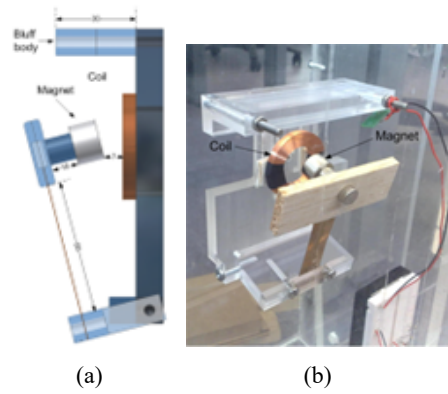


Figure 1.27. (a) Schematic view of the final device (b) Photo of the actual device [53].

Peng et. al [27] were carried out experimental studies to investigate the performance of new type vortex shedder used in Karman vortex flowmeter. They reports that dual bluff body in tandem arrangement can enhance the hydrodynamic vibration generated by the vortex shedding. Another advantage of the dual bluff body over single bluff body is the regularity of the vortices as stated in [27]. Furthermore Venugopal et. al [48] carried numerical and experimental studies with different blockage ratios in a vortex flowmeter and concluded that a blockage ratio of 0.28 is best among all the blockages of triangular bluff bodies as it gives high amplitude signals. It is noted that the blockage ratio in a pneumatic energy harvesting device is defined as the ratio between the front face bluff bodies heights divided by the flow channel height. As stated earlier the main focus of this work will be given to microscale energy harvesting devices using bluff bodies, and thus a more deep analysis will be carried out on this literature review.

In the literature, CFD simulations are focused on the investigation and optimization of vortex flowmeters. Not many simulations are carried out in order to further investigate the idea of energy harvesting through fluid motion. Although the operation principle is similar in both of the cases there are differences. In a vortex flow meter, the most important parameter is to maintain a steady Strouhal number over different fluid velocities. That affects the accuracy of the flowmeter. Venugopal et al. [48] examined three different turbulent models $k-\epsilon$ Realizable, $k-\epsilon$ RNG, and $k-\epsilon$ Standard and they reported that the $k-\epsilon$ RNG model is the most adequate in predicting vortex shedding.

Another miniature energy generator using air for harvesting energy that exploits the Karman vortex effect is proposed from Nguyen et al. [26] where the flexible diaphragm in this case is connected to a piezoelectric film. In the air flow channel two triangular bluff bodies are installed in tandem arrangement. Two triangular bluff bodies enhance pressure fluctuation and the amplitude in the vortex street. In this study, two-dimensional flow analysis were conducted using ANSYS FLUENT software. According to the authors, two-dimensional analyses may be adequate for testing the feasibility of the design although there are phenomena that cannot be captured. The average power produced from the device is 0.49 nW and approximately a voltage of 14 mVp with a pressure fluctuation of 70 Pa and inlet velocity of 20.7 m/s. Authors also argue that the blockage ratio of 0.26 was not adequate and they propose a blockage ratio of 0.33. Also, they propose to move the center of the flexible diaphragm to a wall position just above the aft bluff body and adopt a piezoelectric material with higher piezoelectric constants [26]. The device performance was not examined under different velocities, therefore Reynolds numbers, to determine the efficiency under different conditions.

As mentioned earlier, in this thesis further investigation will take place on the device proposed by Nguyen et al. [26] For that reason a more detailed reference should be made, in order to get a better understanding of the main principles of the device's operation. According to the authors, the

miniature pneumatic energy generator utilizes the pressure variation induced by the formation of the Karman vortex street behind bluff bodies in an airflow channel. Due to the variation of the air pressure in the channel a polydimethylsiloxane diaphragm (PDMS) and a cantilever piezoelectric are driven into vibration, then the vibration (mechanical) energy is converted to electrical utilizing the piezoelectric phenomenon through the piezoelectric film [16].

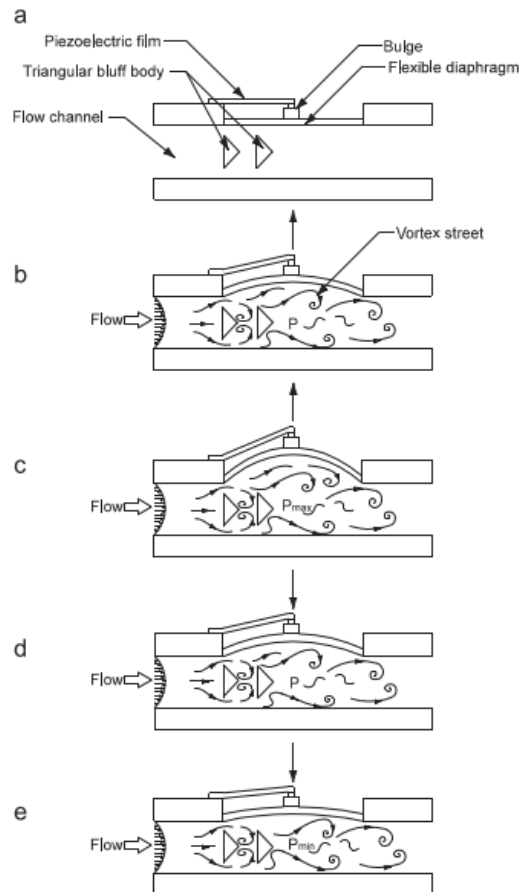


Figure 1.28. Operation of a piezoelectric energy generator [26]

A schematic of the piezoelectric energy generator is shown in Figure 1.28(a) to (e). As reflected in Figure 1.28(a) the device has a flexible diaphragm installed on the wall of a flow channel. Two bluff bodies (triangular shape) in tandem arrangement are placed in the flow channel. A piezoelectric film of a cantilever type is glued to a bulge affixed to the top surface of the flexible diaphragm. The piezoelectric film can oscillate with the flexible diaphragm due to the vortices shed from the bluff bodies in an air flow. As shown in Figure 1.28(b) air flow is supplied to the channel. Pressure in the flow channel behind the bluff bodies may fluctuate with the same frequency as the pressure variation caused by the Kármán vortex street. Then the pressure in the channel causes the diaphragm and the piezoelectric film to deflect in the upward direction. As the pressure increases to the maximum, the diaphragm reaches its highest position (Figure 1.28 (c)). When the pressure drops, the diaphragm and the piezoelectric film deflect downward (Figure 1.28 (d)). As the pressure decreases to the minimum, the diaphragm reaches its lowest position (Figure 1.28 (e)). By ensuring the repeatability of this process the energy harvesting from the air flow in the channel is possible. The authors decided to use triangular bluff bodies in the proposed device due to its performance in terms of pressure amplitude. As mentioned earlier Venugopal et al. reported that triangular and trapezoidal (bodies with sharp edges) bluff bodies give higher wall pressure am-

plitudes instead of conical, ring type, and circular ones. In this study [26], in order to access the feasibility of the proposed energy generator, the authors have decided to set up a numerical model to estimate the pressure fluctuation behind bluff bodies. In these simulations, the performances of single and dual bluff bodies in tandem were studied and compared. in terms of the pressure amplitude. After the simulations, a prototype of this device was constructed with dual bluff bodies, and an experimental setup was used to measure the pressure in the flow channel, the deflection, and the voltage output of the device. Finally, the experimental results were compared with the results of the simulations.

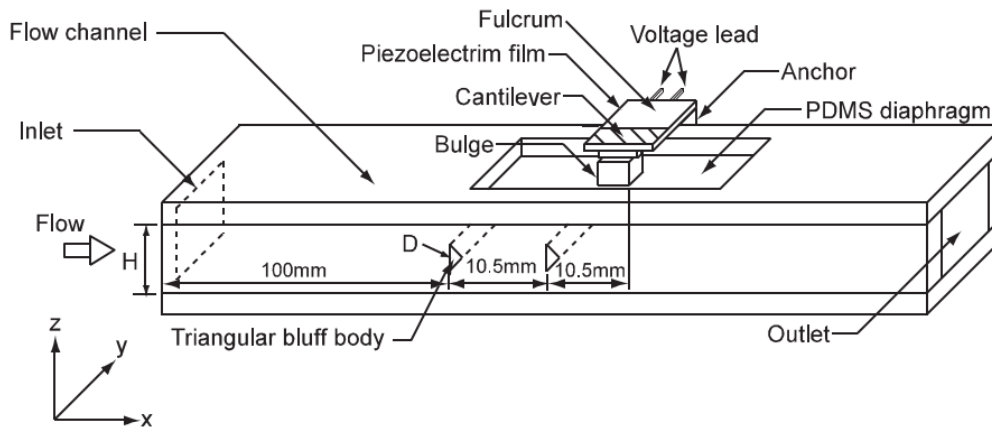


Figure 1.29. An assembled energy generator. [26]

In Figure 1.29 a 3D drawing of the proposed energy generator device is presented. The main particulars of this arrangement are the flow channel, two triangular bluff bodies, a PDMS diaphragm bonded to the channel, and a piezoelectric film attached to the PDMS diaphragm through a bulge.

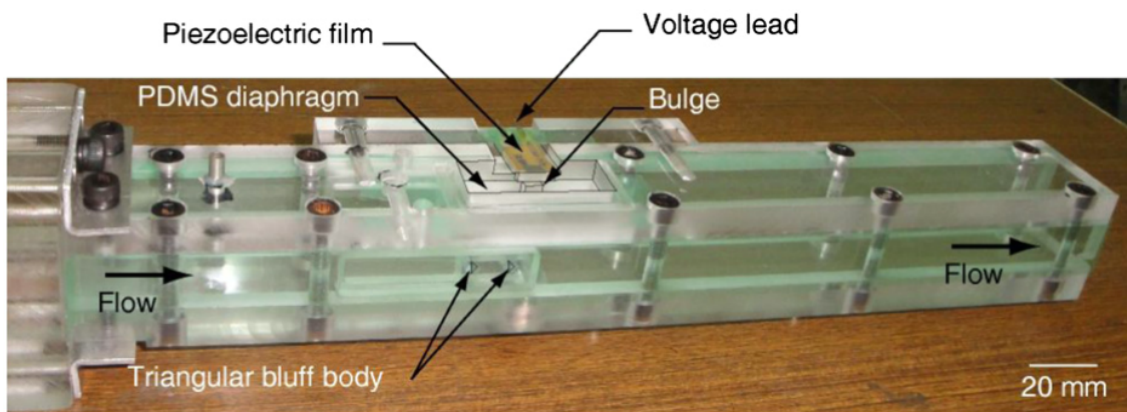


Figure 1.30. Assembled energy generator. [26]

In Figure 1.30 the final device used in the experiments is presented. The length of the device is 300mm and the inner height is 16mm. More details about the experimental setup and computational fluid domain used in the CFD analysis will be given in Chapter 3. Finally, Figure 1.31 is a photo of the final experimental arrangement depicting the fabricated device for testing. The energy generator Figure 1.30 is a part of the assembled set up and it is fixed on a table. An inlet pipe connects to the outlet of a wind tunnel and forced air flows to the inlet of the energy generator. The outlet of the flow channel is kept open to the atmosphere.

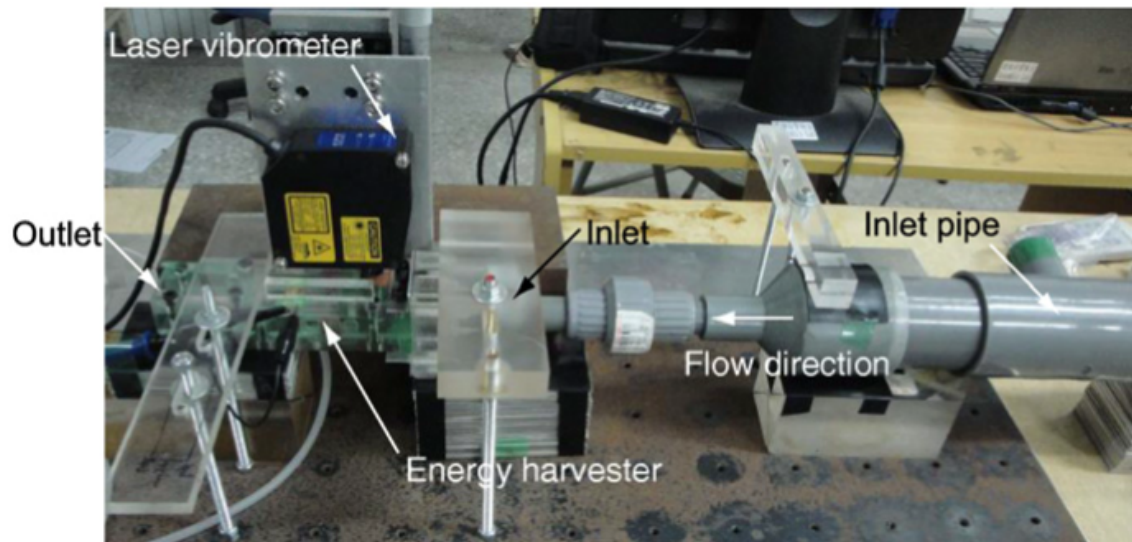


Figure 1.31. Photo of the experimental set up [26]

As stated previously, in addition to experiments the authors carried out numerical simulations to obtain the pressure fluctuation of the flow behind the bluff bodies. In this respect, two-dimensional flow analyses are carried out using the commercial software ANSYS FLUENT. The dimensions of the computational domain are reflected in Figure 1.32. For these simulations, the authors assumed that a fixed wall bounds the flow. Additionally, the fluid-structure interaction phenomena are ignored. The scope of the CFD analysis is to evaluate the pressure amplitude applied to the flexible diaphragm and test the design's feasibility. In this diploma thesis, this study will be considered as a baseline case by taking into consideration the analysis of Koubogiannis [21] as well.



Figure 1.32. Computational domain for flow over two bluff bodies in tandem arrangement. [26]

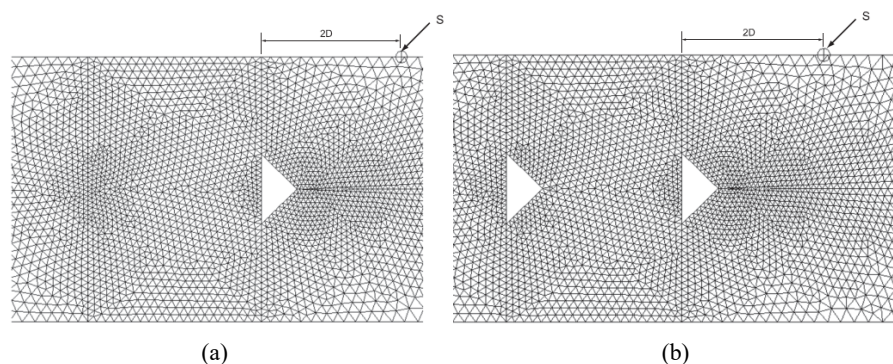


Figure 1.33. (a) Mesh near the two bodies. (b) Mesh near the single body.

From the Figure 1.32 the principals dimensions of the computational domain can be extracted as a function of bluff body width $D=4.25\text{mm}$ (see Figure 1.29). A closer view of the unstructured

mesh created for the simulations is reflected in Figure 1.33 (a) and (b). The static pressure at the center of the flexible diaphragm, indicated by the symbol S as shown in Figure 1.33 is monitored in the simulations. The point S is located 2D downstream of the aft bluff body. It is noted that the detailed set up of the computational domain and the parameters defined for the simulations is a part of the Chapter 3.

On 2016 Koubogiannis [21] carried out an extensive and detailed CFD study on the device proposed by Nguyen et. al [26]. For the same device the author examined different bluff body shapes. The used shapes are itemized as follows:

1. The original triangular bluff body used on the study of Nguyen et. al
2. The original triangular bluff body turned by 180o so the sharp edge faces the incoming flow.
3. A semicircle with its circular arc shaped side facing the incoming flow.
4. An orthogonal triangle turned 35o with respect to the vertical direction and pointing to the diaphragm
5. A rectangular body.
6. A original triangular bluff body with blockage ratio (BR) of 0.33.

The unstructured computational mesh for each case is reflected on the following figure.

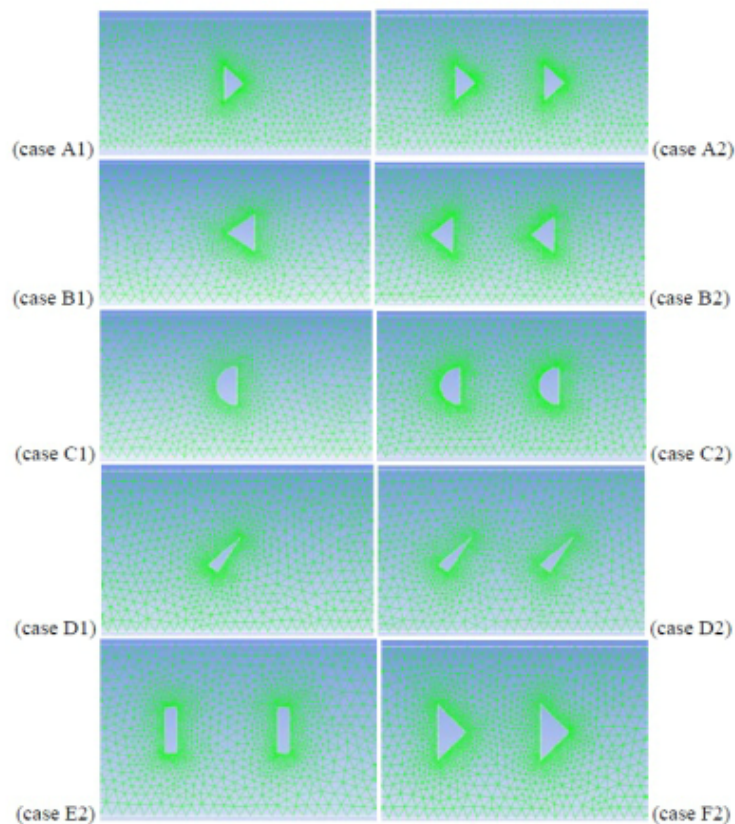


Figure 1.34. Focused view of the grid in the vicinity of the bluff bodies. [21]

In each case, two configurations were tested, namely those containing either one or two bodies of the corresponding shape, respectively. Whenever one bluff body was used, this was located at section BB1. In case of two bluff bodies, the second one was located in front of the first at section BB2 (Figure 1.35).

Incoming flow on	triangle-base	triangle 180 deg	semi-circle	orthogonal triangle 35 deg	rectangle	triangle base BR = 0.33
Number of bodies	1	A1	B1	C1	D1	-
	2	A2	B2	C2	D2	E2

Table 1.4. Nomenclature and description of cases simulated in [21].

Table 1.4 presents the nomenclature that was used for the set of the (ten) different test cases simulated in the context of the author study. The corresponding geometries are shown in Figure 1.34, where focused views of the computational grids in the vicinity of the bluff bodies are presented as stated previously. The computational domain used in the case A2 is reflected in Figure 1.35. The symbol S corresponds to the center of the flexible diaphragm where the unsteady pressure evolution in time was computed. For each case the pressure fluctuation amplitude is defined as $\Delta p = p_{max} - p_{min}$. This quantity was considered to be an indicative quantity for the vortex shedding severity. Air was used as the working fluid in the channel. An inlet velocity of value $V_{in} = 20.7m/s$ was considered by author in order to compare the results with [26]. For all simulations a constant velocity was implemented resulting a constant Reynolds number. More details about the other parameters and set up of the CFD model and also for the mesh generation will be given at Chapter 3.

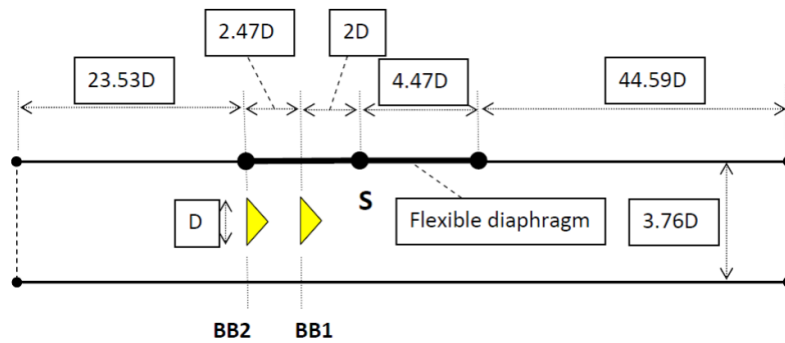


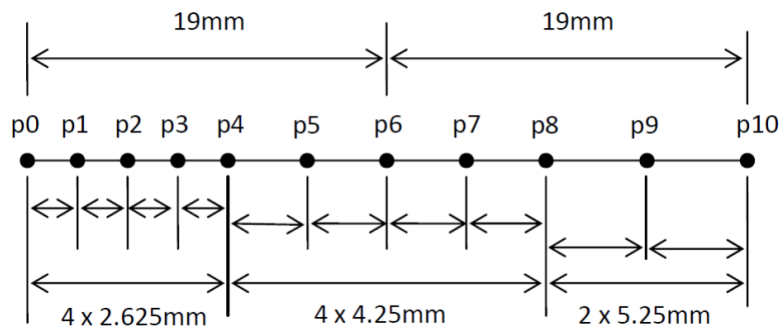
Figure 1.35. The computational flow domain used for the numerical simulations in [21]

Table 1.5 summarizes the pressure amplitudes Δp predicted for each of the cases that were simulated. With reference to this table, configuration A (i.e A1 and A2) seems to produce the larger pressure amplitudes in comparison with the others configuration (i.e B,C,D,E). For cases C1, C2 the results are practically the same, while in cases B2 and D2 the use of a second body suppresses the variation amplitude instead of enhancing it. From this analysis, the author concluded that the triangular body shape located as in cases A1 and A2 causes the more severe pressure variations, and the existence of the second body enhances the phenomenon.

Case	A1	A2	B1	B2	C1	C2	D1	D2	E2	F2
Δp [Pa]	165	240	75	35	35	35	28	23	100	335

Table 1.5. Pressure amplitudes predicted at each case in [21]

As a second part of the same work, using the same configuration (i.e A2 configuration) and in order to access the proper location of the device, 11 points along the upper wall, at positions other than S, were considered along the original diaphragm. The location of these points denoted by p_0, p_1, \dots, p_{10} are presented in Figure 1.36. The results of this analysis are summarized in Table 1.6 and according to them, points p_3 and p_5 exhibit a significant increase of the pressure variation amplitude that is of the order of 46% compared to the reference one which calculated $\Delta p = 240 Pa$ at the center of the diaphragm. It is also noted, that point p_6 corresponds to denote S from the previous analysis.

Figure 1.36. Locations of points p_0, p_1, \dots, p_{10} along the diaphragm, where the pressure evolution was computed for the case A2. Point p_6 is the center S of the diaphragm.

From this analysis, the main conclusion is that the maximum variation amplitude occurs upstream the current position of the diaphragm center S and not downstream as shown in the below table. It is important to be mentioned that the outcomes of these computations are in accordance with similar findings and results in [26], where the same device was examined.

Point	p_0	p_1	p_2	p_3	p_4	p_5	p_6
Δp [Pa]	235	250	245	355	280	350	240

Table 1.6. Pressure amplitudes predicted for case A2 in [21]

Another important parameter according to the literature [48] is the blockage ratio which plays a very important role in the pressure variation amplitude and thus in the performance of the device. As stated in literature in the region near the point where maximum pressure variation occurs and pressure is minimum. In order to achieve even smaller pressure values and, consequently, greater pressure variation amplitudes, greater nearby velocity should be attained. [48]. One way to achieve that is by decreasing the flow area or another way is to increase the width D of the bluff body, leading to an increase of BR. In study [48] after experimental evaluation, they stated that a BR of 0.30 was found to be the optimum, while in [26] a BR of 0.33 was numerically predicted as the optimum value. The usage of a BR greater than the optimum one could lead to suppression of the phenomenon due to the proximity of walls at smaller distances to the bluff body.

Case F2 of the current study [21] was set up in order to check the literature's statements regarding the blockage ratio. Case A2 was simulated again in a channel with BR=0.33 (instead of the original BR which was 0.27) by increasing the triangle base length D. The qualitatively conclusions of this analysis are the same as previous i.e upstream of the center S the amplitudes are greater than the downstream region. The increase of pressure fluctuation by increasing the BR (to an optimum value) seems to be important. Table ... summarizes the pressure amplitudes values for the same points upstream of S (or point p6) for both cases A2 and F2. According to the author the case with a greater blockage ratio i.e case F2, occurs a mean increase of approximately 50% over the amplitudes of the smaller blockage ratio.

Point	p0	p1	p2	p3	p4	p5	p6
Δp [Pa], A2 case	235	250	245	355	280	350	240
Δp [Pa], F2 case	325	390	385	500	470	525	335
% increase	38%	56%	57%	41%	68%	50%	40%

Table 1.7. Comparison of pressure variation amplitudes cases A2 and F2 at points upstream of S in [21]

The main conclusions of the study conducted by Koubogiannis [21] are that the shape of the bluff bodies is very important to achieve significant pressure variations, as well as that the design of the whole configuration including parameters such as the number of bodies, the position and the relative position and the arrangement, the blockage ratio of the channel and the position of the flexible diaphragm, is very crucial in order to harvest significant amounts of energy. The current study in addition to the study conducted by Nguyen et al [26] will be considered as the base-line cases for this thesis diploma as stated previously.

1.7 Thesis outline

In this section, after the first introductory chapter is finished, an outline of the remaining content will be provided.

- In the Chapter 1 of this thesis, the motivation for the research is presented and an overview of wireless sensor networks is also provided. In sections 1.1 and 1.2, the main operational principles of these networks and the challenges and problems related to their powering are discussed. In the following section, an overview of the main techniques for energy harvesting that utilize the ambient environment is provided, with a focus on mechanical energy harvesting and transducer techniques and energy harvesting from fluid motion such as air and water. Special attention is given to the piezoelectric phenomenon and piezoelectric energy harvesters, which are relevant to the nature and working principle of the device under consideration. The Karman vortex street, which is created in the wake of bluff bodies and is the key factor in the pressure fluctuation that produces mechanical vibration in the membrane, is also mentioned. In the last section of Chapter 1, a literature review of similar proposed devices that utilize the piezoelectric phenomenon and vortex shedding phenomenon is presented, with special attention given to the device under consideration and previous research on this particular device.
- In Chapter 2, the theoretical framework, the governing equations, and the mathematical models that are involved in the investigation are presented. The definition of the non-dimensional numbers of the problem take place in Chapter 2 as well.
- In Chapter 3, the focus is given on the computational fluid dynamics model (CFD) setup and case studies description. The appropriate metrics for evaluating the device performance are described, as well as the computational mesh generation and time step selection process, the creation of the computational domain, the selection of the turbulence model, and the wall treatment. A mesh independence study is also conducted to ensure that an appropriate mesh, which would not affect the computational results, is selected.
- In Chapter 4, the results of the different Reynolds numbers in the inlet boundary of the duct and the effect of using different blockage ratios by changing the baseline geometry of the problem is presented. On Chapter 3, Section 3.3.1 a detail description of the subject case study is reported. Finally, the related results and figures that were obtained from the post-processing steps are presented.
- In Chapter 5 The performance of the device in terms of vortex shedding maximization until its suppression is also discussed and a comparison with similar studies is made.
- Finally, in Chapter 6 a recap of the main results and interest points of the above studies are discussed. Moreover, some thoughts and ideas for future research on the matter are also presented.

The bibliography and sources that have been used in the current work are presented on the last pages of this paper.

Chapter 2

Theoretical framework: Governing Equations and Computational Fluid Dynamics

The flows in nature can be described and analyzed in several ways. The main fundamental ways to describe and study the flow fields in the past years are based on experimental, theoretical analysis, and numerical simulations. Numerical simulations are often used as a very powerful tool to support research studies in science and for engineering applications as well. In the last two decades, with the wide development of the power of computers, numerical simulations have become very attractive from the aspects of speed, safety, and cost in many cases, and their use is widely accepted in the academic fields and in the industry as well. Numerical simulation is a valuable tool to analyze in a reduced time complex phenomena that may be difficult to study with theoretical or experimental approaches. In fluid dynamics, the analysis of various fluid fields with numerical simulation means the development and implementation of algorithms and numerical schemes in order to solve the fundamental equations of fluid mechanics. This field of study is well known as Computational Fluid Dynamics or CFD. The fluid flows are governed by the following three fundamental principles:

- Mass is conserved.
- Momentum is conserved. ($F = ma$ Newton's second law)
- Energy is conserved.

The aforementioned fundamental principles are expressed in terms of mathematical equations, which are usually partial differential equations. Unfortunately, these equations can not be solved in the context of numerical simulations by keeping their differential form. Thus computational fluid dynamics is a way of replacing the fundamental partial differential equations of fluid flow with numbers, and using the appropriate discretization of these numbers in space (spatial discretization) and time (temporal discretization) a final numerical description of the interest flow field occurs. This definition of the CFD of course is not an all-inclusive definition given that there are several problems that the immediate solution of the flow field without the aforementioned discretization is allowed. Furthermore, some problems involve the integral expression of the governing equations instead of differential ones. The result of any approach after the implementation of CFD analysis is in all cases a collection of numbers and not a closed-form analytical solution. [14]

In fluid dynamics, there are two fundamental models – methods that a flow field can be described. These two methods are worldwide known as the Eulerian and Lagrangian descriptions. A general flow field represented by streamlines as shown in Figure 2.1 is considered. From this flow,

a closed volume within a finite region of the flow is considered. This volume defines a control volume, V , and a control surface, S is defined as the closed surface which bound the volume. By using the first description i.e Eulerian method, this control volume is fixed in space with the fluid moving through it Figure 2.1 a left. In the second description alternatively i.e Lagrangian method the control volume is moving with the fluid as shown in Figure 2.1 a right. It is very difficult to obtain the fluid flow equations if we are looking at the whole flow field, for that reason our attention is limited only on the fluid of the pre-described finite volume region. When applying the beforementioned fundamental principles the directly derived equations following the control volume method are in integral form. From integral form by implementing the appropriate mathematical handling, we may derive indirectly the equations in partial differential form.

It is possible to derive the governing equations directly in differential form by imagining an infinitesimally small fluid element in the flow rather than control volume Figure 2.1 b. Again, instead of looking at the whole flow field at once, the fundamental physical principles are applied to just the fluid element itself.

By using the Eulerian approach (fixed volume or element flow in space) to derive the governing equations (in integral or differential form), we obtain the conservation form of the governing equations. If now we are using the Lagrangian approach, (finite volume or element flow moving with fluid) to derive the governing equations (in integral or differential form) we obtain the non-conservation form of the governing equations. The terms conservation and non-conservation form of the governing equations makes little difference in most theoretical applications. When we talk about numerical procedures such as CFD, which form is used can make a difference in some applications. The deeper analysis and derivation of the governing equations are beyond the scope of the present work. For reasons of completeness, the governing equations are presented in this chapter by following the Eulerian method (preferred in numerical simulations) in the infinitesimal fluid element. See Figure 2.1 b left.

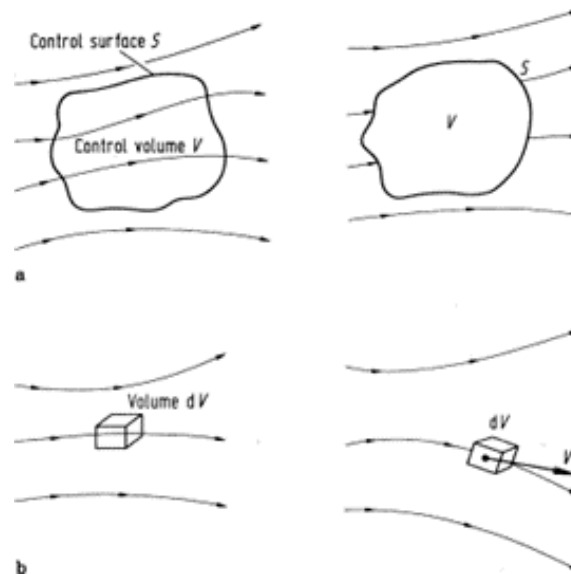


Figure 2.1. a left: Finite control volume approach - Eulerian representation, a right: Finite control volume approach - Lagrangian representation
 b left: Infinitesimal fluid element - Eulerian representation, b right: Infinitesimal fluid element - Lagrangian representation

2.1 Governing Equations

When the problem involves fluids there are a set of equations that can be utilized, to solve the flow fields of interest (velocity, pressure, vorticity, etc.). These equations are none other than the Navier-Stokes equations. The Navier – Stokes equations, consist of the conservation of mass, conservation of momentum, and conservation of energy. For this diploma thesis, the conservation of mass and momentum are the most important.

2.1.1 Conservation of mass: Continuity Equation

The conservation of mass is expressed in the continuity equation. Practically, the conservation of mass means the net in and outflow in any of the directions (x,y,z) should be equal to zero, assuming there is no mass source or sink. The differential form of the mass conservation or continuity equation is given by the following equation as a physical definition:

$$\left[\begin{array}{l} \text{Rate of mass entering through} \\ \text{the bounding surface of a volume} \end{array} \right] + \left[\begin{array}{l} \text{Rate of mass} \\ \text{generation in a volume} \end{array} \right] = 0$$

The above equation is expressed with mathematical terms in the following equation.

$$\frac{\partial \rho}{\partial t} + \nabla \cdot (\rho \vec{V}) = 0 \quad (2.1)$$

It is noted that the cartesian space is used for the governing equations presentation. There are several coordinate systems such as cylindrical and spherical that the equations can be expressed, but for this work the use of the cartesian coordinate system is sufficient.

The unit vectors along the x,y,z axis are \vec{i}, \vec{j} and \vec{k} respectively. The vector velocity field in this cartesian space is given by $\vec{V} = u\vec{i} + v\vec{j} + w\vec{k}$. Furthermore, the x, y, z components of velocity are given from the following expressions.

$$u = u(x, y, z, t), v = v(x, y, z, t), w = w(x, y, z, t) \quad (2.2)$$

The vector operator is defined as:

$$\nabla = \frac{\partial}{\partial x} \vec{i} + \frac{\partial}{\partial y} \vec{j} + \frac{\partial}{\partial z} \vec{k} \quad (2.3)$$

by applying the vector operator to a vector field, like velocity, the divergence of this field occurs.

Given the above, the divergence of a vector field is a scalar field that can be represented as:

$$\nabla \cdot \vec{V} = \frac{\partial u}{\partial x} + \frac{\partial v}{\partial y} + \frac{\partial w}{\partial z} = \text{div} \vec{V} \quad (2.4)$$

Thus, the equation 2.1 can be rewritten as follows by applying the equation 2.3.

$$\frac{\partial \rho}{\partial t} + \frac{\partial (\rho u)}{\partial x} + \frac{\partial (\rho v)}{\partial y} + \frac{\partial (\rho w)}{\partial z} = 0 \quad (2.5)$$

The equation 2.5 is the continuity equation in conservation form for an unsteady three-dimensional, compressible, viscous flows.

In the absence of any significant absolute pressure or temperature changes, it is acceptable to assume that the flow is incompressible; that is, the pressure changes do not have significant effects on density. This is almost invariably the case in liquids and is a good approximation in gases at speeds much less than that of sound. [39]

The incompressibility condition indicates that ρ does not change with the flow. This is equivalent to saying that the continuity equation for incompressible flow is given by:

$$\nabla \cdot \vec{V} = 0 \quad (2.6)$$

or in the expand form:

$$\frac{\partial u}{\partial x} + \frac{\partial v}{\partial y} + \frac{\partial w}{\partial z} = 0 \quad (2.7)$$

$\nabla \vec{V}$ is physically the time rate of change of the volume of a moving fluid element, per unit volume.

It is worth mentioning that the governing equations can be expressed by using several notations. Equation 2.6 represent the vector form of the continuity equation. The following equation represents the same equation but is now in tensor form. This form is also called the Einstein summation convention. The importance of using the Einstein notation arises from the fact that in computational fluid dynamics, the numerical solution of the partial differential equations is achieved by linearizing them into tensors. For that reason, in many books dealing with the numerical solution of equations, this form has prevailed. The continuity equation in tensor form is occurs by the following expression.

$$\frac{\partial u_i}{\partial x_i} = 0 \quad (2.8)$$

where, the velocity vector is given by u_i and the spatial vector is given by x_i .

2.1.2 Conservation of momentum: Navier Stokes momentum equation

Navier-Stokes equation, in fluid mechanics, is a partial differential equation that describes the flow of incompressible fluids. The equation is a generalization of the equation devised by Swiss mathematician Leonhard Euler in the 18th century to describe the flow of incompressible and frictionless fluids. In 1821 French engineer Claude-Louis Navier introduced the element of viscosity (friction) for the more realistic and vastly more difficult problem of viscous fluids. Throughout the middle of the 19th century, British physicist and mathematician Sir George Gabriel Stokes improved on this work, though complete solutions were obtained only for the case of simple two-dimensional flows. The complex vortices and turbulence, or chaos, that occur in three-dimensional fluid (including gas) flows as velocities increase have proven intractable to any but approximate numerical analysis methods.

The Navier-Stokes momentum equations (NS-equations) describes an momentum equilibrium in the flow. The formulation of the Navier-Stokes equations is shown in equations 2.9 to 2.11, for a 3-dimensional incompressible and Newtonian fluid. The derivation of these equations is achieved beginning from the Newtons second law and several mathematical handling and assumptions. The analytical derivation of the equation is not part of this work but this equations governs our problem. Therefore are mentioned for completeness reasons. The unknown variables in the Navier-Stokes equation are the velocities x , v , w and the pressure p , the remaining parameters in the equation are determined by the fluid surroundings and geometry.

$$x - axis : \rho \cdot \left(\frac{\partial u}{\partial t} + u \cdot \frac{\partial u}{\partial x} + v \cdot \frac{\partial u}{\partial y} + w \cdot \frac{\partial u}{\partial z} \right) = -\frac{\partial p}{\partial x} + \mu \left(\frac{\partial^2 u}{\partial x^2} + \frac{\partial^2 u}{\partial y^2} + \frac{\partial^2 u}{\partial z^2} \right) \quad (2.9)$$

$$y - axis : \rho \cdot \left(\frac{\partial v}{\partial t} + u \cdot \frac{\partial v}{\partial x} + v \cdot \frac{\partial v}{\partial y} + w \cdot \frac{\partial v}{\partial z} \right) = -\frac{\partial p}{\partial y} + \mu \left(\frac{\partial^2 v}{\partial x^2} + \frac{\partial^2 v}{\partial y^2} + \frac{\partial^2 v}{\partial z^2} \right) \quad (2.10)$$

$$z - \text{axis} : \rho \cdot \left(\frac{\partial u}{\partial t} + u \cdot \frac{\partial w}{\partial x} + v \cdot \frac{\partial w}{\partial y} + w \cdot \frac{\partial w}{\partial z} \right) = -\frac{\partial p}{\partial x} + \mu \left(\frac{\partial^2 w}{\partial x^2} + \frac{\partial^2 w}{\partial y^2} + \frac{\partial^2 w}{\partial z^2} \right) \quad (2.11)$$

The final form of N-S momentum equation is expressed with vector notation as follows dividing all parts with fluid density:

$$\boxed{\frac{\partial \vec{V}}{\partial t} + (\vec{V} \cdot \nabla) \vec{V} = -\frac{\nabla p}{\rho} + \nu \nabla^2 \vec{V}} \quad (2.12)$$

Where:

$$\nabla p = \left(\frac{\partial p}{\partial x}, \frac{\partial p}{\partial y}, \frac{\partial p}{\partial z} \right)^T$$

$$\Delta \vec{V} = \frac{\partial^2 \vec{V}}{\partial x^2} + \frac{\partial^2 \vec{V}}{\partial y^2} + \frac{\partial^2 \vec{V}}{\partial z^2} = \nabla^2 \vec{V} \text{ (which is the Laplacian operator)}$$

$$\vec{V} \nabla = u \cdot \frac{\partial}{\partial x} + v \cdot \frac{\partial}{\partial y} + w \cdot \frac{\partial}{\partial z}$$

and $\nu = \frac{\mu}{\rho}$, the kinematic viscosity of the fluid.

The following colorful expression explains briefly each term of the momentum Navier – Stokes equation. It is obvious, that the below equation is a consequence of Newton's second law as mentioned previously.

$$\underbrace{\rho}_{\substack{\text{MASS} \\ \text{Density} \\ \text{of the fluid}}} \cdot \underbrace{\left(\frac{\partial \vec{V}}{\partial t} + (\vec{V} \cdot \nabla) \vec{V} \right)}_{\text{ACCELERATION}} = \underbrace{-\nabla p + \mu \cdot \nabla^2 \vec{V}}_{\text{FORCE}}$$

Change in velocity over time
Speed and direction of fluid
Pressure gradient
Internal stress forces (viscous effects)

Equation 2.12 can also be expressed in the tensor form such as the equation of continuity as mentioned above. By using the Einstein convention of free indices equation 2.13 occurs.

$$\boxed{\rho \cdot \left(\frac{\partial u_i}{\partial t} + u_j \frac{\partial u_i}{\partial x_j} \right) = -\frac{\partial p}{\partial x_i} + \mu \frac{\partial^2 u_i}{\partial x_j \partial x_j}} \quad (2.13)$$

2.2 Computational Fluid Dynamics

Nowadays various ways to numerically calculate the flow field on internal or external flows. A couple of methods are stated from high calculation time to short; Direct Numerical Simulation (DNS), Large Eddy Simulation (LES), Reynolds-averaged Navier-Stokes (RaNS). On one end, DNS will simulate all the details in the flow, and on the other RaNS equations will give a time-averaged solution and thus the average flow. In this thesis in order to simulate the low-speed flow of air in the micro-channel under consideration, the two-dimensional unsteady incompressible fluid Reynolds Averaged Navier-Stokes (RaNS) equations were numerically solved.

2.2.1 Reynolds averaged Navier Stokes Equations (RaNS)

The RaNS equations are the result of time averaging the NS-equations and substituting the variables (velocity and pressure) by an average term and a fluctuation term. These are notated with \bar{u} and u' respectively (example for velocity u). The time scale used for averaging should be the largest time scale present in the problem. The flow of a viscous incompressible fluid with constant properties is governed by the Navier—Stokes equations as described previously. According to the concept of Reynolds decomposition, the dependent variables of N-S equations system are decomposed into mean and fluctuating parts: [3]

$$u_i = \bar{u}_i + u'_i, \quad p = \bar{p} + p' \quad (2.14)$$

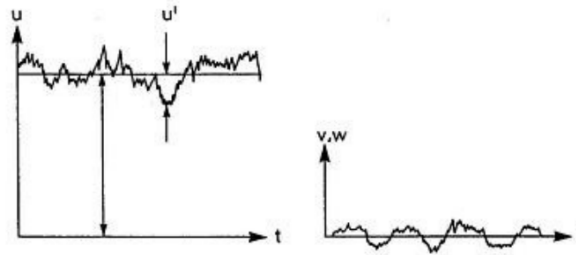


Figure 2.2. Turbulent velocity fluctuation in pipe flow as a function of time

After applying the Reynolds decomposition and averaging, of N-S equations system, the RaNS equations are obtained. It is noted that the derivation of these equations is not presented in the current work, but the reader may find plenty of sources in the literature.

$$\rho \frac{\partial \bar{u}_i}{\partial t} + \rho \frac{\partial}{\partial x_j} (\bar{u}_i \bar{u}_j) = -\frac{\partial \bar{p}}{\partial x_i} + \mu \frac{\partial^2 \bar{u}_i}{\partial x_j \partial x_j} - \frac{\partial \tau_{ij}}{\partial x_j} \quad (2.15)$$

$$\frac{\partial \bar{u}_i}{\partial x_i} = 0 \quad (2.16)$$

where: $\tau_{ij} = \rho \overline{u'_i u'_j}$ is the Reynolds-stress term that incorporates the effects of turbulent motions on the mean stresses. The Reynolds-stress tensor is symmetric, the diagonal components are normal stresses, and the off-diagonal components are shear stresses. Equation System 2.15, 2.16 is not a closed system for the calculation of the four dependent variables and in the sense that the Reynolds-stress tensor contains six additional independent unknowns. The problem of the closure of the Reynolds-averaged Navier—Stokes equations consists in expressing mainly through models the Reynolds-stress tensor as a function of the mean-field and/or other variables. In general, turbulence models are devised to represent high-order moments of the velocity fluctuations in terms of lower-order moments. This can be done directly, as in the case of the eddy-viscosity models, or

indirectly, as in the case of models (turbulence models) based on the solution of additional partial differential equations. [3].

2.2.2 Turbulence modeling

Physically, turbulence energy is generated in the largest vortex scales and transferred to medium scale vortices and dissipated in micro scale vortices. Turbulent vortices are complex and time intensive to model, but mostly only the average influence of the turbulence on the flow is desired. This turbulence model determines the time averaged Reynolds stresses in the flow (τ_{ij} part) and complete the RaNS equations.

Turbulence was taken into account by means of an eddy-viscosity turbulence model, namely the realizable variant of the k- ϵ two-equation model; this variant ensures that only physically realistic (realizable) viscous stresses will arise during the simulations. The equations for turbulent kinetic energy k and dissipation rate ϵ are given as follow:

$$\frac{\partial}{\partial t} (\rho k) + \frac{\partial}{\partial x_j} (\rho k u_j) = \frac{\partial}{\partial x_j} \left[\left(\mu + \frac{\mu_t}{\sigma_k} \right) \frac{\partial k}{\partial x_j} \right] + G_k - \rho \epsilon - Y_M + S_k \quad (2.17)$$

$$\frac{\partial}{\partial t} (\rho \epsilon) + \frac{\partial}{\partial x_j} (\rho \epsilon u_j) = \frac{\partial}{\partial x_j} \left[\left(\mu + \frac{\mu_t}{\sigma_\epsilon} \right) \frac{\partial \epsilon}{\partial x_j} \right] + \rho C_1 S \epsilon - \rho C_2 \frac{\epsilon^2}{k + \sqrt{\nu \epsilon}} + S_\epsilon \quad (2.18)$$

where:

G_k represents the generation of turbulence kinetic energy due to the mean velocity gradients, σ_k and σ_ϵ are the turbulent Prandtl numbers for k and ϵ equations, respectively, while S_k and S_ϵ are the source terms for k and ϵ equations, respectively. Finally, C_2 , C_1 , are model constants and C_1 is calculated by the following formula:

$$C_1 = \max \left[0.43, \frac{\eta}{\eta + 5} \right], \eta = S \frac{k}{\epsilon}, S = \sqrt{2 S_{ij} S_{ij}} \quad (2.19)$$

where S is the mean modulus of strain tensor, and the S_{ij} term is given by the following expression

$$S_{ij} = \frac{1}{2} \left(\frac{\partial u_j}{\partial x_i} + \frac{\partial u_i}{\partial x_j} \right) \quad (2.20)$$

The corresponding equation for the calculation of turbulent viscosity is:

$$\mu_t = \rho C_\mu \frac{k^2}{\epsilon} \quad (2.21)$$

2.2.3 Computational grids

The computational grid divides the flow field into a number of cells and defines at the same time the discrete points, at which the values of the variables will be calculated. Consequently, the way the grid is constructed is particularly important for solving a problem effectively. A variety of grids can be used in physical problems, such as structured or unstructured grids, while there is no restriction on the number and shape of the cells. In two-dimensional meshes the cells are usually triangles, as shown in the figure below, while in three-dimensional meshes the cells are usually tetrahedra or hexahedra, although there are cases of hybrid unstructured meshes with the presence of hexahedra, tetrahedra, prisms and pyramids in the same mesh.

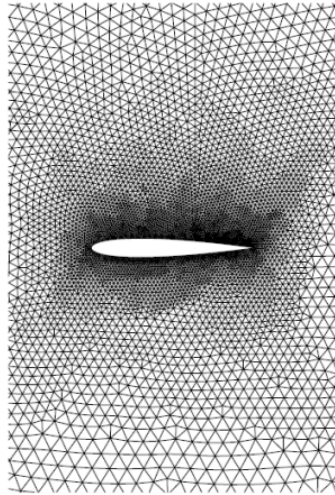


Figure 2.3. Unstructured grid around NACA 0012 airfoil in 2-dimensions

Unstructured grids have a lot of advantages in comparison with structured grids. In particular, unstructured approximate any complex geometry without significant problems, while, it is very difficult and time-consuming to generate structured meshes around complex geometries. Additionally, the grids generated in the second case may have strongly distorted cells, as a result of which errors are introduced into the final results from the very early stage of the computational domain discretization. Furthermore, another important advantage of structured grids is the ability of local intervention in the grid, in some regions where significant changes in the flow occur, such as boundary layer phenomena or shock waves. The above-mentioned local refinement of the unstructured computational mesh can be implemented during the solution of a problem, if significant transient phenomena appear in the flow, increasing the accuracy of the final results considerably. On the contrary, in the case of structured grids, the intervention should be performed on the entire mesh to maintain the character of the structured mesh.

The major disadvantage of unstructured meshes is the difficulty to handle them. As there is no sense of direction along the grid lines, an irregular connection of the cells occurs. Consequently, the lack of structure requires the creation of appropriate data structures, where the topological elements of the mesh will be stored. The creation of these structures as well as their handling is a time-consuming process, while at the same time it has high memory requirements from the working computer. An example of a two-dimensional unstructured grid is Figure 2.3, where the grid around a NACA 0012 airfoil is presented. The lack of structure is obvious, forcing the creation and storage of information such as the nodes of a triangle, the edges of a triangle, the nodes of edges, etc. In the present thesis, two-dimensional unstructured mesh was mainly used, which consists of triangular cells and is locally refined during the numerical solution of the problem. It is an extremely flexible mesh type, suitable for complex geometries, while in theory can be used with any discretization method, but it adapts much better to finite volume and finite element methods.

2.2.4 Spatial discretization methods

The choice of the appropriate discretization method is an important factor in solving the system of governing equations. Practically, the discretization method approximates the system of equations with a system of linear algebraic equations. The solution resulting from the aforementioned system of linear algebraic equations offers an approach to the solution of the system of partial differential equations at discrete points of the flow field. There are three main discretization methods listed herein.

- The finite difference method
- The finite elements method
- The finite volume method

All the above methods generally yield the same qualitative solution, if a high-density grid will be used. It is noted that the choice of method is mainly determined by the nature of the problem under consideration. In the framework of this work, the method of finite volumes was used, and a brief analysis of the main components of this method is discussed below.

The finite volume method is the main discretization method for solving computational fluid mechanics problems. The main advantage of this method is its ability to be applied to any type of computational grid and adapted to complex geometries as well. By definition, this method is conservative, as long as the surface integrals are the same on both sides of an interface. Additionally, all the calculated variables have physical substance, which contributes to the widespread use of the method. It is noted that the main disadvantage of the method is the difficulty in developing more accurate arithmetic schemes than the second order when three-dimensional unstructured grids are implemented. Nevertheless, the finite volume method (FVM) is a worldwide well-known spatial discretization method, which essentially transforms the complex system of differential equations into a solvable system of linear algebraic equations.

The FV method uses the integral form of the conservation equations as its starting point. The flow field or domain is subdivided, as in the finite element method, into a set of non-overlapping cells that cover the whole domain. In the finite volume method (FVM) the term cell is used instead of the term element used in the finite element method (FEM). The conservation laws are applied to determine the flow variables in some discrete points of the cells, called nodes. These nodes are at typical locations of the cells, such as cell-centres, cell-vertices or midsides. As mentioned in the previous paragraph, there is considerable freedom in the choice of the cells and the nodes. Cells can be triangular, quadrilateral, or other type. Furthermore, they can form a structured grid or an unstructured grid. Typical grids implemented in the finite volume method is shown in Figure 2.4 [14]

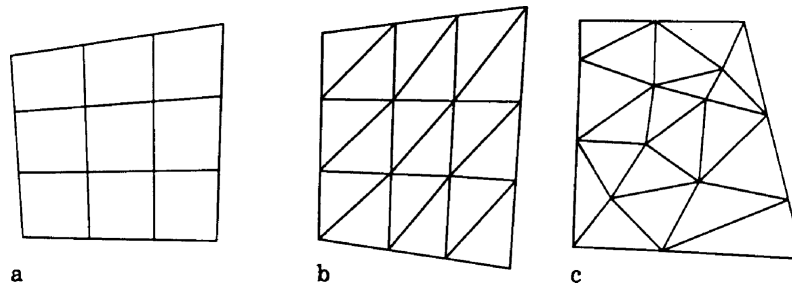


Figure 2.4. a: structured quadrilateral grid, b: structured triangular grid, c: unstructured triangular grid [14]

It is very important the selection of the volumes on which the conservation laws in the integral form are applied. In Figure 2.5 some possible choices of control volumes are shown shaded with lines. In the first two examples, control volumes coincide with cells. The third example in Figure 2.5 shows that the volumes on which the conservation laws are applied need not coincide with the cells of the grid. The volumes even can be overlapping. It is worth to mentioned that with the term volume the control volume to which the conservation laws are applied is denoted (the volumes are connected with functions). The term cell refers a mesh of the grid (connected to geometry determination). It is mandatory requirement for the cells to not overlapping and they should span the whole computational domain. This requirement is not mandatory for the volumes.

The volumes can be overlapping. The consistency requirement for all this procedure is the respect to the conservation laws, which means that a flux leaving a volume should enter another one. [14]

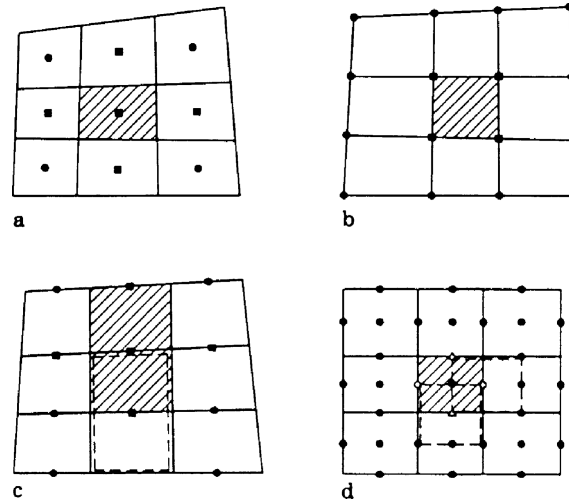


Figure 2.5. Typical choice of nodes in the FVM. The marked nodes are used in the flux balance of the control volume.[14]

2.2.5 Time discretization methods

Two distinct schemes for time discretization can be identified in computational modeling: explicit and implicit solvers. Explicit solvers utilize the values of the previous time steps to solve the equations, while implicit solvers employ the current time step for solving the equations. Generally, implicit solvers require more computational power per time step, but offer greater stability compared to explicit solvers. In this study, a first-order implicit scheme was implemented for the time discretization process for all the simulations.

2.3 Definition of Reynolds number

Reynolds number is one of the most important dimensionless quantities in fluid mechanics. It correlates the inertia forces to the viscous forces. The calculation of the Reynolds number for this thesis diploma is given by the following formula:

$$Re = \frac{\rho \cdot V_{inlet} \cdot D}{\mu} \quad (2.22)$$

where,

- ρ is the fluid density in $[kg/m^3]$,
- D is the characteristic length (bluff body width in our case) in [meters],
- V_{inlet} is the free stream velocity in $[m/s]$, and
- μ is the dynamic viscosity of the fluid in $[Pa.s]$.

2.4 Definition of Strouhal number for periodic flow motion

The Strouhal number is another very important ratio that plays a very dominant role in this dissertation having in mind the nature of the periodic flow created behind bluff bodies. According to [19], in general, the Strouhal number is the ratio of inertial forces due to the local acceleration of the flow divided by the inertial forces due to the convective acceleration. If we take into account the periodic motion of the flow the Strouhal number, in that case, is associated with the oscillations of the flow due to the inertial forces relative to the changes in velocity due to the convective acceleration of the flow field. The definition that will be used in this work is given by the following expression.

$$St = \frac{f \cdot D}{V_{inlet}} \quad (2.23)$$

where,

- f being the vortex shedding frequency in [Hz],
- V_{inlet} is the approach flow velocity or the free stream velocity in $[m/s]$
- D is the characteristic length (bluff body width in our case) in [meters]

Several researchers have studied the connection between Strouhal and Reynolds numbers by analyzing the flow past a cylinder and the measures data indicating the relation of Re and St are plotted in Fig. Figure 2.6 The different colors in the beforementioned plot indicate the different diameters of the cylinder which is used as the characteristic length. [19]

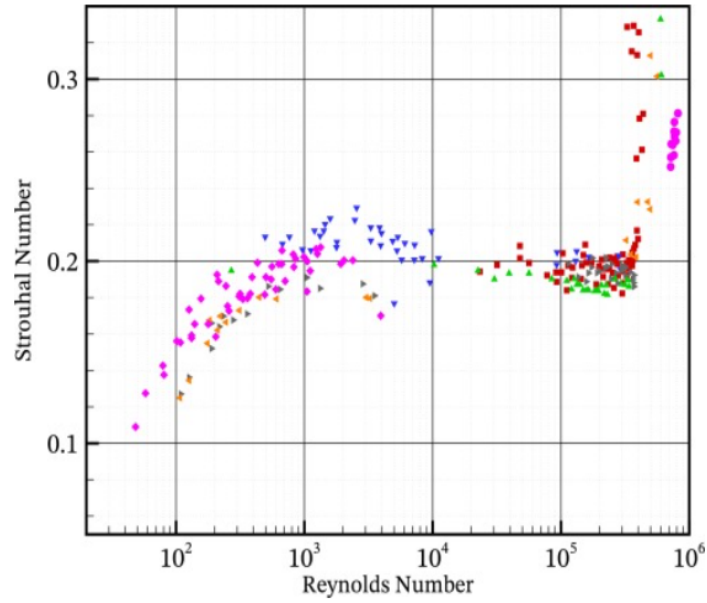


Figure 2.6. Variation of Strouhal number [19]

The main outcome from the Figure 2.6 is that for a wide region of Reynolds number (range of $Re \ 5 \cdot 10^2 < Re < 5 \cdot 10^5$) the data indicating a constant value of $St \simeq 0.2$. Furthermore, a sharp increase is observed at the end of the beforementioned Reynolds region (i.e for $Re < 10^2$), while at the low end of the range, the flow behind the cylinder seems to be laminar and the vortices last longer. Several periodic fluid motions in the nature are associated and described with the Strouhal number making it a very important quantity.

Chapter 3

Description of case studies and setup of the CFD model

This chapter deals with a more detailed presentation and explanation of the device proposed initially by Nguyen et al [26] and studied further by Koubogiannis [21] in 2016. In Chapter 1 Section 1.5 a short description of the main operating principles of the device under consideration was reported, and the key outcomes were presented and extracted by both experimentally and numerically simulations. By using these studies as a reference baseline case, a rebuild of the computational domain and geometry occurred to furtherly investigate the potential of this device by using numerical simulations to examine the periodic fluid motion in the channel. Given the above, in this chapter, a more detailed description of the geometry and flow domain will be presented by utilizing the modules of the commercial program ANSYS Fluent. Furthermore, a description of the setup of the CFD model regarding the implementation of the governing equations which formulate the problem, the numerical solver used by ANSYS Fluent, and turbulence modeling will be made in the basis of the equations presented in Chapter 2. One of the most important sections of the present chapter is the description of the various case studies which built this work. The spatial discretization of the flow domain using the meshing module of ANSYS Fluent will be described. Moreover, a discussion regarding the selection of time step (temporal discretization) will take place for the various case studies. In addition to the above, to evaluate the performance of the device several assumptions have been made to simplify the problem and they are described in this chapter along with the appropriate metrics that have been selected for the post-processing analysis and evaluation of results. Finally, a section containing step-by-step the setup of the CFD model in ANSYS Fluent will close this chapter. It is noted that the various case studies were set up following the steps, the same assumptions, and using the same software.

3.1 Description and production of the flow domain geometry

In CFD simulations some common steps are followed in all types of simulations, flows, and physical problems. In order to set up and study a problem in computational fluid mechanics, a necessary element is the correct and accurate production of the geometry. Computational fluid dynamics modeling is defined as the process of setting up a computer-based model to determine fields such as the flow field, pressure field, and other engineering quantities of interest as a result. In the below chart, the standard and most commonly implemented workflow of a simulation is presented.

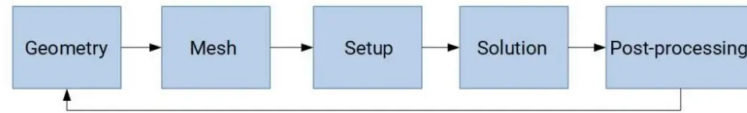


Figure 3.1. Typical CFD modeling workflow

As illustrated in Figure 3.1 the first step is to define the geometry of the problem to be solved, which generally comes from a CAD model or is integrated into the CFD software if a CAD module is available in the usage software. The flows in nature are categorized into two large categories, the internal and the external flows. In the first one the computational domain of the problem contains physical boundaries such as pipeline stationary walls, for example, flows into a pipeline or moving walls components such as pistons and valves in the internal combustion engines, while in the second one the boundaries are not physical walls and is typically a volume around the geometry of interest which should have adequate dimensions. In this work, the computational domain is determined by physical boundaries i.e the duct walls. As a result, in the present study, the computational domain is represented by the confines of the geometry itself.

An exploded view containing the construction dimensions of the device under examination proposed in the literature is shown in the Figure 3.2.

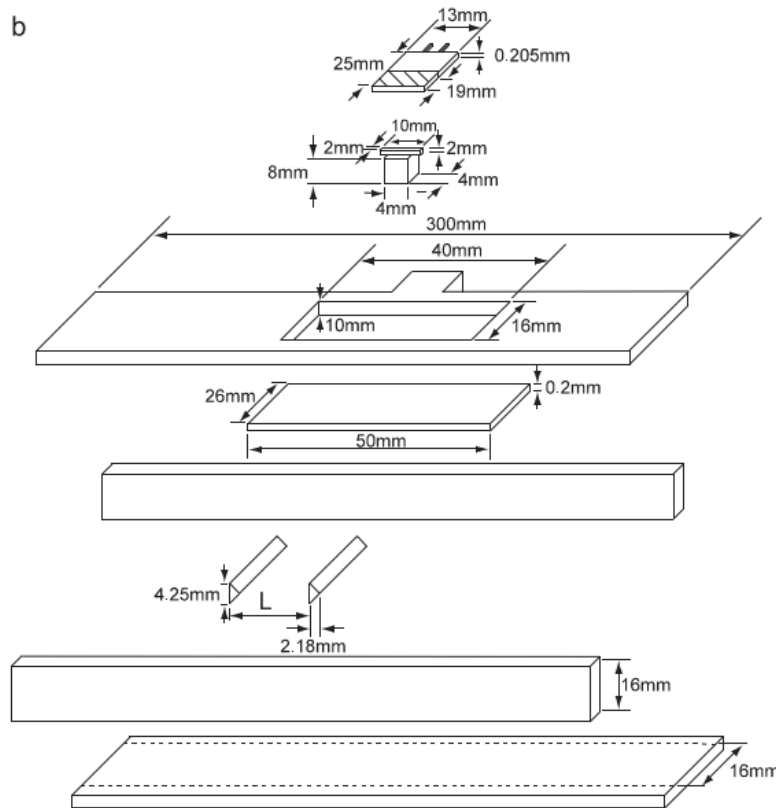


Figure 3.2. Exploded view of the energy generator proposed in [26]

It is obvious, that the beforementioned figure represents the device constructed by the authors and used in the experimental procedure. For the current analysis, a two-dimension (2D) computational domain is created by utilizing the key dimensions and arrangement of the original device as a first step of our investigation. For the creation of the geometry, the SpaceClaim module was used, provided as a CAD module of ANSYS Fluent commercial software. The bluff body shape is an isosceles triangle as discussed previously in Chapter 1, the base of which faces the incoming

flow from the left. All dimensions are expressed as a function of the bluff body's width which is $D = 4.25\text{mm}$, for the initially used configuration. The length of the channel is $L = 77.06D$, while its height is $H = 3.76D$. The blockage ratio which occurs from this dimension is defined as $BR = D/H = 0.27$. The flexible diaphragm is located on the upper wall of the channel. Its origin is just above the position of the first triangle base. The distance from the inlet of the flow domain to the origin of the diaphragm is $23.53D$, the length of the diaphragm is $8.94D$, while the distance from the diaphragm end to the flow outlet is $44.59D$. The whole upper and lower boundaries of the channel are treated as solid/stationary walls. The left boundary is the inlet of the flow domain and the right one is the outlet. More details about the boundary and initial condition of the problem will be given in the following section of the current chapter. Figure 3.3 below, reflects a sketch that visualizes the initial computational domain that corresponds to the first set of calculations (i.e. the baseline case).

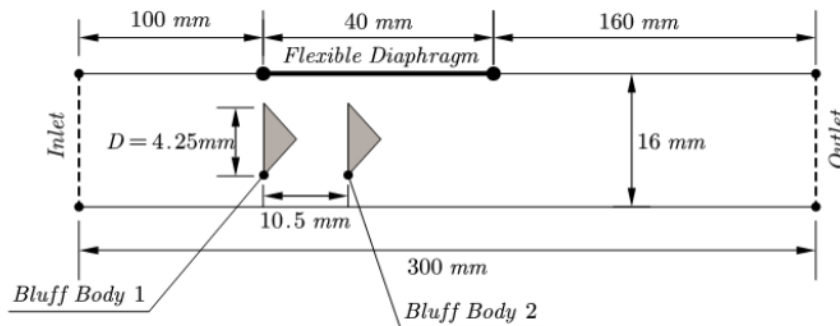


Figure 3.3. The computational flow domain used for the numerical simulations.

Following the presentation and description of the computational domain which is the same geometry due to the nature of the flow (internal flow), a detailed description of the geometry creation using the SpaceClaim of the ANSYS commercial software will take place.

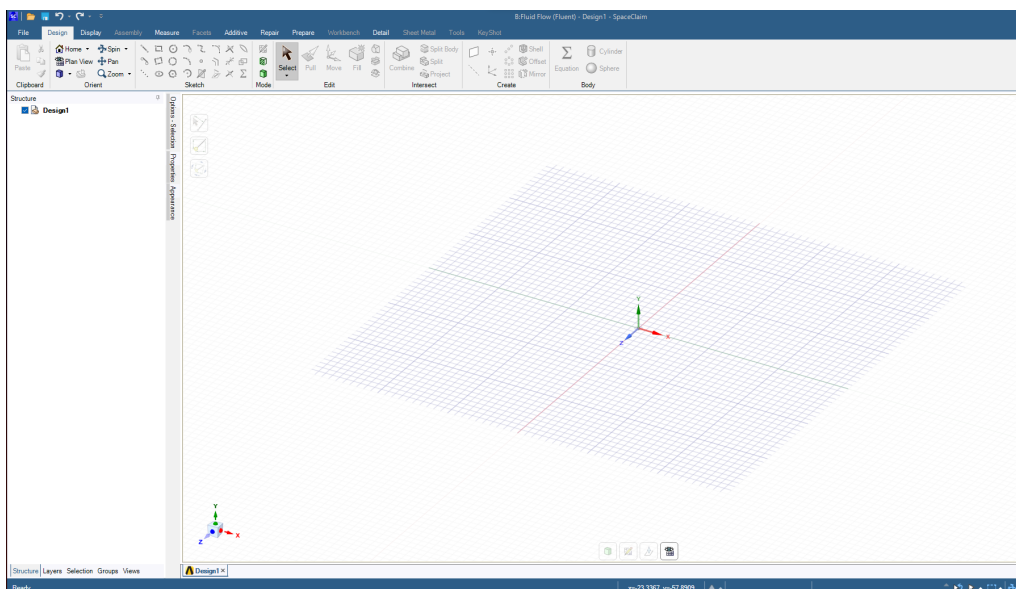


Figure 3.4. SpaceClaim GUI environment

The two dimension geometry creation for this particular problem is a very straightforward

process given that the mid-section of Figure 3.2 contains a rectangular with dimensions of $L \times H = 300\text{mm} \times 16\text{mm}$, and the two triangles' bodies as shown in Figure 3.2. After the creation of these elements, a splitting of the upper was necessary to create the flexible diaphragm 40mm in length.

The first step is the creation of a project from scratch and opening the node geometry where the creation of the computational domain takes place. On SpaceClaim, we choose the sketch mode from the toolbar ribbon and set the view on XZ plane. From the toolbar ribbon, a rectangular shape is chosen and the creation of the first part of the geometry is shown in Figure 3.5.

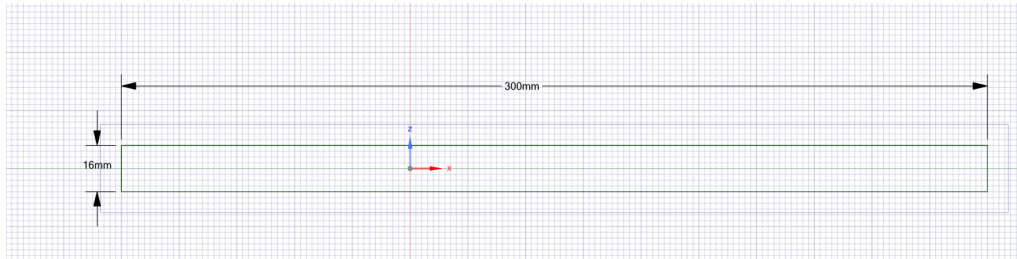


Figure 3.5. Creation of the computational domain 1/4

The second step is the creation of bluff bodies in a tandem arrangement and placing them in the right position inside the duct. The middle point of the base side of the aft triangle is positioned at the axis origin i.e 0,0. The width D of the triangles is equal to 4.25mm while their height is 2.18mm.

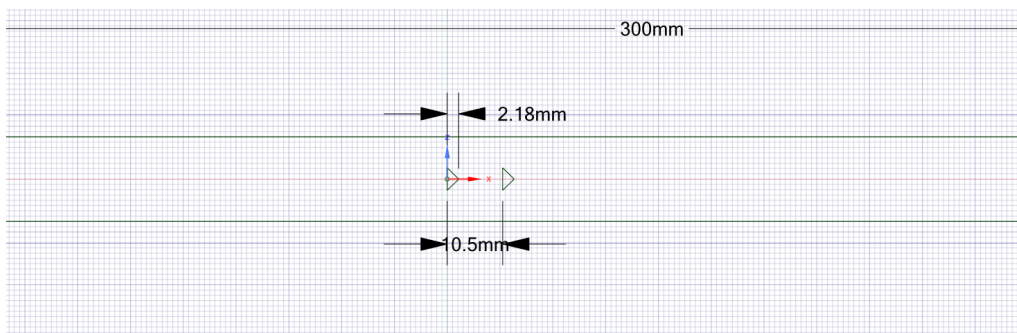


Figure 3.6. Creation of the computational domain 2/4

The third and final step is the assign parts to layers to be easier the handling of the walls for the mesh generation, which is the second step of the CFD analysis workflow.

The layers of the geometry consist of the upper wall which is divided into three parts, the lower wall which is divided into the same three parts, the inlet wall at the left of the domain, the outlet wall at the right of the domain, and finally the two bluff bodies walls. Namely, these parts are characterized as follows:

- upper wall left, with a length of 100mm. (red color)
- upper wall mid (this part represents the flexible diaphragm as per Figure), with a length of 40mm. (orange color)
- upper wall right, with a length of 160mm. (magenta color)
- lower wall left, with a length of 100mm. (green color)
- lower wall mid, with a length of 40mm. (black color)

- lower wall right, with a length of 160mm. (cyan color)

The reason that the lower wall is divided into the same three parts as the upper wall is for the easier operation and handling of the computational grid. The inlet wall (yellow color) is assigned in a separate layer such as the outlet wall (dark red color), and finally, the six triangle walls (navy blue color) are placed in a separate layer as well. The results and the final geometry is reflected in Figure 3.7 in sketch mode and in Figure 3.8 in the final surface mode ready for grid generation.

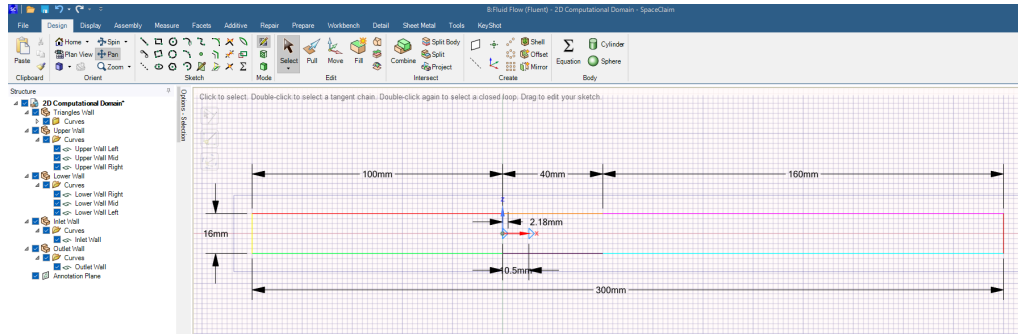


Figure 3.7. Creation of the computational domain 3/4

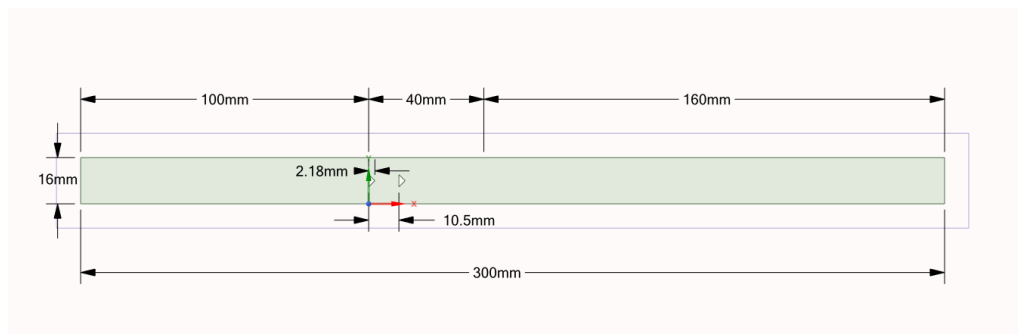


Figure 3.8. Creation of the computational domain 4/4 - Final 2D domain

3.2 Governing equations and numerical solver

In order to simulate the low-speed flow of air in the micro-channel, the two-dimensional unsteady incompressible fluid, two-dimensional Reynolds Averaged Navier-Stokes (RANS) equations were numerically solved, i.e. the continuity and momentum ones (the so-called mean-flow equations). Turbulence was taken into account by means of an eddy-viscosity turbulence model, namely the realizable variant of the $k-\epsilon$ two-equation model; the latter ensures that only physically realistic (realizable) viscous stresses will arise during the simulations [10]. The mean flow equations were solved by means of FLUENT software in the context of finite volume method in unstructured grids made of triangular elements, utilizing the SIMPLE pressure correction scheme. Second-order accuracy was used for the convective terms of the mean flow equations, while first order was used for the turbulence model ones. Transient solution of the governing equations was sought by means of first-order Euler scheme in time with a constant time step in physical time and 20 sub-iterations between two successive time steps. Inlet velocity was prescribed at the flow inlet boundary (termed ‘velocity inlet’ in FLUENT), while zero pressure value was set to the outlet boundary (termed ‘pressure outlet’). No-slip condition was used for the velocity at the channel walls and the bluff bodies. Wall functions were implemented to model velocity profiles at walls. In particular, the

option ‘scalable wall functions’ was used. This ensures that the wall distance employed in wall functions will be such that $y^+ > 11.126$, avoiding erroneous modelling of the laminar and buffer boundary layer regions (occurring in the range $y^+ < 11.126$) by effectively shifting the near-wall mesh point to $y^+=11.126$, irrespective the level of the actual near-wall grid refinement.

3.3 Description of case studies

In the present work, the effect of various parameters on the energy harvesting potential of the device under consideration is investigated. These parameters are the inlet Reynolds number (Re), and the blockage ratio (BR) of the bluff body width to the channel height. In particular, two different studies were carried out, concerning:

- The effect of blockage ratio and Reynolds number on the device performance.
- The value of blockage ratio causing suppression of vortex shedding.

In what follows, the various cases involved in these parametric studies are described and organized.

3.3.1 Cases to study the effect of blockage ratios and Reynolds numbers

The width of the bluff body D is the characteristic length of the flow. Thus, Reynolds number (Re) was based on the inlet velocity V_{in} and width D , i.e. $Re = \rho \cdot V_{in} \cdot D / \mu$. By writing D in terms of the blockage ratio BR, as $D = BR \cdot H$ (H is the channel width), the above formula becomes $Re = \rho \cdot V_{in} BR \cdot H / \mu$. Since air was used as the working fluid in all the simulations with a density of $\rho = 1.225 \text{ kg/m}^3$ and dynamic viscosity coefficient of $\mu = 1.789 \times 10^{-5} \text{ Pa}\cdot\text{s}$, for the baseline case studied in [21] (with $V_{in} = 20.7 \text{ m/s}$ and $BR = 0.27$), the Reynolds number was $Re = 6024$.

Apart from the baseline value $BR=0.27$ for blockage ratio, six more different BR values were simulated herein, i.e. seven cases in total. In addition, for each of these seven BR values, seven different Re numbers (named after C1,...,C7) were simulated, resulting in a total number of 49 simulations with respect to varying both Re and BR. In each of these cases, the inlet velocity was calculated according to the formula $V_{in} = (\mu \cdot Re) / (\rho \cdot BR \cdot H)$. Table 3.1 summarizes the values of the inlet velocity for the various values of Re and BR.

Case	C1	C2	C3	C4	C5	C6	C7	
Re	4278	4860	5442	6024	6606	7188	7770	BR
Vin (m/s)	16.3	18.5	20.7	22.9	25.1	27.3	29.6	0.24
	14.7	16.7	18.7	20.7	22.7	24.7	26.7	0.27
	13.0	14.8	16.6	18.3	20.1	21.9	23.6	0.30
	11.8	13.4	15.1	16.7	18.3	19.9	21.5	0.33
	10.8	12.3	13.8	15.3	16.7	18.2	19.7	0.36
	10.0	11.4	12.7	14.1	15.5	16.8	18.2	0.39
	9.3	10.6	11.8	13.1	14.4	15.6	16.9	0.42

Table 3.1. Inlet velocity for the various Reynolds numbers and blockage ratios.

3.3.2 Cases to find the value of blockage ratio causing suppression of vortex shedding

According to the literature, the increase of blockage ratio leads to increase of vortex shedding phenomenon; however, there is a value that causes suppression of vortex shedding [26]. In order to find this value, a number of simulations are required. In particular for this investigation a wide

range of BRs were studied between 0.240 and 0.663 and the results of the subject analysis will be given in Chapter 5. In these simulations, the baseline inlet velocity $V_{in}=20.7\text{m/s}$ was kept constant, while the generated mesh is similar to [26] for comparison purposes. Table 5.1 summarizes the different cases that were simulated for this investigation.

		Vin = 20.7 m/s													
BR	0.24	0.27	0.33	0.33	0.36	0.39	0.42	0.55	0.65	0.655	0.66	0.661	0.662	0.663	
Re	5443	6024	6804	7484	8164	8845	9525	12473	14741	14854	14968	14991	15013	15025	

Table 3.2. BR and Reynolds numbers with constant $V_{in} = 20.7\text{m/s}$

3.4 Fluid data for the simulations

Air was used as the working fluid in all the simulations. Air density was set to $\rho = 1.225\text{kg/m}^3$ and dynamic viscosity coefficient of air was set to $\mu = 1.789 \times 10^{-5}\text{Pa}\cdot\text{s}$. The Reynolds number based on channel width is greater than that based on body width, i.e. $Re_H = \rho V_{in}H/\mu > \rho V_{in}D/\mu = Re_D = Re$. According to Table 3.1, in all cases, $Re = Re_D$ is greater than the critical value Reynolds for ducts, namely 2300. This dictates turbulent flow in all of the cases that were simulated. In order to set boundary conditions for turbulence, the values of turbulence intensity I_t and turbulent length scale l_t were prescribed at the inlet. The latter was estimated, for fully developed flow, by the formula $l_t = 0.07D$. Turbulence intensity was computed by $I_t = 0.16(ReD)^{-1/8}$. A constant time step was used to march the flow-field evolution in physical time. A characteristic time scale of the problem at hand is the so-called ‘convective time’, defined by $T_C = D/V_{in}$. As in [26], a value of 5% of T_C , was used for the physical time step in the simulations, i.e. $\Delta t = \Delta t_c = (0.05)T_C$. For the baseline case (where $D = 0.00425\text{m}$ and $V_{in} = 20.7\text{m/s}$) this value was $\Delta t_{bsl} = 10^{-5}\text{s} = 0.01\text{ms}$. At each of the cases, starting from an ambient initial velocity field, the solution was marched using the corresponding physical time step for sufficient time to establish periodicity and then the flow field was let to evolve for at least three periods.

3.5 Assumptions involved in the simulation

All of the numerical simulations performed in the present work, rely on the following assumptions:

- The greater the vortex shedding intensity, the better the expected performance of the device.
- The flexible diaphragm is considered to be rigid wall, fluid-structure interaction phenomena are ignored, displacement of the fluid due to diaphragm motion is ignored and feedback effects from the diaphragm to the flow are neglected. (on this stage of analysis)
- The diaphragm has small inertia and was able to oscillate with the frequency of vortex shedding, the piezoelectric film is strained laterally following the vibrations of the diaphragm and, according to the piezoelectric phenomenon, produces electrical power.
- Although the actual geometry is three-dimensional, two-dimensional simulations along the symmetry plane of the channel were performed.

3.6 Definition of metrics to assess the energy harvesting potential of the device

The assessment of the flow energy harvesting potential in the present work, relied on some metrics. These are quantities of interest, either being indicative for assessing the potential to cause

greater effect on the piezoelectric membrane or characteristic quantities of the flow-field, like for example pressure drop along the channel. As time evolution of pressure acting on the center of the diaphragm exhibits periodicity, its fluctuation amplitude was considered as a criterion to comparatively assess the energy harvesting potential of the flow with such a device [26]. To monitor pressure evolution along the membrane, 21 distinct equidistant positions were defined along the diaphragm on the upper channel wall denoted by P1, P2, ..., P21 Figure 3.9. They serve to evaluate and compare local pressure evolution and estimate its amplitude, in order to assess energy harvesting potential by means of the piezoelectric membrane. The latter is expected to exhibit a better performance if the center of the membrane is located at the position experiencing the maximum pressure variation amplitude $p(t)$, $i=1, \dots, 21$.

In the light of the above, the selected metrics that are computed after establishing flow periodicity, are:

- The position $P_{i,max}$, where the maximum pressure fluctuation amplitude $\Delta p_{i,max}$ is predicted.
- The value of this maximum pressure fluctuation amplitude $\Delta p_{i,max}$. in a period, as well as the same quantity in non-dimensional form, namely as $C_{p,max} = \Delta p_{i,max} / 0.5\rho V_{in}^2$.
- The frequency and the nondimensional frequency of the above pressure signals, i.e. the Strouhal number $St = fD/V_{in}$.
- The average pressure drop Δp_{drop} in the duct in a period, calculated by the difference between inlet and outlet average pressures, as well as the same quantity in non-dimensional form, namely as $C_{p,drop} = \Delta p_{drop} / 0.5\rho V_{in}^2$.

The grid independence study for the baseline case, as well as the assessment of vortex shedding severity for various Reynolds numbers that are presented in the following chapters have been based on the above defined metrics.

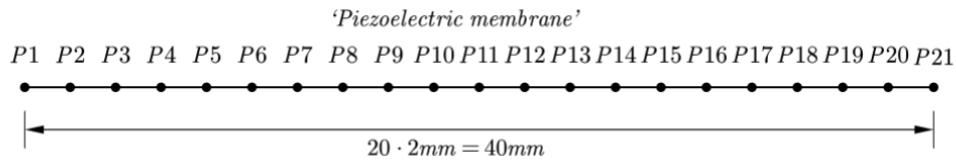


Figure 3.9. Positions P1, P2, ..., P21 along the diaphragm.

3.7 Selection of mesh size - mesh generation

The appropriate creation of the geometry (or the computational fluid domain) is one of the most important for mesh generation. As mentioned in Chapter 2 the quality of the mesh is reflected directly in the problem results. Meshing discretizes a complex object into well-defined cells where the governing equation can be assigned so that the solver can easily simulate physical behavior. The phrase "high-quality mesh" means that the mesh is fine and geometrically well-defined to ensure accuracy and convergence in speedy simulations. Therefore, Creating a high-quality mesh is key to the accuracy of the simulation. It is very crucial for CFD simulations, for the mesh geometry to be solid and watertight enough for the CFD solver to identify the appropriate flow domain for internal and external flow simulation. Additionally, a key parameter for mesh generation is the appropriate mesh density. It is generally true that higher mesh density produces a more accurate solution. Finer mesh can accurately depict the gradients. However, before increasing the mesh density, it is to be noted that more cells mean more time to solve the governing equation. This can take up more disk space and slow down the computational speed of the solver. This also raises

the question of cost-effectiveness. Thus, for an efficiency purposes, only the density near critical points with higher stress levels can be adjusted while keeping the overall cell size constant. This can increase the accuracy of the simulation while keeping the cost within limits. It is obvious that the final results connect directly with the mesh size, type, and density depending on the flow under consideration. In order to be sure of the mesh's satisfactory quality a mesh independence study should be performed. The mesh independence study helps to identify the mesh density required to achieve convergence. Once the result obtained by running the simulation has converged, the subsequent change in mesh size has little to no effect on the result. The result obtained from the convergence study has maximum accuracy for the given mesh. In this section, the process of the initial mesh generation will be presented step by step, utilizing the ANSYS Mechanical module for mesh generation.

For each ANSYS fluent problem, there is a list of actions to be followed in order to set up a CFD simulation using this solver. This list is shown in below Figure. It is obvious from the below that after the creation of the geometry the mesh generation is following.

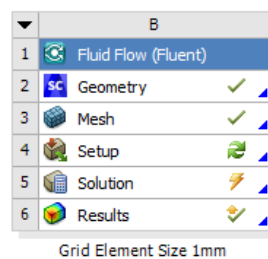


Figure 3.10. Step list for CFD simulations with ANSYS fluent

The below Figure reflects the graphical user interface on which the setup of grid generation has been done. The geometry is coming and translating automatically from the geometry tab and is ready for meshing.

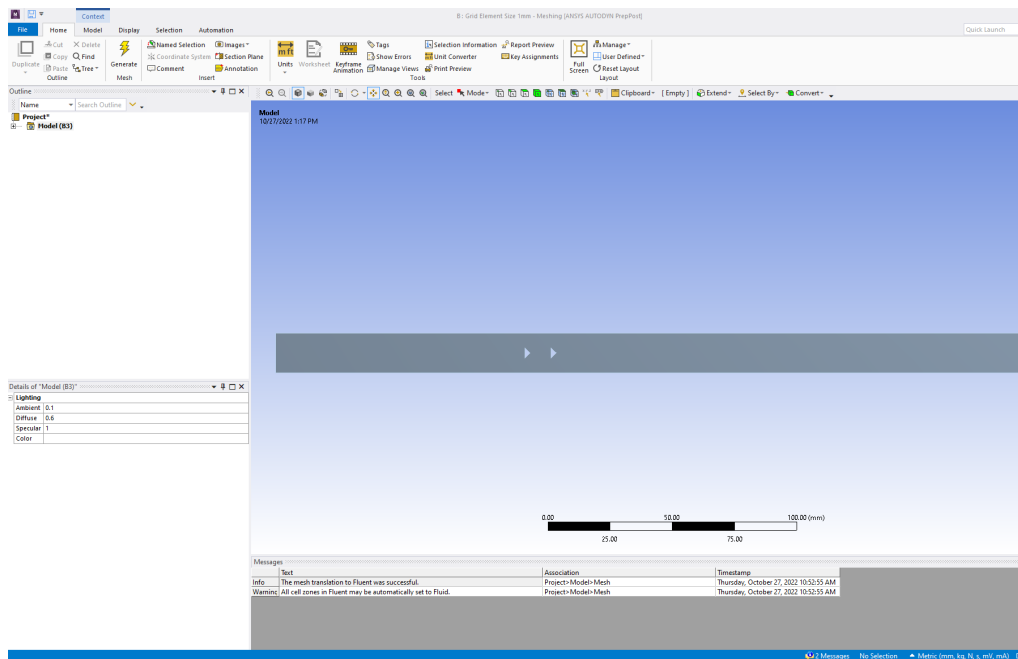


Figure 3.11. Mesh generation 1/3

In order to numerically simulate the flow in the channel and around the bluff bodies, the flow domain was discretized by means of an unstructured grid consisting of triangular elements by using the grid generation module of the academic version of FLUENT. The grid was made denser near the walls in order to better resolve the boundary layer regions. From the various grid metrics available in FLUENT, mainly the parameter named after ‘element size’ was used in this study. The geometry walls have been splitted on different layers in order to be easier for make the mesh denser in the interesting areas where we have significant changes in the flow. The above process is reflected on the Figure below. By utilizing the ‘mesh sizing’ option a denser grid have been created around the bluff bodies.

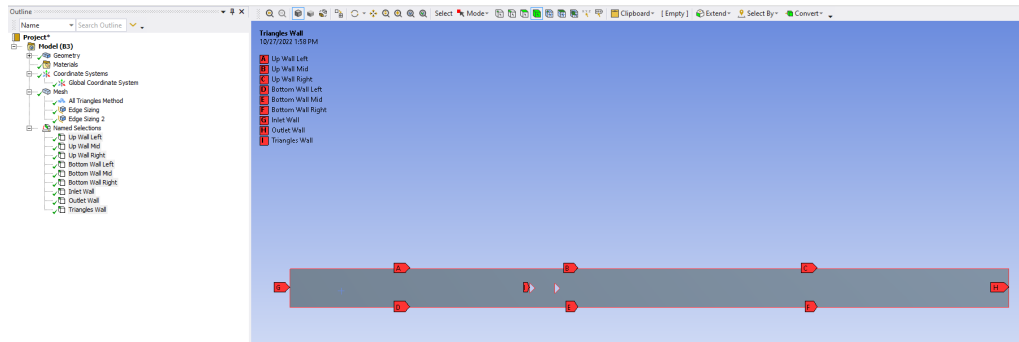


Figure 3.12. Mesh generation 2/3

The thickening of the mesh around the bluff bodies is achieved by dividing the four front edges into twenty divisions and the base edge into ten. The element thickness of the initial mesh is 1mm. The details of this operation depicted on the following figures.

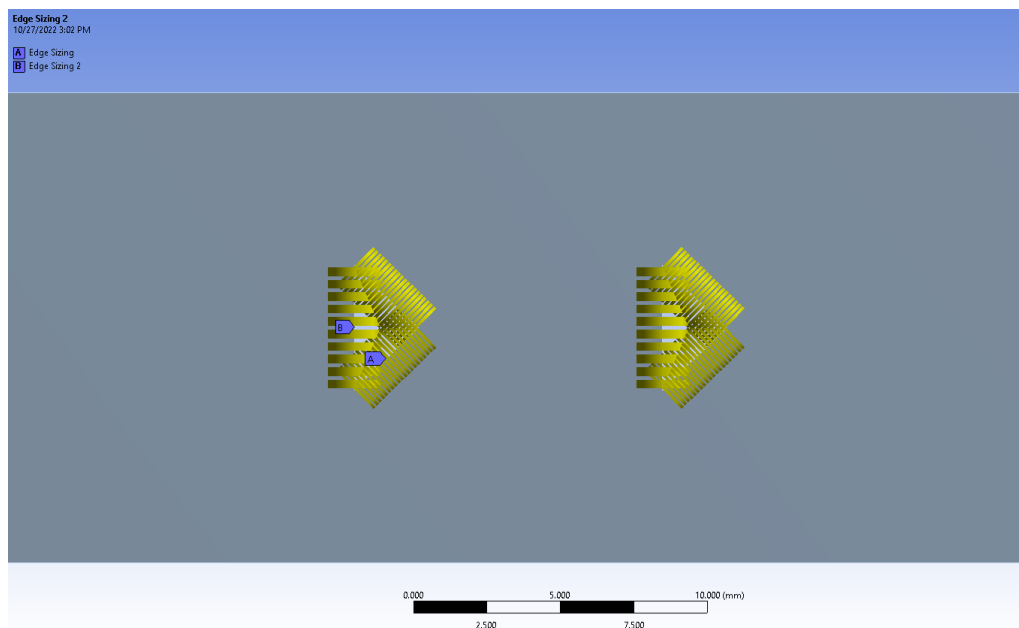


Figure 3.13. Mesh generation 3/3

Details of "Edge Sizing" - Sizing	
Scope	
Scoping Method	Geometry Selection
Geometry	4 Edges
Definition	
Suppressed	No
Type	Number of Divisions
<input type="checkbox"/> Number of Divisions	20
Advanced	
<input type="checkbox"/> Growth Rate	Default (1.2)
Capture Curvature	Yes
<input type="checkbox"/> Curvature Normal Angle	Default (18.0°)
<input type="checkbox"/> Local Min Size	Default (0.15015 mm)
Capture Proximity	No
Bias Type	No Bias

Figure 3.14. Denser mesh details on four front edges

Details of "Edge Sizing 2" - Sizing	
Scope	
Scoping Method	Geometry Selection
Geometry	2 Edges
Definition	
Suppressed	No
Type	Number of Divisions
<input type="checkbox"/> Number of Divisions	10
Advanced	
<input type="checkbox"/> Growth Rate	Default (1.2)
Capture Curvature	Yes
<input type="checkbox"/> Curvature Normal Angle	Default (18.0°)
<input type="checkbox"/> Local Min Size	Default (0.15015 mm)
Capture Proximity	No
Bias Type	No Bias

Figure 3.15. Denser mesh details on two base edges

At this stage, all required settings have been completed and the next step is the generation of the computational grid on the domain. Figure 3.16 is shown the generated mesh for the computational domain with an element size of 1mm. Figure 3.17 reflects the mesh around the bluff bodies which is denser. Finally, in Figure 3.18 all details concerning the main mesh of the domain are listed.

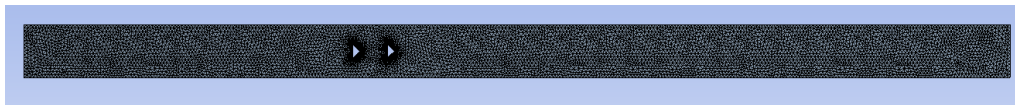


Figure 3.16. Final initial mesh

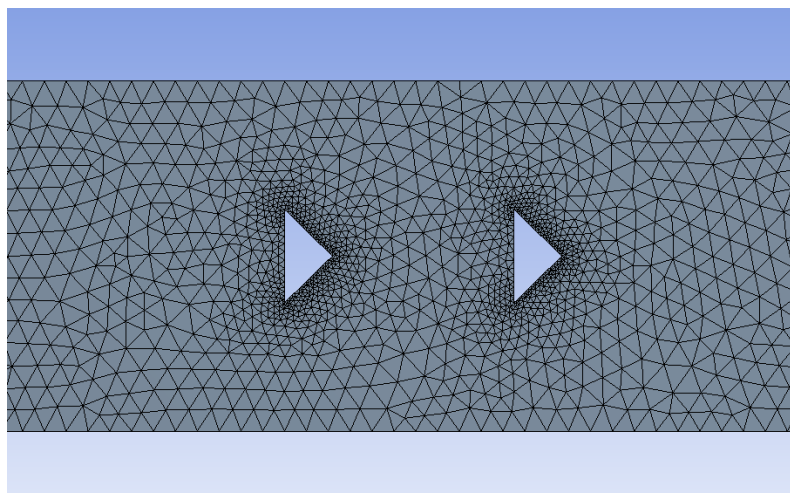


Figure 3.17. Denser mesh around bluff bodies

Details of "Mesh"		Inflation	
Display		Use Automatic Inflation	None
Display Style	Use Geometry Setting	Inflation Option	Smooth Transition
Defaults		<input type="checkbox"/> Transition Ratio	0.272
Physics Preference	CFD	<input type="checkbox"/> Maximum Layers	2
Solver Preference	Fluent	<input type="checkbox"/> Growth Rate	1.2
Element Order	Linear	Inflation Algorithm	Pre
<input type="checkbox"/> Element Size	1.0 mm	View Advanced Options	No
Export Format	Standard	Batch Connections	
Export Preview Surface Mesh	No	Mesh Based Connection	No
Sizing		Assembly Meshing	
Use Adaptive Sizing	No	Method	None
<input type="checkbox"/> Growth Rate	Default (1.2)	Advanced	
Mesh Defeaturing	Yes	Number of CPUs for Parallel Part Meshing	Program Controlled
<input type="checkbox"/> Defeature Size	7.5074e-002 mm	Straight Sided Elements	
Capture Curvature	Yes	Rigid Body Behavior	Dimensionally Reduced
<input type="checkbox"/> Curvature Min Size	0.15015 mm	Triangle Surface Mesher	Program Controlled
<input type="checkbox"/> Curvature Normal Angle	Default (18.0°)	Topology Checking	Yes
Capture Proximity	No	Use Sheet Thickness for Pinch	No
Bounding Box Diagonal	300.43 mm	Pinch Tolerance	Default (0.13514 mm)
Average Surface Area	4790.7 mm ²	Generate Pinch on Refresh	No
Minimum Edge Length	3.0443 mm	Sheet Loop Removal	No
Quality		Statistics	
Check Mesh Quality	Yes, Errors	<input type="checkbox"/> Nodes	6415
<input type="checkbox"/> Target Skewness	Default (0.900000)	<input type="checkbox"/> Elements	12086
Smoothing	Medium		
Mesh Metric	Element Quality		
<input type="checkbox"/> Min	0.64221		
<input type="checkbox"/> Max	0.99999		
<input type="checkbox"/> Average	0.96581		
<input type="checkbox"/> Standard Deviation	3.4509e-002		

Figure 3.18. Final initial mesh details

From the various tabs of the above table with mesh details, important information for mesh quality like sizing and statics is given. The initial mesh consists of 6415 nodes and 12086 triangular elements.

3.7.1 Denser meshes generation for mesh independence study

A mesh independence study is a method of investigating, whether the simulation results are independent of the underlying mesh or not. This is done by running a few simulations with different mesh resolution and checking if the results changes. This type of investigation is critical in CFD due to the mechanics of CFD simulations and the underlying mathematics. Following the procedure described in Section 3.7, a series of seven grids in total were generated to facilitate grid independence study for the case under consideration. Table 3.3 summarizes the name, size, and corresponding value of the mesh size parameter for each of the seven grids. Figure 3.19 presents comparative partial views of the grid region near the bodies for the grids corresponding to the mesh size parameter values of all generated grids involved in the mesh independence study.

Name	$G_{1.0}$	$G_{0.7}$	$G_{0.5}$	$G_{0.4}$	$G_{0.3}$	$G_{0.25}$	$G_{0.2}$
Mesh size (mm)	1.00	0.70	0.50	0.40	0.30	0.25	0.20
Nodes	6415	12623	21433	30490	56529	87216	105783
Elements	12086	24230	41491	59288	110840	171737	208238

Table 3.3. Mesh sizes

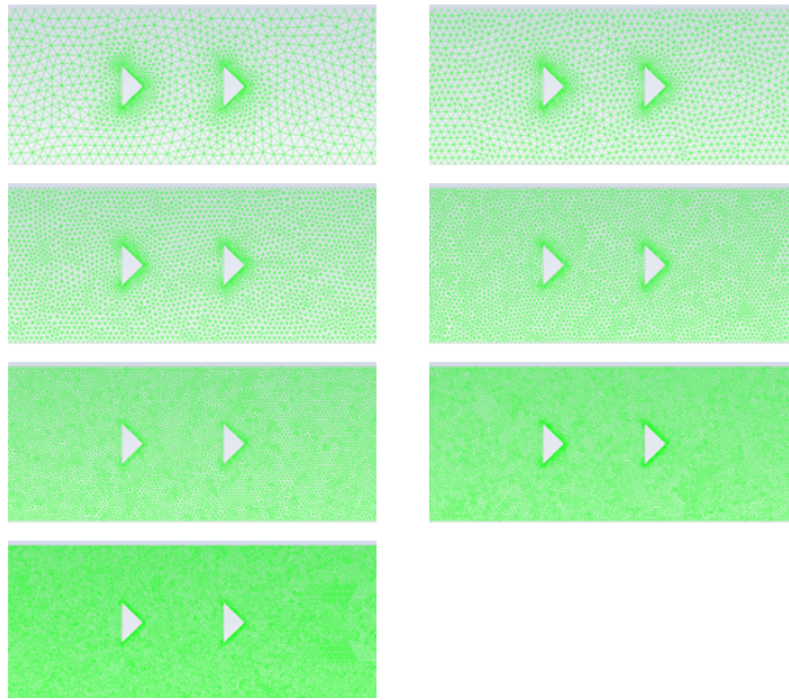


Figure 3.19. Grids corresponding to mesh size values of 1mm (top left) to 0.2mm (bottom left).

The results of the mesh independence analysis for the spatial discretization will be given in the section below.

3.7.2 Mesh independence study results

The first study concerns the mesh independence of the results; this study was performed for the baseline case. In particular, according to the definitions given in the previous sections, case C4 was simulated in all of the grids described in Table 3.3 (i.e. $G_{1,0}$ to $G_{0,2}$). It is noted that the case C4 corresponds to a two dimensional simulation utilizing the realizable k-epsilon turbulence model with wall functions. The Reynolds number is considered constant and equal to $Re=6024$, while the blockage ratio of the channel was also kept constant and equal to $BR = 0.27$. The main outcome of this evaluation is that the generated grid with an element size of 0.3mm is sufficient to capture the flow changes of the case under consideration. The mesh independence study is a significant part of the CFD setup, thus the results of this analysis are presented in this section. To complete this study, 7 runs were performed in total. The results evaluation was based on pressure evolution in time, at the point where the maximum evolution occurs, and the pressure drop in the channel, were considered as the quantities of interest, and thus the mesh independence analysis was based on these quantities.

Figure 3.20 presents the pressure fluctuation amplitude for points P1-P21 for each of the seven grids $G_{1,0}$ to $G_{0,2}$. According to it, the position of maximum pressure fluctuation amplitude along the diaphragm for the first two grids, namely $G_{1,0}$ and $G_{0,7}$ appears to be at position P8, while in all the rest finer grids it occurs at point P5, i.e. at a distance $1.88D=8\text{mm}$ from the beginning of the diaphragm.

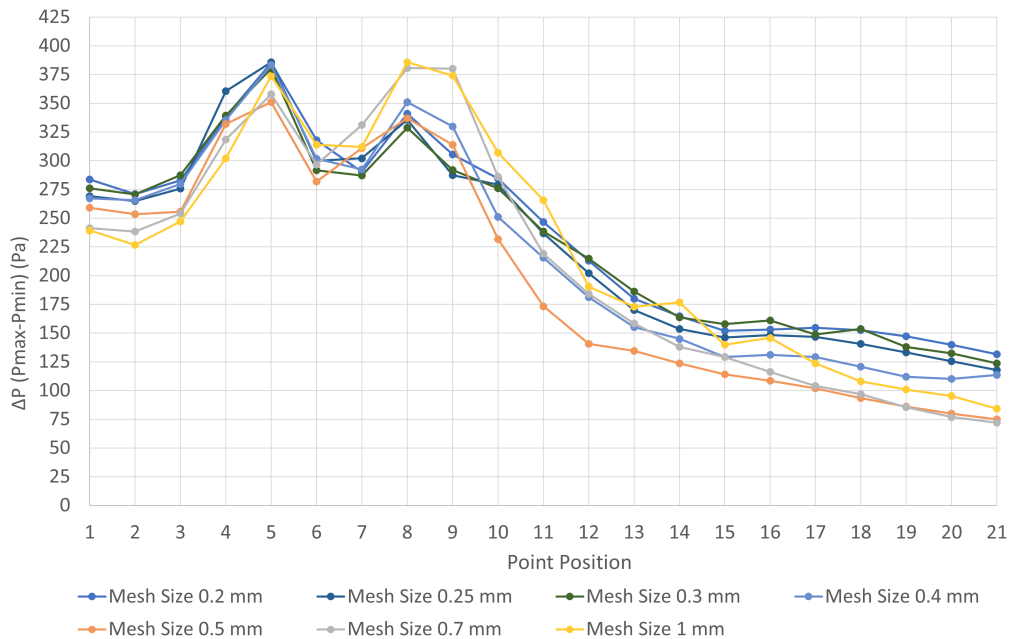


Figure 3.20. Position of maximum pressure fluctuation amplitude along the diaphragm for various grid sizes.

Pressure drop time evolution between inlet and outlet of the duct also attains periodicity in time. Figure 3.21 presents average pressure drop in time as it was predicted for the various grid sizes. This quantity seems to stop changing significantly after grid G0.3.

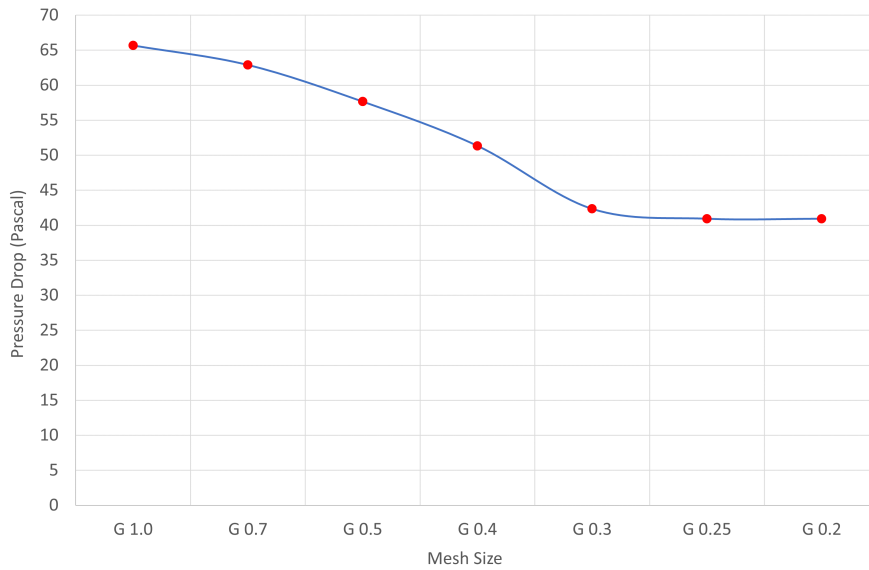


Figure 3.21. Average pressure drop in time predicted for the various grid sizes.

In addition to the above mesh independence indicators, Figure 3.22 presents the local pressure evolution in time computed in grids $G_{1.0}$ to $G_{0.3}$, at the point where the maximum amplitude of pressure fluctuation is predicted, for most generated grids i.e. Point 5. Since this is considered to be a critical quantity in the present study, grid independence was mainly based on it. It has to be mentioned that the pressure signal curves have been translated and shifted in time in order to be comparable to each other. According to this figure, it becomes clear that, for the various grids from $G_{1.0}$ to $G_{0.3}$, a different resolution of pressure is exhibited.

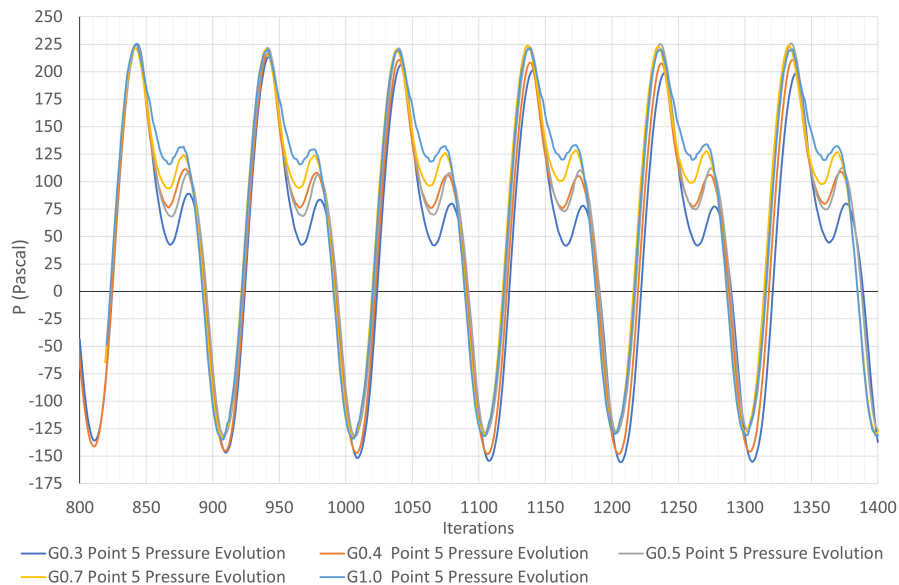


Figure 3.22. Local pressure evolution in time for grids $G_{1.0}$ to $G_{0.3}$ at point P5

Similarly, Figure 3.23 presents the local pressure evolution in time for the grids from $G_{0.3}$ to $G_{0.3}$ at point P5. According to this figure, for these three grids, practically the same resolution of pressure is achieved. Having in mind these results it could be said that the local pressure evolution over time seems to stop changing significantly after grid $G_{0.3}$. According to the above analysis,

grid $G_{0.3}$ was considered to be sufficient for obtaining a grid-independent solution in the case under consideration as said in the beginning.

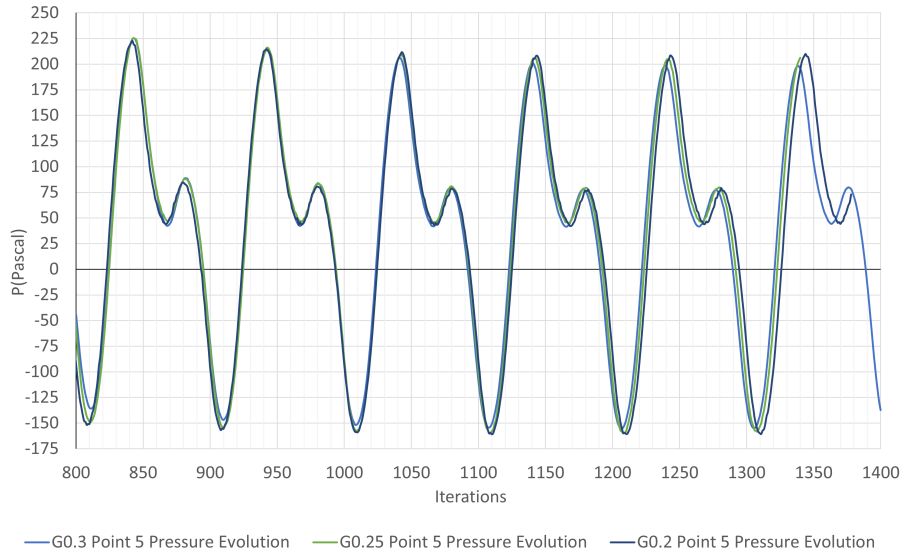


Figure 3.23. Local pressure evolution in time for grids $G_{0.3}$ to $G_{0.2}$ at point P5

For the sake of completeness, it has to be mentioned that in order to assess the necessity of using ‘scalable wall functions’, the value of y^+ was computed in a number of simulations. In particular, minimum y^+ was found to be between 0.3-1.1 and maximum y^+ was found to be in the range 17.3-74.0 for the various grids used to simulate baseline case. Similarly, minimum y^+ was between 0.3-1.1 and maximum y^+ was in the range 17.1-27.2 for the seven different Reynolds numbers in the case with $BR=0.27$ when using grid $G_{0.3}$. Thus, in all cases, the aforementioned minimum values justify the use of the selected approach.

3.8 Time step selection - temporal discretization

According to what described in section 3.4, the time step for each simulation was to be calculated as $\Delta t_c = 0.05(D/V_{in})$. So, in [10], where all the numerical simulations concerned the baseline case ($Re=6400$, $BR=0.27$), the time step value of $\Delta t_{bsl} = 10^{-5}s$ was used. Due to the fact that $V_{in} = (\mu \cdot Re)/(\rho \cdot D)$, the previous formula can be written as $\Delta t_c = 0.05(\rho \cdot D^2)/(\mu \cdot Re)$ and by taking into account that $D = BR \cdot H$, the final formula for time step as a function of Re and BR is written in the form $\Delta t_c = \Delta t_c(Re, BR) = 0.05(\rho \cdot BR^2 H^2)/(\mu \cdot Re)$. According to this, Δt_c decreases with the decrease of BR and the increase of Re (for lower BR values and higher Re values).

In the present study, Δt_c was computed for each of the cases concerning the parametric studies with respect to Re and BR . This value was compared with Δt_{bsl} and the cases where Δt_c was found to be lower than Δt_{bsl} , i.e. $\Delta t_c < \Delta t_{bsl}$, were identified. These were only a few, namely those with $BR = 0.24$ for $Re > 4830$ (5 cases, namely C3-C7) and those with $BR = 0.27$ for $Re > 6024$ (3 cases, namely C5-C7). For these cases, appropriate comparisons were made in order to assess the effect of time step on the resolution of the flow-field so as to decide if the use of Δt_{bsl} for all cases is sufficient or the corresponding value of Δt_c had to be considered. For these cases, appropriate comparisons were made in order to assess the effect of time step on the resolution of the flow-field so as to decide if the use of Δt_{bsl} for all cases is sufficient or the corresponding value of Δt_c had to be considered. The comparison was made in terms of the pressure evolution on point P5, where,

as it will be shown in the results section, the maximum local pressure fluctuation on the membrane occurs, in all cases. All calculations were performed in the $G_{0.3}$ grid.

Figure 3.24 compares the local pressure evolution in time at point P5 for $BR = 0.24$ and cases C3-C7, as predicted by using $\Delta t = \Delta t_{bsl} = 10^{-5}s$ (blue curve) with that obtained by using $\Delta t = \Delta t_c < \Delta t_{bsl} = 10^{-5}s$ (red curve). It is obvious that as Re increases the discrepancy between the two curves becomes more significant. The same remark can be made in Figure 3.25, where again the local pressure evolution in time at point P5 for $BR = 0.27$ and cases C5-C7, is compared between results predicted by $\Delta t = \Delta t_{bsl} = 10^{-5}s$ (blue curve) and $\Delta t = \Delta t_c < \Delta t_{bsl} = 10^{-5}s$ (red curve). According to the above comparisons, it becomes evident that the resolution of the flow-field in terms of pressure in the simulations with the different time steps is not the same. In the 8 cases that $\Delta t_c < \Delta t_{bsl}$, the lower value (Δt_c) was obviously considered to provide more accurate results (instead of Δt_{bsl}). As a consequence, the time step in each run was finally defined according to the formula $\Delta t = \min \{ \Delta t_c, \Delta t_{bsl} \}$.

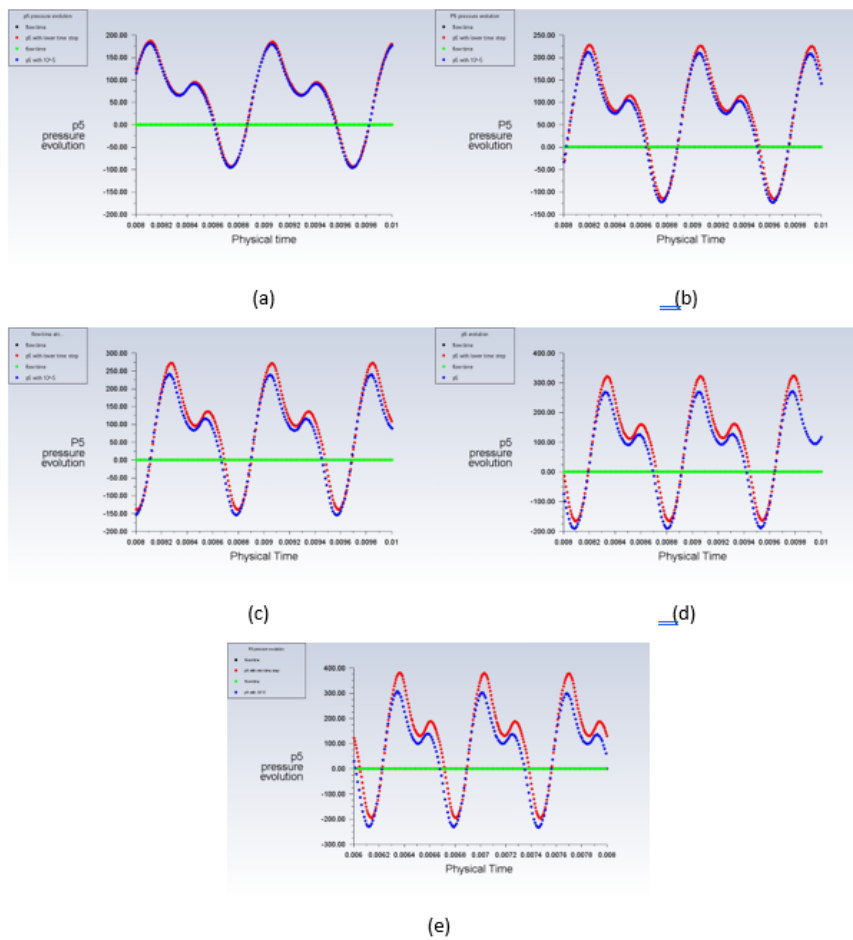


Figure 3.24. Local pressure evolution in time at point P5 for $BR=0.24$ and case (a) C3, (b) C4, (c) C5, (d) C6, (e) C7. The blue curve concerns results obtained with $\Delta t = \Delta t_{bsl} = 10^{-5}s$, while the red one corresponds to results obtained with $\Delta t = \Delta t_c < \Delta t_{bsl} = 10^{-5}s$.

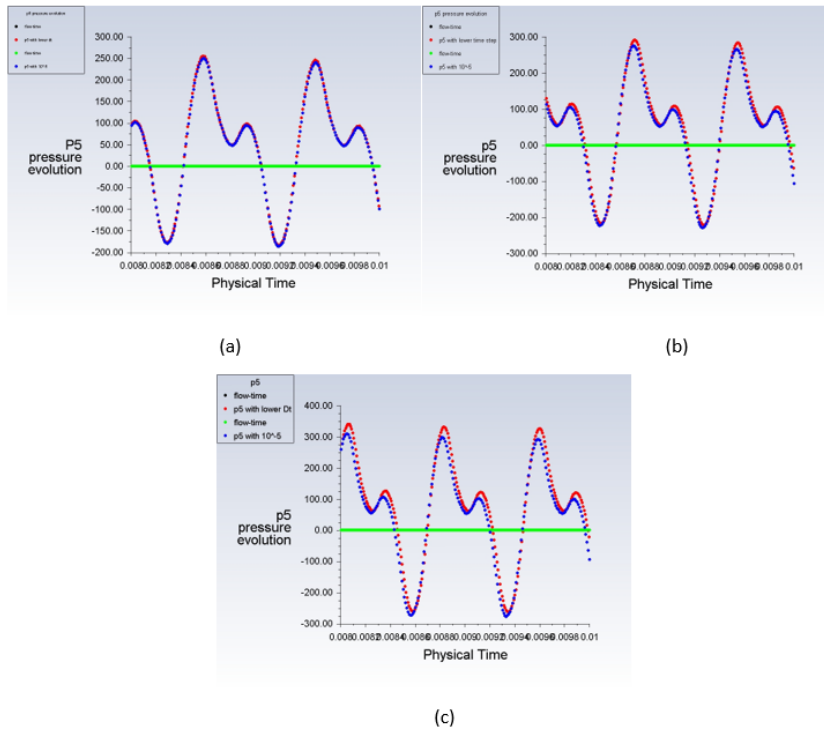


Figure 3.25. Local pressure evolution in time at point P5 for BR=0.27 and case (a) C5, (b) C6, (c) C7. The blue curve concerns results obtained with $\Delta t = \Delta t_{bsl} = 10^{-5} s$, while the red one corresponds to results obtained with $\Delta t = \Delta t_c < \Delta t_{bsl} = 10^{-5} s$.

3.9 Set up of Fluent model

Upon the mesh generation and the definition of the boundaries, the next step is the setup of the model in the ANSYS Fluent environment. This step corresponds to step three of the list as reflected in Figure 3.10. The parameters and settings used in the setup of the model were based on the description given in Section 3.2. The graphical user interface of the model setup menu is shown in the below figure.

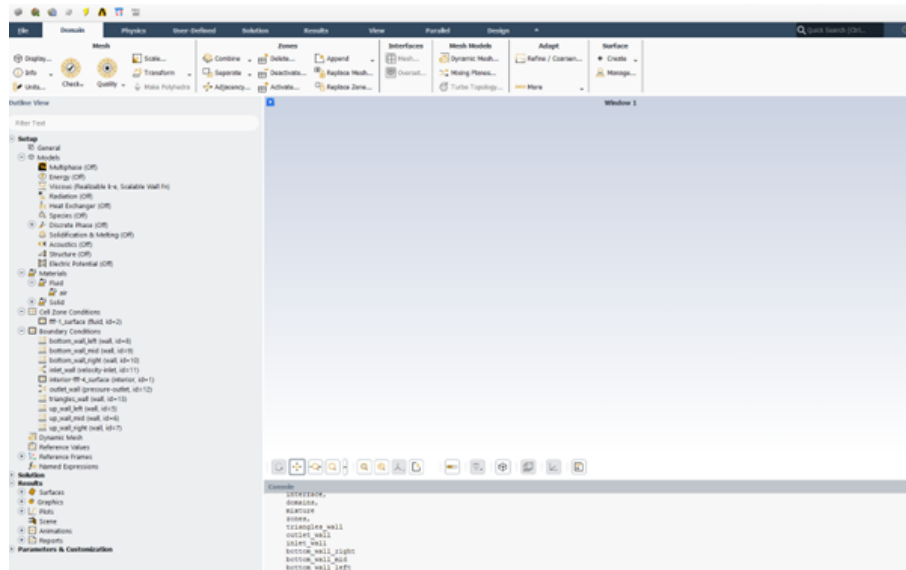


Figure 3.26. ANSYS Fluent graphical user interface

The left side tree leads the setup process through several nodes such as set up, where the appropriate physical models, materials, and boundary conditions are defined. The next node is the solution where the definition of the various metrics (reports definitions), figures (report plots), solution methods (e.g SIMPLE algorithm), time step, and other key parameters of the solution process are carried out. The final node is the results node, where the post-processing of the solved problem takes place. The results presentation and evaluation are carried out with XY plots such as pressure evolution in time, and contour representations of the flow field of interest such as velocity, pressure, and vorticity fields in specified time of the solution. In this section, a short description of the chosen models and corresponding parameters will be presented for the baseline case i.e $BR = 0.27$ and inlet velocity of $20.7m/s$.

Firstly the definition of the viscous model should be enabled. The viscous model dialog box allows us to set parameters for inviscid, laminar, and turbulent flow. In our case, the flow is turbulent, thus the selection of the turbulence model is activated. As already mentioned in Chapter 2 the turbulence model implemented in our problem is the Realizable k-epsilon two equations model, and for the near wall treatment, the scalable wall functions were chosen as mentioned in Section 3.2. The purpose of scalable wall functions is to force the usage of the log law in conjunction with the standard wall functions approach. The specific dialog box of the viscous model, turbulence model, and near-wall treatment definition is shown below.

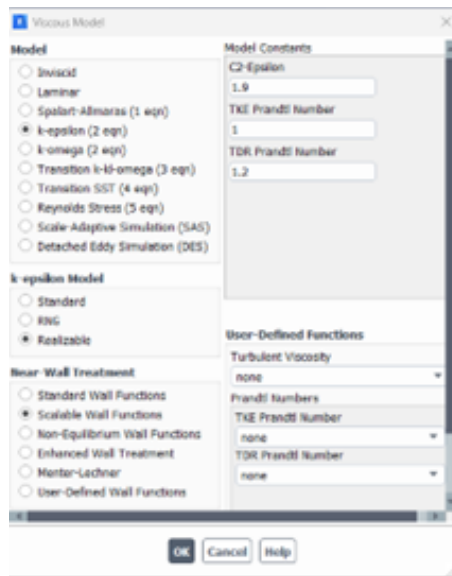


Figure 3.27. Set up of turbulence model and wall treatment

The next step is the definition of the working fluid, which in our case is air, with standard properties, as described in Section 3.4. The corresponding dialog box of the working fluid definition is presented in the following Figure.

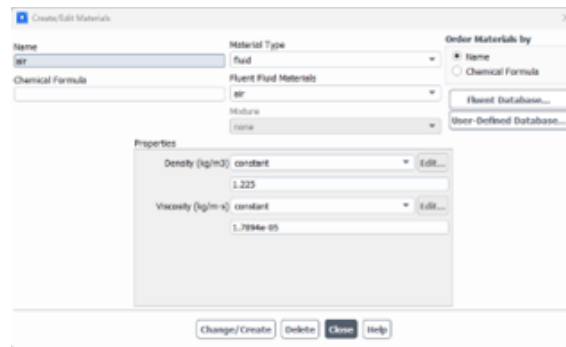


Figure 3.28. Working fluid definition

The computational domain boundaries consist mainly of stationary no-slip walls. The roughness of the walls was not taken into consideration for simplicity reasons since either way the evaluation of the device is based on a 2D simulation in that stage. Velocity inlet boundary conditions are used to define the flow velocity, along with all relevant scalar properties of the flow, at the flow inlet. In this case, the total (or stagnation) pressure is not fixed but will rise (in response to the computed static pressure) to whatever value is necessary to provide the prescribed velocity distribution. Regarding the outlet boundary on the right side of the domain, a pressure outlet boundary condition has been imposed. Pressure outlet boundary conditions require the specification of static (gauge) pressure at the outlet boundary. To set the static pressure at the pressure outlet boundary, the appropriate value for Gauge Pressure in the Pressure Outlet dialog box has been defined. The corresponding dialog boxes for the inlet and outlet conditions are reflected in the Figures below.

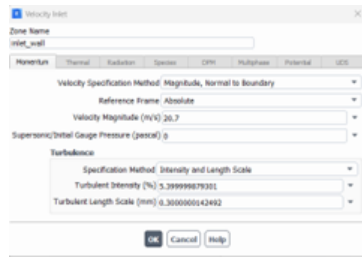


Figure 3.29. Velocity Inlet task page

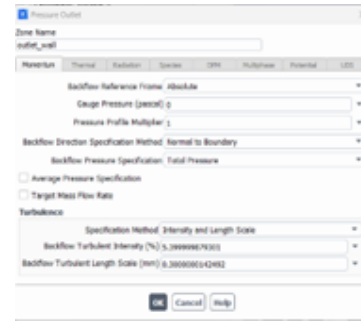


Figure 3.30. Pressure Outlet task page

Additionally to the above boundary conditions, when the flow enters the domain at an inlet, outlet, or far-field boundary, the software requires the specification of transported turbulence quantities. In our case, these quantities are the Turbulence Intensity and the Turbulence Length scale. The chosen values of these quantities are described in Section 3.4. More specifically, turbulence intensity, I , is defined as the ratio of the root-mean-square of the velocity fluctuations, u' , to the mean flow velocity u_{avg} . For internal flows, the turbulence intensity at the inlets is dependent on the upstream history of the flow. The turbulence intensity at the core of a fully-developed duct flow can be estimated from the following formula derived from an empirical correlation for pipe or duct flows:

$$I \equiv \frac{u'}{u_{avg}} = 0.16 (\text{Re}_{D_H})^{-1/8}$$

Furthermore, the turbulence length scale, l , is a physical quantity related to the size of the large eddies that contain the energy in turbulent flows. In fully-developed duct flows, l is restricted by the size of the duct, since the turbulent eddies cannot be larger than the duct. An approximate relationship between l and the physical size of the duct is $l = 0.07D$ where D is the relevant dimension of the duct which is the bluff body's width in our case. If the turbulence derives its characteristic length from an obstacle in the flow, such as bluff bodies, it is more appropriate to base the turbulence length scale on the characteristic length of the obstacle rather than on the duct size according to [7]. Finally, the below dialog box indicates the stationary wall settings.

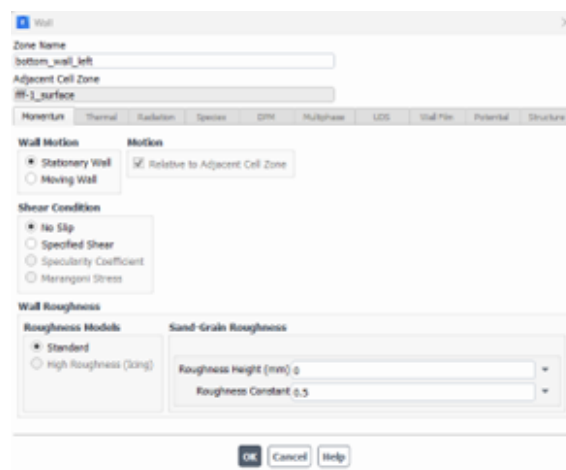


Figure 3.31. Computational domain walls definition

Further to the completion of the setup node with the definition of the viscous model – turbulence model, materials, and boundary conditions, the next step is the appropriate creation of

solutions reports by creating the discrete points as reflected in Figure 3.9 in the "upper-wall-mid" of the created geometry. In this investigation, the variable of interest is the static pressure evolution in the flexible diagram which is modeled here as a rigid wall as stated in Section 3.5. In order to monitor the pressure evolution twenty-one discrete points were created by using the surface report option of ANSYS Fluent. The Area-Weighted Average was selected as the report type for all twenty-one points, and the same report was used to monitor the pressure evolution at the inlet boundary. For the outlet boundary, the pressure was set to 0 Pa in the pressure outlet condition as already said. The twenty-one points where the pressure evolution is monitored are presented in Figure 3.32. It is worth mentioning that the area-weighted average of a quantity is computed by dividing the summation of the product of the selected field variable i.e pressure field and facet area by the total area of the surface.

$$\frac{1}{A} \int \phi dA = \frac{1}{A} \sum_{i=1}^n \phi_i |A_i|$$

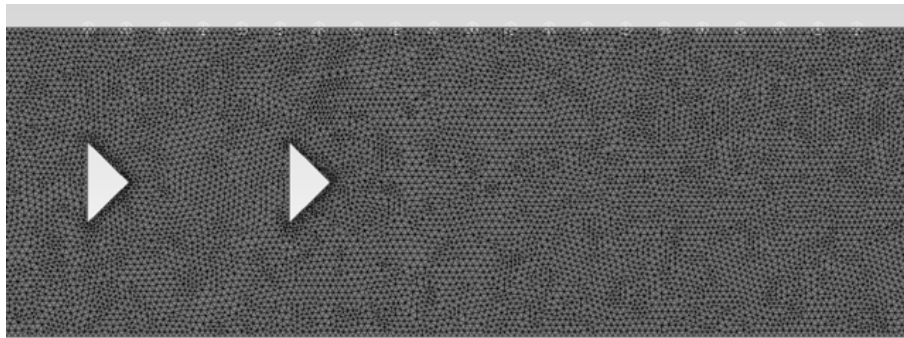


Figure 3.32. Pressure evolution monitoring points

The monitoring and acquisition of the evolution of the pressure field in time at each point is achieved at each time step starting from the first iteration. Subsequently, twenty-one report files are created containing information about the flow time the physical time, and the pressure evolution, one report for each point. The resulting report is in .txt format and the post-processing evaluation of the various signals is based on these .txt files. More details about the post-processing procedure will be given in the following chapters.

Before starting the solver we have to provide ANSYS Fluent with an initial guess for the solution flow field. This process is called "initialization of the solution", and the available methods of entire flow field initialization are listed below.

- Standard initialization
- FMG initialization
- Hybrid initialization

For our research, the last method was implemented i.e. hybrid initialization, and a short description of this method is given below.

Hybrid Initialization is a collection of recipes and boundary interpolation methods. It solves the Laplace equation to produce a velocity field that conforms to complex domain geometries, and a pressure field that smoothly connects high and low-pressure values in the computational domain. All other variables, such as temperature, turbulence, species fractions, volume fractions, and so on, will be automatically patched based on domain averaged values or a particular interpolation

recipe. The default parameters of hybrid initialization were used. The solution initialization task page for hybrid initialization is depicted in the Figure below.

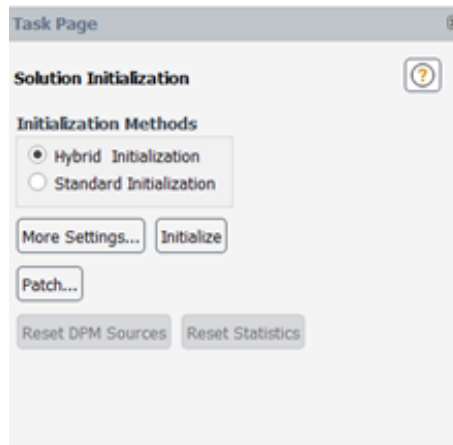


Figure 3.33. Hybrid Initialization of flow field flow

At this stage, the computational model is almost ready to start the iterative process of determining the flow fields required for the evaluation of pressure fluctuation occurring on the device under investigation. The last step is the setup of the time stepping method, the corresponding time step, and the number of time steps for this transient type of simulation. The above values are defined on the run calculation task page. ANSYS Fluent can solve the conservation equations in a time-dependent manner, to simulate a wide variety of time-dependent phenomena, such as vortex shedding and other time-periodic phenomena. As discussed in Section 3.2, the transient solution of the governing equations was sought by means of a first-order Euler scheme in time with a constant physical time step. The solution parameters for the implicit transient formulations are as follows:

- **Max Iterations/Time Step:** When ANSYS Fluent solves the time-dependent equations using the implicit formulation, multiple iterations may be necessary at each time step. This parameter sets a maximum for the number of iterations per time step. If the convergence criteria are met before this number of iterations is performed, the solution will advance to the next time step. [7]
- **The time step size:** is the magnitude of Δt . Since the ANSYS Fluent formulation is fully implicit, there is no stability criterion that must be met in determining Δt . However, to model transient phenomena properly, it is necessary to set at least one order of magnitude smaller than the smallest time constant in the system being modeled. A good way to judge the choice is to observe the number of iterations ANSYS Fluent needs to converge at each time step. For time-periodic calculations, the time step is chosen based on the time scale of the periodicity. For vortex shedding, 20 steps per period have been implemented. The time step Δt for our case was set as described in Section 3.8.
- **Time Stepping Method:** The fixed time step method has been selected for this kind of simulations. That means that the time remains constant during the solution process.

In conclusion, in the frame of the present work several setups and model configurations have been created. The main philosophy of these setups is based on the above-described procedure. After the creation of Fluent models, the simulations were run and the assessment of the results are presented in Chapters 4 to 6.

3.10 Post processing of the simulations

3.10.1 Fundamental frequency and Strouhal number estimation

Besides the pressure evolution and the pressure magnitude that occurs in the device, the vortex shedding frequency and the Strouhal number are also very important quantities for the performance evaluation of the device as already stated in previous chapters. It is known, that the Strouhal number varies with Reynold's number, surface roughness, turbulence intensity, etc. Much research has been dedicated to the empirical determination of the dependence of the Strouhal number on these parameters. In this section, results of the relationship between Strouhal and Reynolds numbers will be presented for the cases C1 to C7 for the blockage ratio of the base line case i.e BR=0.270.

Vinlet	14.7	16.7	18.7	20.7	22.7	24.7	26.7
Re Number	4278	4860	5442	6024	6606	7188	7770
Δt (s)	10^{-5}	10^{-5}	10^{-5}	10^{-5}	$9.36 \cdot 10^{-6}$	$8.60 \cdot 10^{-6}$	$7.96 \cdot 10^{-6}$
T(s)	0.0014	0.00123	0.0011	0.001	0.00090804	0.000834514	0.00076404
f(1/s)	714.2857	813.0081	909.0909	1000	1101.273499	1198.302001	1308.82378
D(m)	0.00425						
St Number	0.207	0.207	0.207	0.205	0.206	0.206	0.208

Table 3.4. Foundamental Frequency and Strouhal number results of cases C1-C7 for constant BR=0.270

Table 3.4 presents the results of the various Reynolds numbers' effect on the vortex shedding frequency and the corresponding Strouhal number. It is noted that during these calculations the blockage ratio was taken as BR = 0.270, which corresponds to a bluff body width of D=4.25mm. Regarding the time discretization was kept constant in all runs and the value of time step occurs from the analysis as discussed in Section 3.8. The vortex shedding frequency, period, and Strouhal number were computed utilizing the pressure variation signal output of point P5 where the maximum pressure fluctuation occurred for most cases. The post-processing procedure for calculating these quantities has happened with two different approaches. The first way is the manual calculation of the signal's period. After that, the calculation of frequency and Strouhal number, and the second approach is the direct calculation of the Strouhal number through Fluent Fast Fourier Transform analysis of the same signal. It is obvious that the final results are the same for both approaches. These post-processing procedures will be briefly described below, having as an example the base case run i.e C4 with 20.7 m/s inlet velocity.

Figure 3.34 depicts the output signal of pressure evolution for point P5. The period of the signal is from peak to peak as reflected in the figure. Within the period there are 100 reported values. Taking the advantage of the constant time step, if we multiply the number of the reported values with the time step the period T will result. For this case, i.e C4 is equal to 0.001s. From the period easily we may find the vortex shedding frequency on point P5. Having the vortex shedding frequency we obtain the Strouhal number by using the expression described in Chapter 2, Section 2.4.

$$St = \frac{f \cdot D}{V_{inlet}} = \frac{1000 \cdot 0.00425}{20.7} = \frac{\left[\frac{1}{s}\right] \cdot [m]}{\left[\frac{m}{s}\right]} = 0.205$$

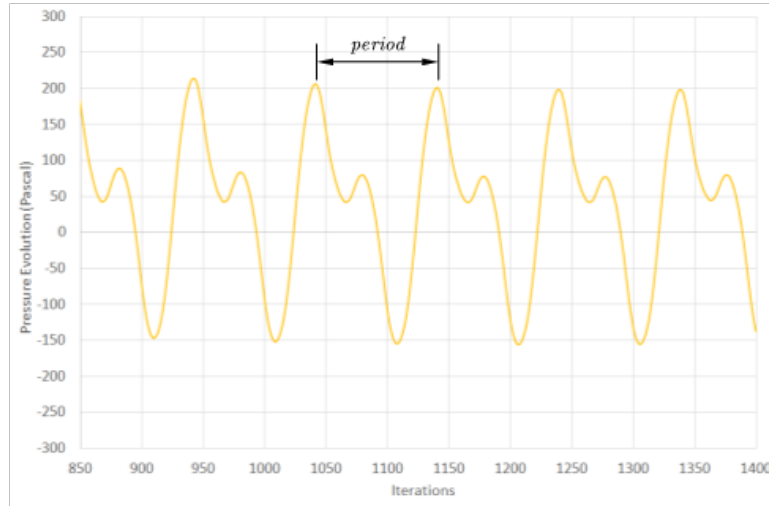


Figure 3.34. Pressure evolution in time for case C4

The same philosophy has been followed for the rest cases.

As mentioned earlier, the fundamental frequency and the Strouhal number can be calculated by using the Fourier transform utility of the ANSYS Fluent. This module enables us to compute the Fourier transform of a signal $\varphi(t)$, a real-valued function, from the number of its sampled points. In particular, in order to find the frequency of the signal we have to translate the signal from the time domain to the frequency domain. For a periodic set of N sampled points, φ_k , the discrete Fourier transform expresses the signal as a finite trigonometric series [7]:

$$\varphi_k = \sum_{n=0}^{N-1} \hat{\varphi}_n e^{2\pi i k n / N} \quad k = 0, 1, 2, \dots (N-1) \quad (3.1)$$

where the series coefficients $\hat{\varphi}_n$ are computed as:

$$\hat{\varphi}_n = \frac{1}{N} \sum_{k=0}^{N-1} \varphi_k e^{2\pi i k n / N} \quad n = 0, 1, 2, \dots (N-1) \quad (3.2)$$

Equation 4.1 and Equation 4.2 form a Fourier transform pair that enables us to determine one from the other. Furthermore, when we follow the convention of varying n from 0 to $N-1$ in Equation 4.1 and Equation 4.2 instead of from $-N/2$ to $N/2$, the range of index $1 \leq n \leq N/2 - 1$ corresponds to positive frequencies, and the range of index $N/2 + 1 \leq n \leq N - 1$ corresponds to negative frequencies. $n = 0$ corresponds to zero frequency. Nevertheless, for the actual calculation of the transforms, ANSYS Fluent adopts the so-called fast Fourier transform (FFT) algorithm, which significantly reduces operation counts in comparison to the direct transform [7].

The required data for the Fourier Transform is the signal variation in time, which in our case is the point P5 pressure evolution as depicted in Figure 3.34. When the .txt file is loaded, we have to modify the input signal to disregard the data before periodicity establishment. The relevant settings are presented in Figure 3.35. The Y-axis of the spectral analysis is the amplitude of the signal and the X-axis is the frequency or Strouhal number. For the detailed spectral representation with all resolved harmonics, the Magnitude (A) is defined for the frequency f_n as:

$$A(f_n) = \begin{cases} |\hat{\varphi}_n| & n = 0, N/2 \\ 2|\hat{\varphi}_n| & n = 1, 2, \dots, N/2 - 1 \end{cases} \quad (3.3)$$

Where $A(f_0)$ is the mean signal value.

There are three options for the X-axis function you can choose from in order to plot or write the detailed spectrum with all resolved Fourier modes. These three options are related to the discrete frequencies at which the Fourier coefficients are computed. For our case, the frequency and the Strouhal are used as mentioned before, where the frequency is defined as:

$$f_n = \frac{1}{N\Delta t}n, n = 0, 1, 2, \dots, N/2 \quad (3.4)$$

where N is the number of data points used in the FFT. The Strouhal number is calculated as described in Chapter 2 Section 2.4.

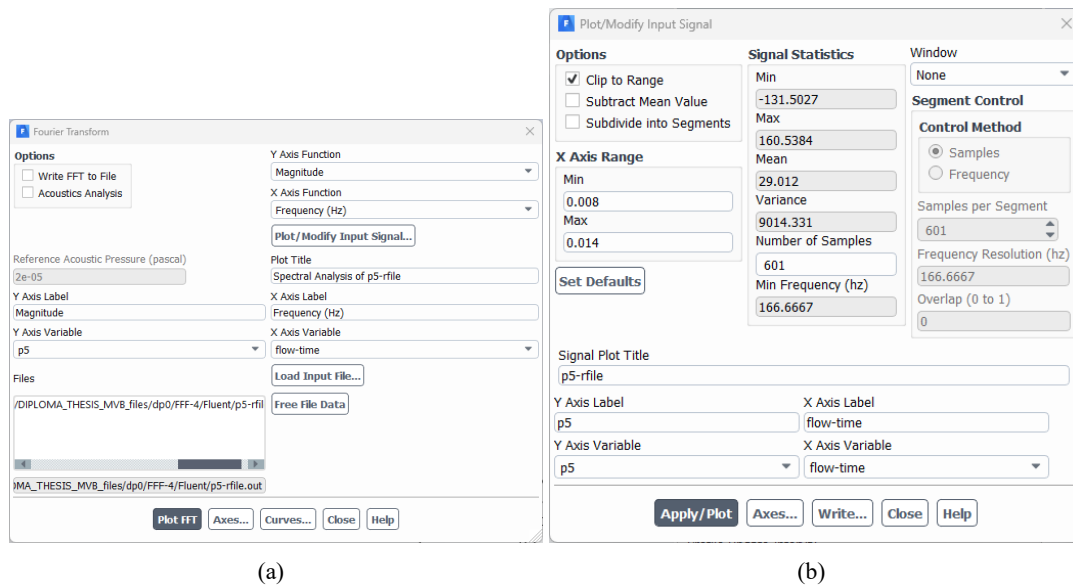


Figure 3.35. FFT set up

The results of spectral analysis of point P5 signal for the baseline case i.e C4 with respect to the fundamental frequency and Strouhal number are shown in the below Figure.

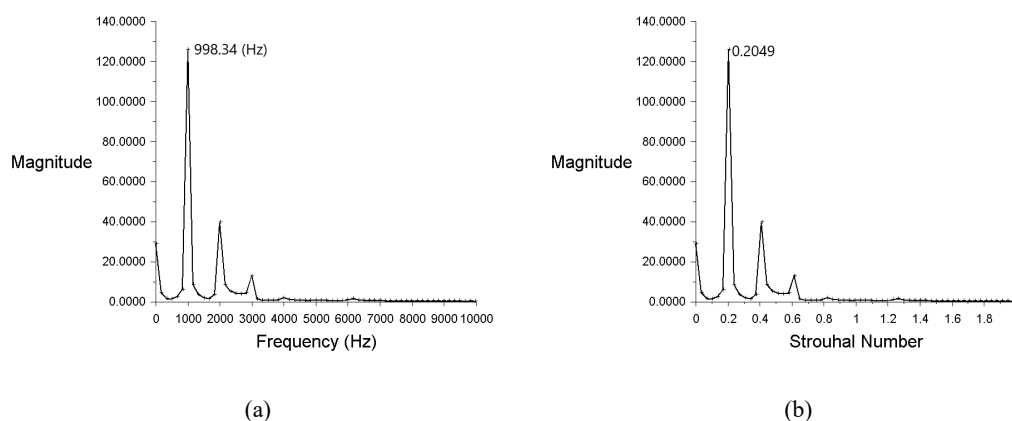


Figure 3.36. Spectral analysis (a) X-axis frequency (b) X-axis Strouhal

The fundamental frequency obtained by the spectral analysis is equal to 998.34 Hz, and the Strouhal number is equal to 0.2049. The other peaks are harmonics as the input signal is not

perfectly sinusoidal. Both values are in good agreement with those presented in Table 3.4. The same approach was followed for the rest cases as well.

Chapter 4

Parametric studies for various Reynolds numbers and Blockage Ratios

In the literature, energy harvesting devices using bluff bodies, similar to the device under examination, are tested employing CFD and experimental simulations with fixed inlet velocity V_{in} and constant BR. The optimum position of the diaphragm along the upper wall at position, where maximum pressure amplitudes occur, in relation to changes in Reynolds number and blockage ratio is examined in this chapter. The inlet velocities chosen for the various values of Re and BR were presented in Table 3.1, in Section 3.3 where the case studies are described.

Following the mesh independence analysis, grid $G_{0.3}$ was chosen as the grid leading to grid independence results. Therefore all cases illustrated in Table 3.1 were simulated using this grid. The presentation of the results is carried out with several contours containing information for quantities of interest such as pressure and velocity fields. Finally, the vortex shedding frequency and the nondimensional Strouhal number were calculated and their variation was compared with respect to the different Reynolds numbers and BR. The different configurations of the computational grid for the various BR are presented in Figure 4.1

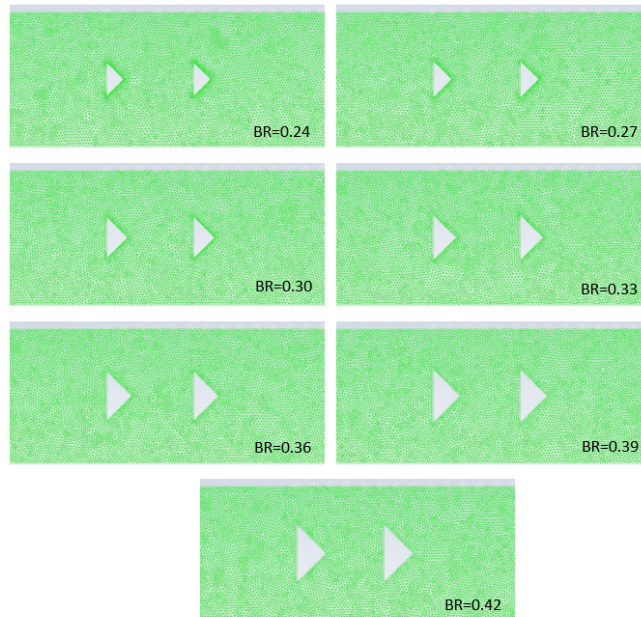


Figure 4.1. Generated grids for various values of BR

After performing the numerical simulations for the 49 different cases (corresponding to 7 Re and 7 BR values), as they described in Table 3.1 (subsection 3.3.1), generating grids and selecting time-steps according to what presented in sections 3.7 and 3.8, respectively and carrying out appropriate post-processing, the obtained results are presented herein. First, the effect of Reynolds is presented for various values of blockage ratio. Then, the corresponding information in the form of the effect of BR for various Reynolds numbers is presented.

4.1 Effect of Reynolds numbers for various blockage ratios

The seven cases C1-C7, corresponding to different inlet Reynolds numbers, were simulated in grids like $G_{0,3}$, for each of the seven different BR values. The results are presented in this section with BR as a parameter.

Some representative pictures of the flow-field are presented first, for the sake of demonstration. These concern the baseline geometry with blockage ratio $BR = 0.27$. In particular, Figure 4.2 depicts representative results of iso-velocity contours predicted at time 14ms for the cases C1 to C7, where $V_{in} = 14.7$ to 26.7m/s ($Re = 4278$ to 7770). Obviously, a greater maximum value of velocity is attained for case C7 due to the greater inlet velocity, in the region above and below the bluff bodies (red regions in figures), where flow is accelerated due to the narrow flow passage.

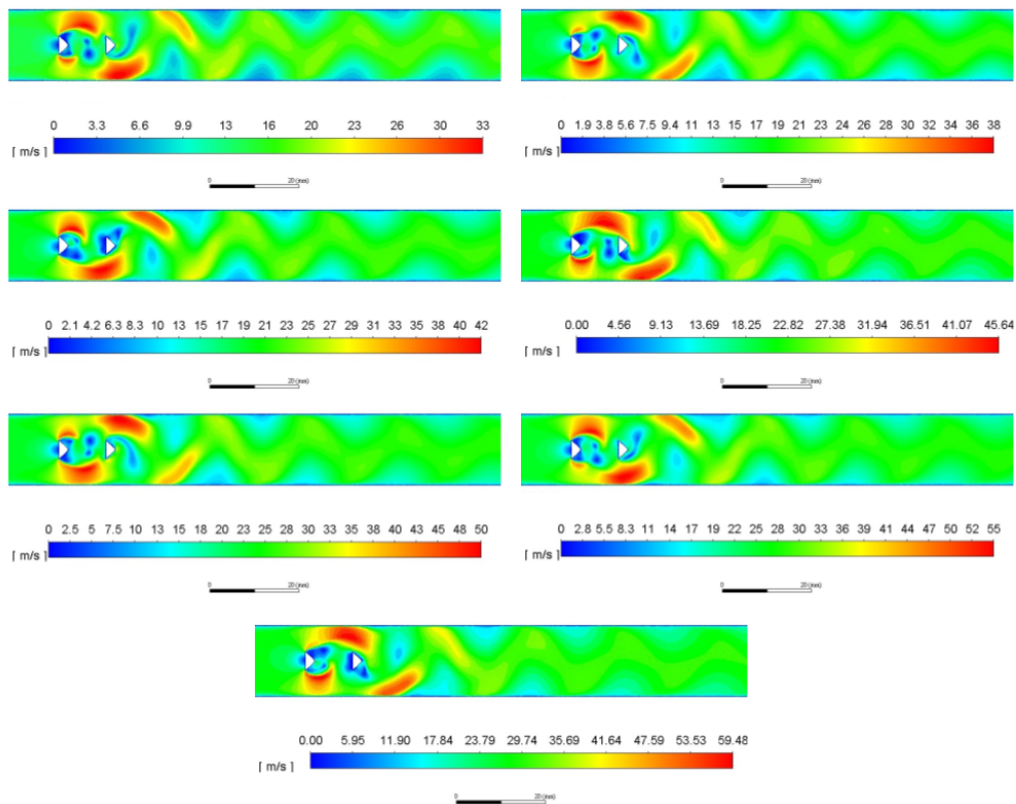


Figure 4.2. Iso-velocity contours predicted at 14ms in the baseline geometry ($BR=0.27$) for cases C1 to C7.

In Figures 4.3, 4.4 the pressure amplitude variation, along the flexible diaphragm is presented for $BR=0.270$ and $BR=0.330$. As it can be observed, an increase in the Reynolds numbers or V_{in} leads to an increase in pressure amplitude variation (pressure fluctuation) along the length of the flexible diaphragm for the aforementioned BR, at least for the Reynolds numbers investigated in the present work. Additionally, it is worth mentioning that the plots of pressure fluctuation along the diaphragm for each Reynolds number and BR are quite similar among each other.

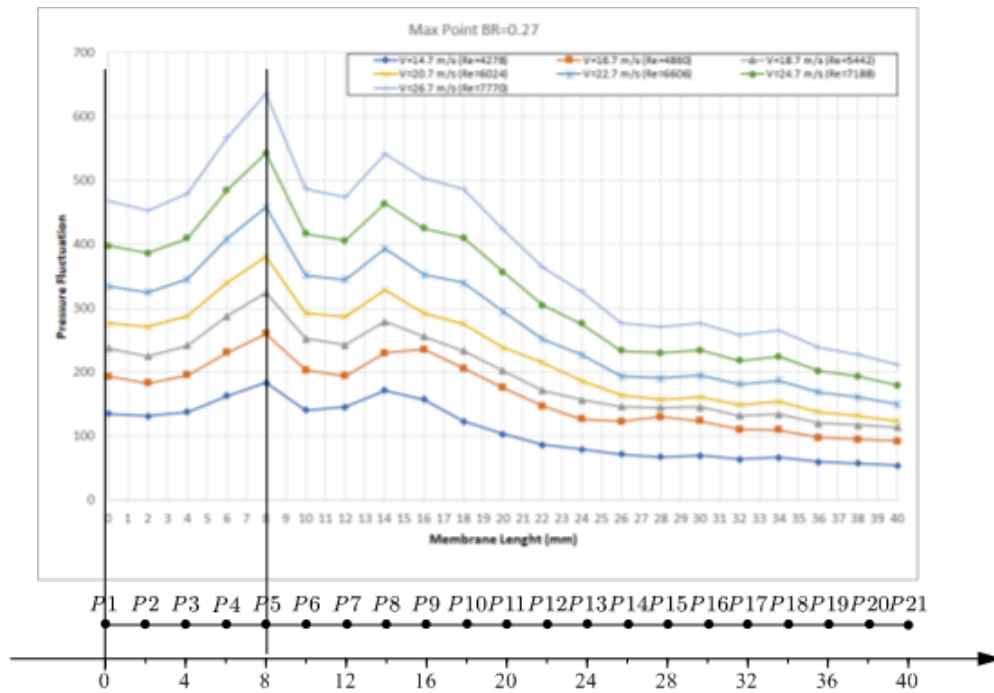


Figure 4.3. Pressure fluctuation amplitude versus distance from the beginning of the diaphragm for BR=0.270

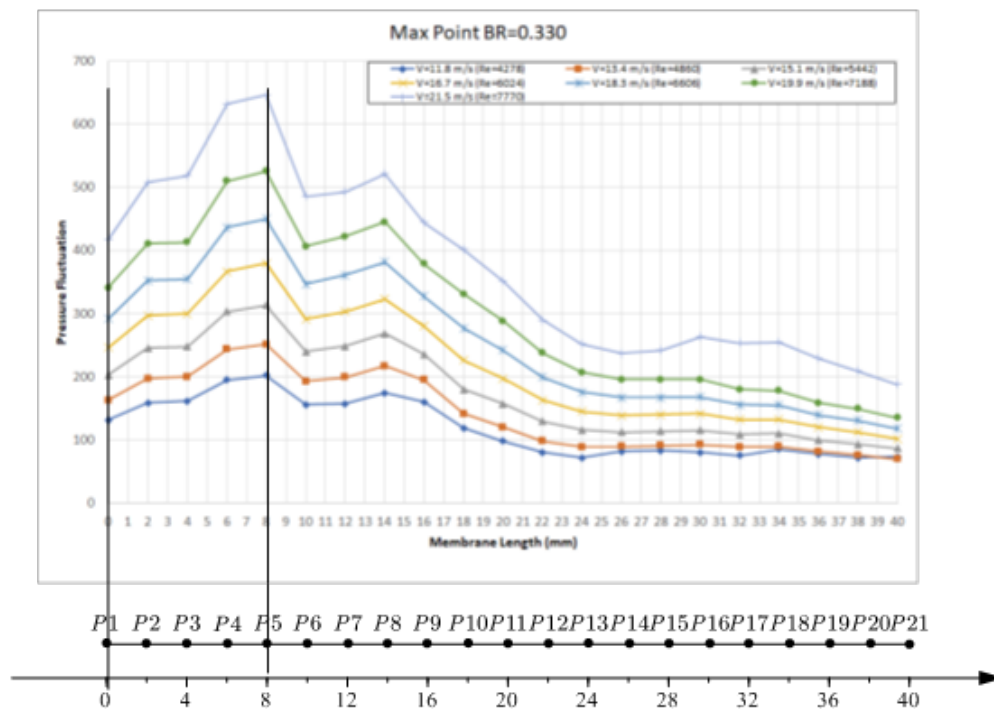


Figure 4.4. Pressure fluctuation amplitude versus distance from the beginning of the diaphragm for BR=0.330

Furthermore, Figures 4.3, 4.4 illustrate the position, where the maximum pressure fluctuation along the diaphragm is predicted. According to these figures, this position was found for all cases

C1-C7 at distance $8\text{mm}=1.88D$ from the beginning of the diaphragm, i.e. at point P5. It has to be noticed, that similar plots like that of Figures 4.3, 4.4 were derived for the rest blockage ratio and the results were the same, regarding the maximum pressure fluctuation point. This result is very important in designing such a miniature energy harvesting device, indicating that the position of the flexible diaphragm position along the upper wall is a key factor for the performance of the device.

Apart from the pressure fluctuation, changing the inlet velocity is expected to influence also the pressure drop in the flow channel. This is calculated as $P_{in} - P_{out}$, where P_{in} is the pressure at the inlet and P_{out} is the pressure at the outlet, in our study imposed to be 0 Pa.

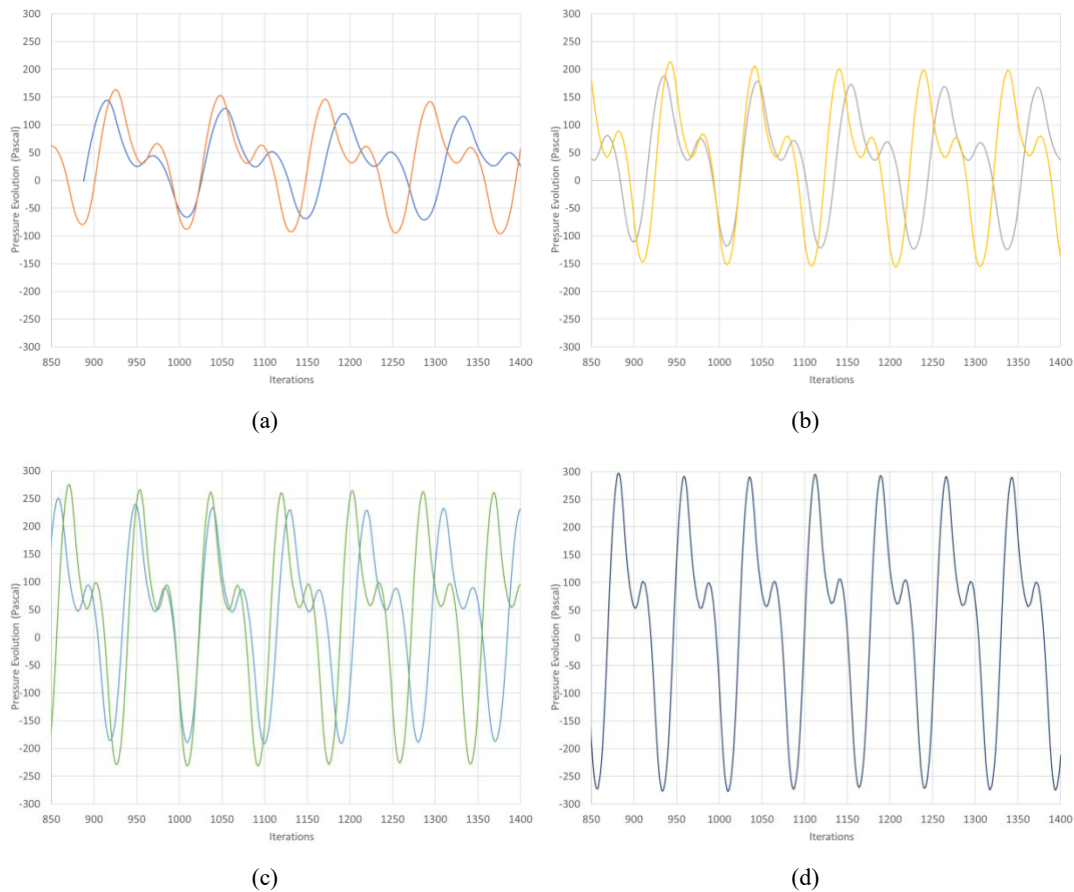


Figure 4.5. Comparative pressure evolution at P5 for cases (a) C1-C2 (b) C3-C4 (c) C5-C6 (d) C7

Figure 4.5 depicts pressure evolution at point P5 on the membrane in plots, each containing one or two curves. In particular Figure 4.5 (a) presents cases C1-C2 and similarly 4.5(b) C3-C4, 4.5(c) C5-C6 and 4.5(d) C7. Pressure range (on the vertical axis) is the same in all of these plots, i.e. -300 to 300 Pa. The X-axis depicts the iterations after the phenomenon periodicity establishment and this range is from 850 to 1400. As it can be observed, pressure signal varies with the flow Reynolds number both in amplitude and fundamental frequency (actually determining the period of the phenomenon). The effects of Reynolds and BR on the two aforementioned quantities are presented in what follows.

Figure 4.6 presents the variation of maximum pressure amplitude at point P5 with respect to the increase of inlet velocity for the various values of BR. An almost linear increase of the amplitude with inlet velocity is noticed for all BR. Furthermore the inclination of the curves increases slightly as BR increases. For the same inlet velocity, pressure amplitude increases with the increase of BR.

The curves in the plot, are shifted to the left as BR increases, i.e. towards lower values of velocity. This is due to the fact that the same range of Reynolds numbers was decided to be simulated for each BR, so the inlet velocity was computed according to the formula $V_{in} = (\mu \cdot Re) / (\rho \cdot BR \cdot H)$ (see section 3.3.1), according to which, for the same Re, as BR increases V_{in} decreases.

Figure 4.7 presents the same information in terms of corresponding non-dimensional quantities, namely coefficient of maximum pressure amplitude against Reynolds number, where the pressure coefficient was defined as $Cp_{max} = \Delta p_{max} / (0.5 \cdot \rho \cdot V_{in}^2)$. According to this plot, Cp_{max} seems to have an almost constant value irrespective Re for the same BR. This means that the effect of Re on Cp is very weak and Cp is actually an increasing function of BR.

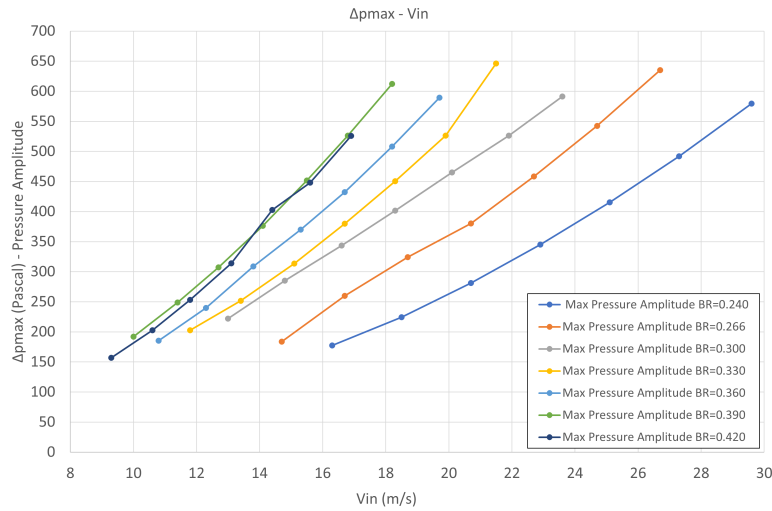


Figure 4.6. Variation of pressure amplitude with respect to inlet velocity

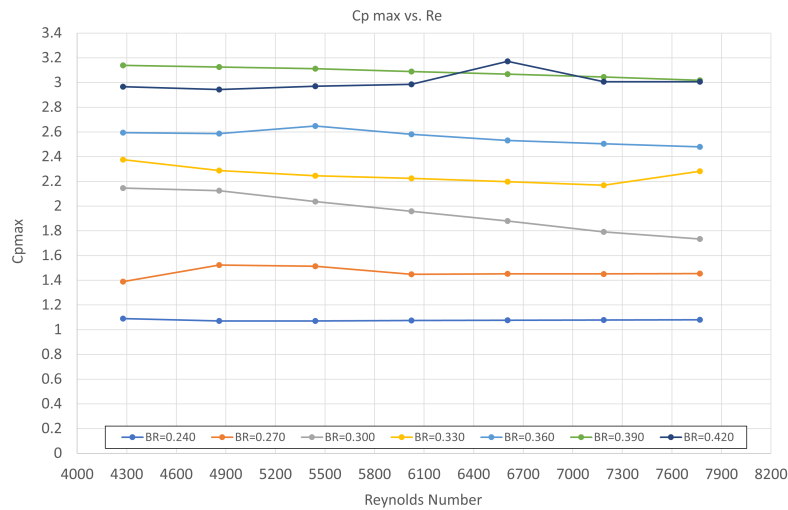


Figure 4.7. Non-dimensional pressure amplitude coefficient with respect to Reynolds number.

Figure 4.8 shows the variation of the fundamental frequency of the predicted pressure signal at point P5 with respect to inlet velocity for the various BR values. An almost linear variation is predicted for all the values of BR and the curves have all about the same inclination. For the same inlet velocity, frequency decreases with the increase of BR. Figure 4.9 presents the same information in terms of corresponding non-dimensional quantities, namely Strouhal number against Reynolds

number. According to this plot, the value of St for each BR is almost constant (independent of Re) and also increases with the increase of BR.

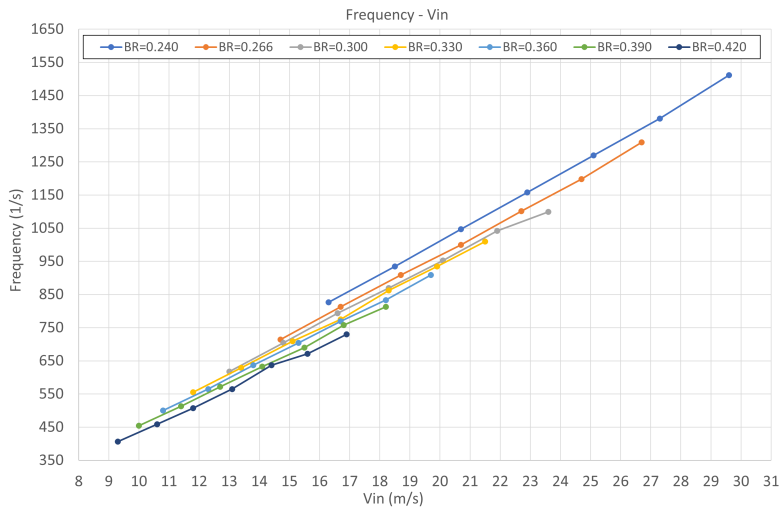


Figure 4.8. Variation of frequency with respect to inlet velocity

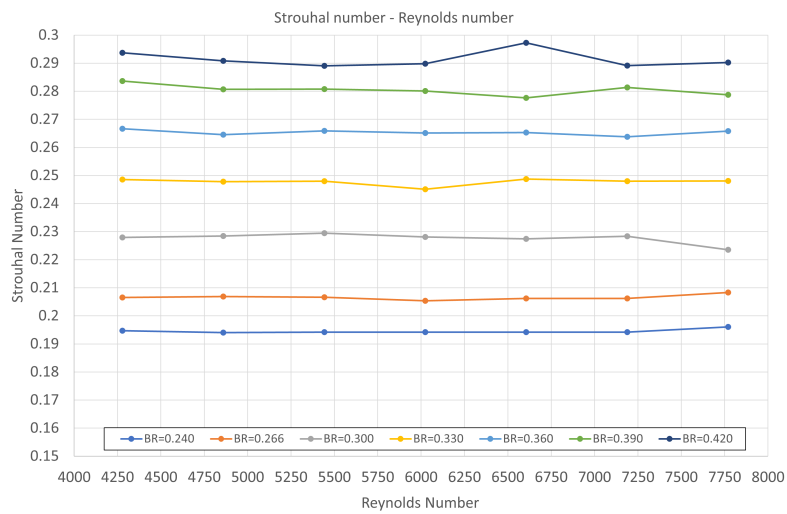


Figure 4.9. Variation of non-dimensional frequency (Strouhal) with respect to Reynolds number

Figure 4.10 presents the variation of average pressure drop in the channel with the increase of inlet velocity for various BR. As expected, pressure drop changes with the square of velocity for all values of BR. For the same inlet velocity, pressure drop increases with BR. Figure 4.11 presents the same information in terms of non-dimensional average pressure drop coefficient ($C_{p,drop} = \Delta p_{drop} / (0.5 \cdot \rho \cdot V_{in}^2)$) against Re . According to it, $C_{p,drop}$ is almost constant for each Re , having a different value for each BR.

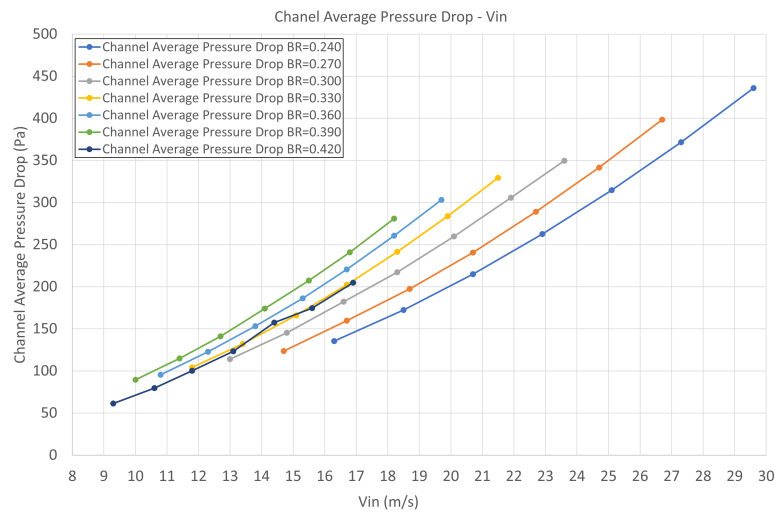


Figure 4.10. Variation of average pressure drop with respect to inlet velocity

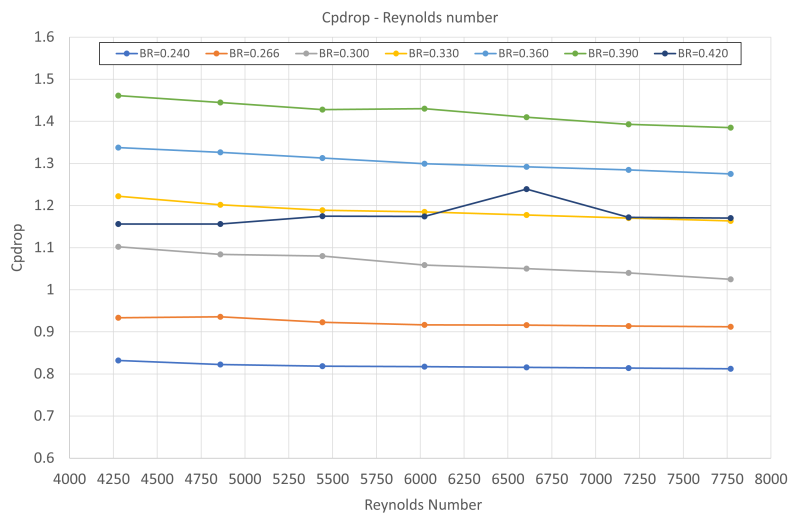


Figure 4.11. Variation of non-dimensional average pressure drop with respect to Reynolds number

4.2 Effect of blockage ratio for various Reynolds numbers

The results of the previous subsection, obtained for various Reynolds numbers and blockage ratios, are now presented against BR with Re as a parameter.

Figure 4.12 depicts maximum pressure amplitude (i.e. amplitude at point P5) with the increase of BR for various values of Re (and corresponding V_{in}). According to it, for each Re, the amplitude exhibits only a small variation with BR. For the same BR, the amplitude increases with the increase of Re. Figure 4.13 presents the pressure amplitude coefficient $C_{p,max}$ against BR. This exhibits an almost linear increase with BR irrespective of the Reynolds.

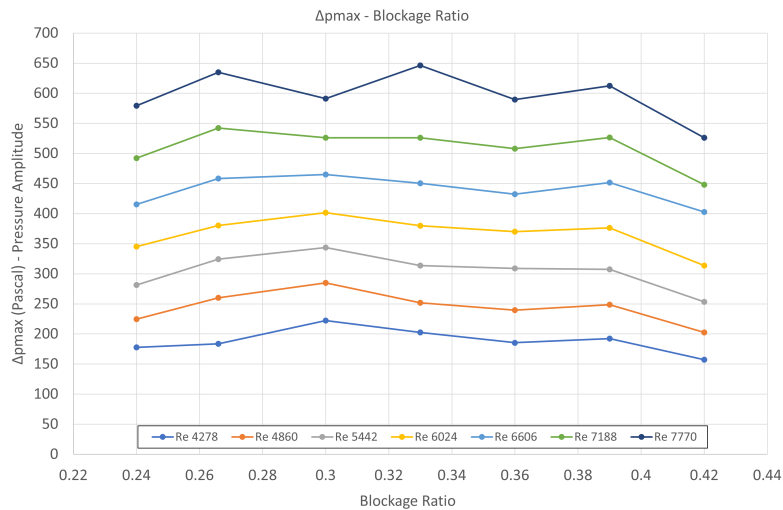


Figure 4.12. Variation of pressure amplitude with BR for various Re numbers.

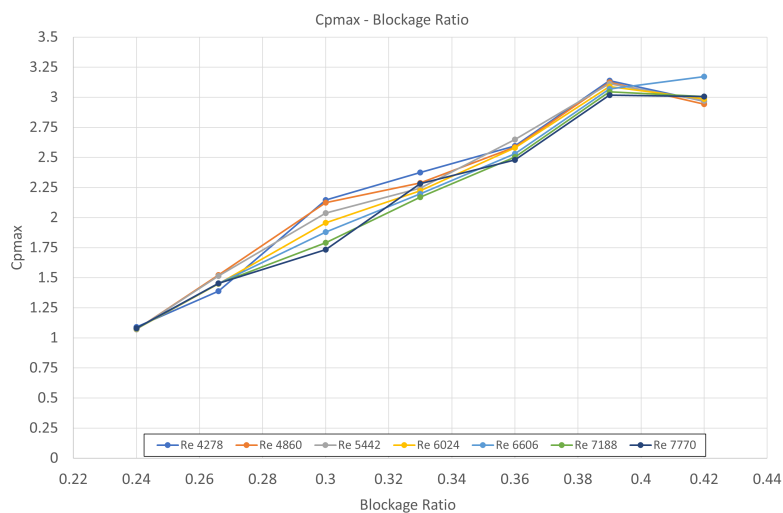


Figure 4.13. Variation of pressure amplitude coefficient with BR for various Re numbers.

Figure 4.14 presents the fundamental frequency of the pressure signal at point P5 with BR for various Re values. This quantity decreases with the increase of BR at constant Re. For the same BR, higher Re corresponds to higher frequency. Figure 4.15 shows the Strouhal number against BR for various Re. Finally Strouhal is almost independent of Re and increases about linearly with BR.

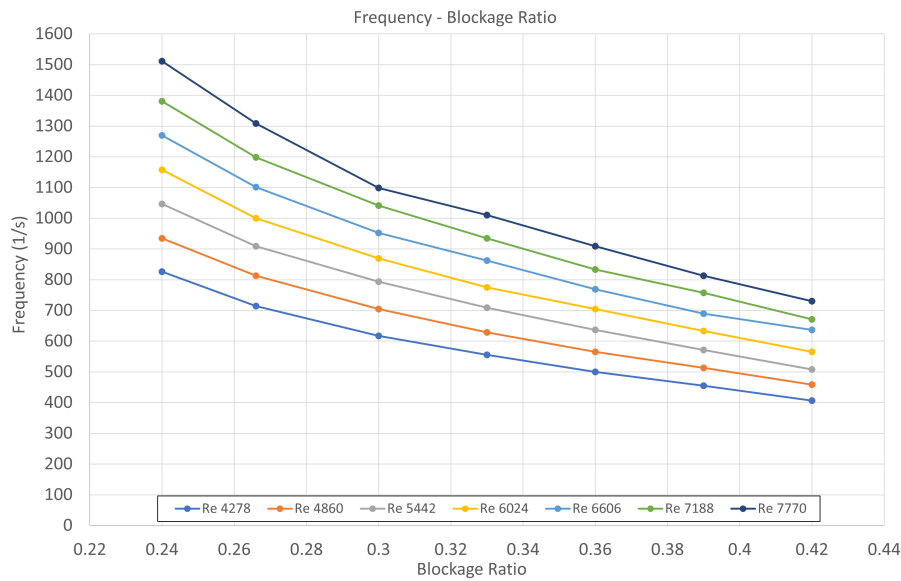


Figure 4.14. Variation of frequency with BR for various Re numbers.

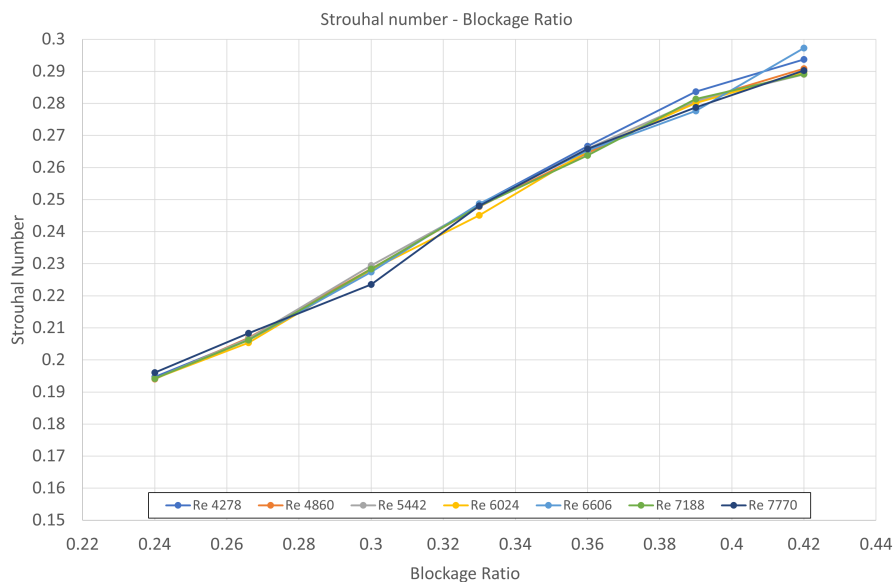


Figure 4.15. Variation of Strouhal number with BR for various Re numbers.

Figure 4.16 shows the change of the average pressure drop with BR for various Re. As expected, for constant BR, pressure drop increases with the increase of Re. However, pressure drop decreases with the increase of BR for constant Re. Although this seems contradictory to what is expected, it can be explained as follows: in order to keep constant Re while BR (and d) increases, lower values of V_{in} have been used. This means that although the flow path in the channel becomes narrower, the velocity of the flow through it is lower. Since pressure drop varies with the square of velocity, the latter dominates from a quantitative point of view and finally, pressure drop becomes lower. Of course, if BR was increased without changing inlet velocity, the pressure drop would increase. Figure 4.17 presents the pressure drop coefficient against BR for various Re. Like St before, it is almost independent of the Reynolds and increases about linearly with BR, except of the final value.

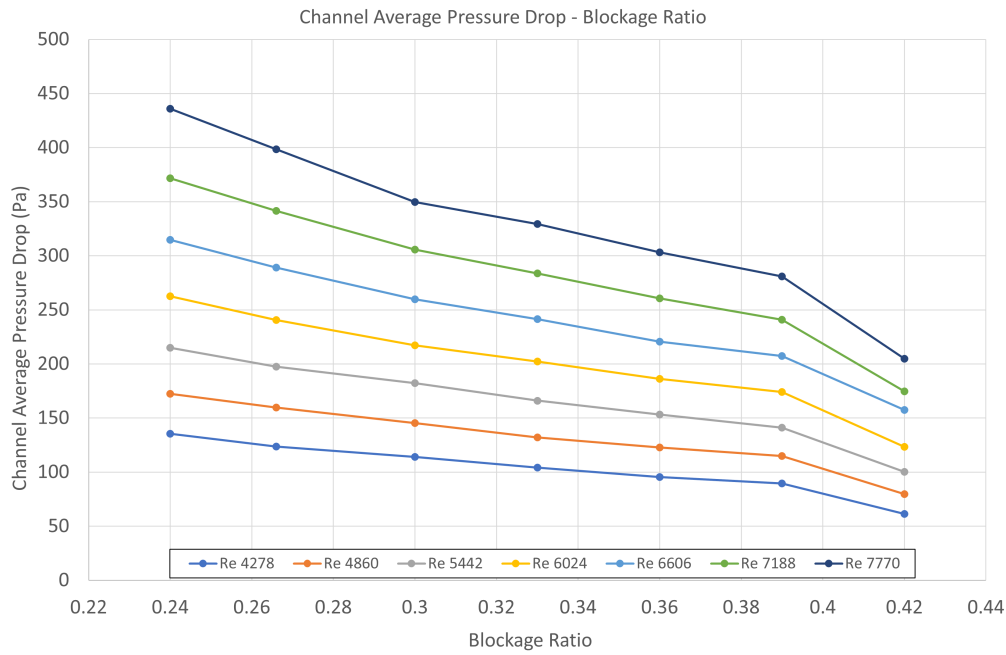


Figure 4.16. Variation of average pressure drop with BR for various Re numbers.

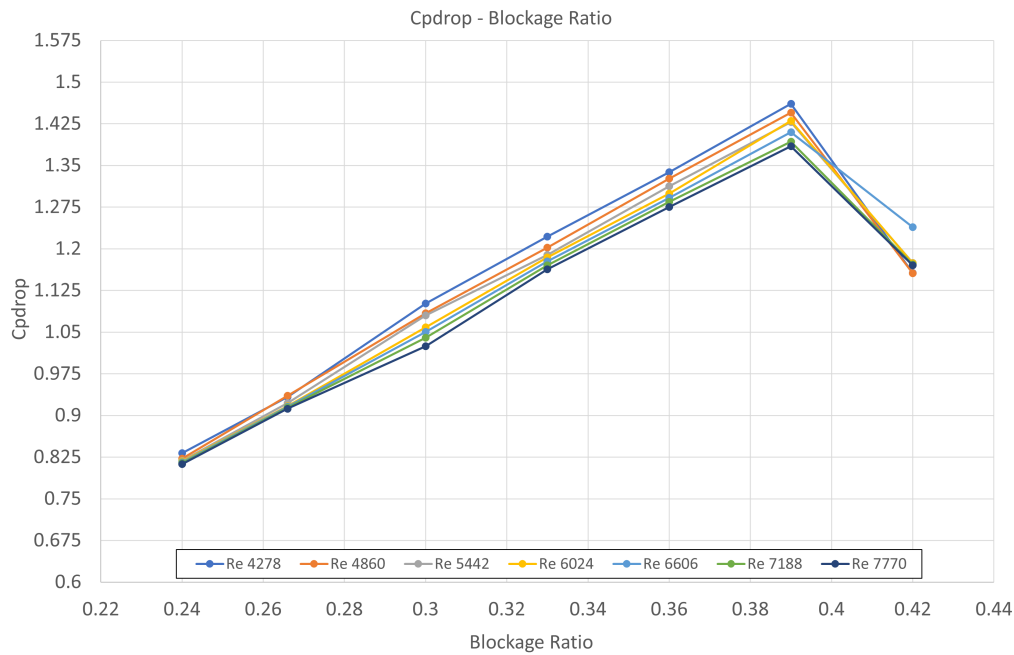


Figure 4.17. Variation of average pressure drop coefficient with BR for various Re numbers.

In order to depict the effect of both Reynolds and blockage ratio on maximum pressure amplitude and frequency, the corresponding surface plots of these quantities, i.e. $\Delta p_{\max} = F1(BR, Re)$ and $f = F2(BR, Re)$ as they were extracted by the simulations are presented in Figures 4.18 and 4.19, respectively. According to them, the maximum pressure amplitude is high for high Re values, at any BR, while the frequency of pressure signal exhibiting the maximum amplitude (i.e. at point P5) is maximized for low values of BR and high values of Re. As a consequence, if high amplitude combined with high frequency is desired, low BR with high Re should be used. However, it has

to be noticed that the above statements refer to a specific operational Reynolds range.

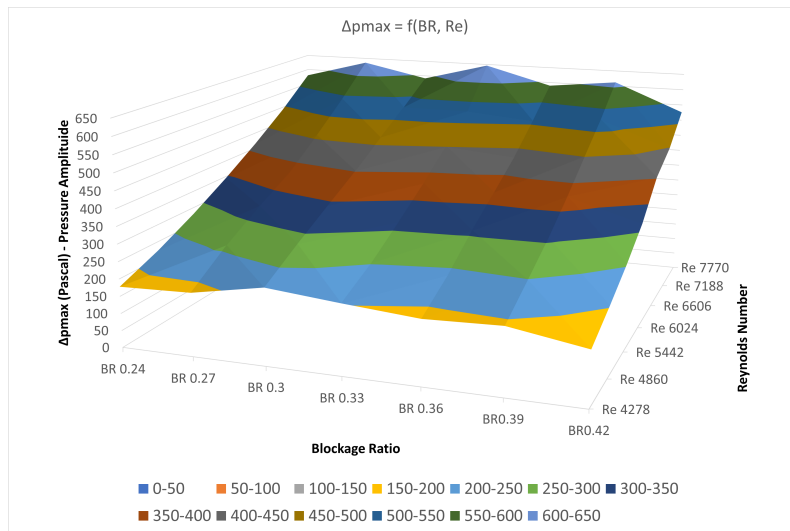


Figure 4.18. Surface plot of amplitude of the pressure signal at point P5, where maximum pressure amplitude occurs, as a function of BR and Re.

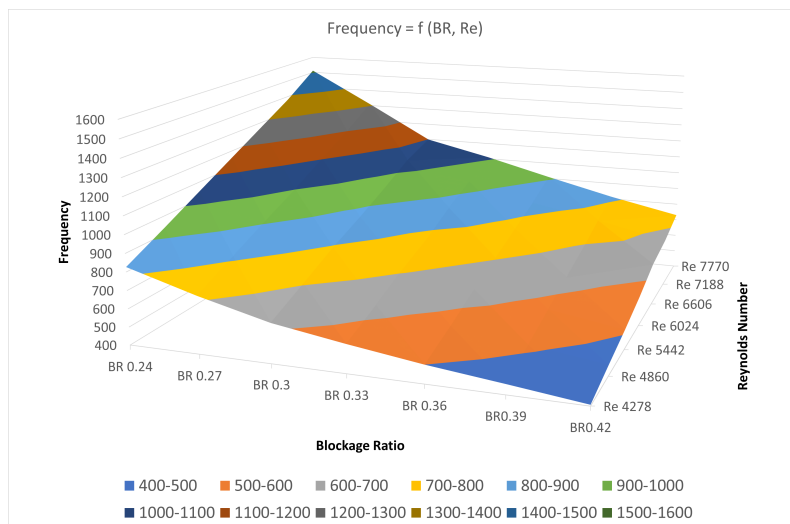


Figure 4.19. Surface plot of frequency of the pressure signal at point P5, where maximum pressure amplitude occurs, as a function of BR and Re.

Chapter 5

Investigation of vortex shedding suppression due to blockage ratio increase

Nguyen et al [26] investigated the effect of blockage ratio increase on the performance of the device under consideration by means of numerical simulations. To this end, they predicted numerically the mean value and amplitude of the pressure signal at the center S (see Figure 5.1) of the diaphragm for higher values of BR. They concluded that by increasing BR, the performance is enhanced, attaining a maximum for BR=0.330 and then gradually decreases and becomes zero for BR=0.420, where vortex shedding suppression takes place. Figure 5.2 presents their plot from [26], concerning the change in mean value and amplitude of pressure at the center of the diaphragm with BR increase, that schematically shows the above-described behavior.

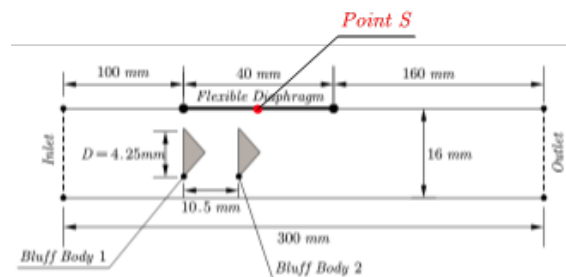


Figure 5.1. Definition of S point (center of the diaphragm)

However, in the present study, the above claim of the authors in [26] was not validated. Not only vortex shedding was predicted by the present approach at BR=0.420 and beyond, but pressure amplitude at S continued to increase in this range of BR values. These findings motivated to conduct a more extended study in order to find the value of BR for which vortex shedding suppression is predicted by the present CFD model. To this end, the inlet velocity was kept constant $V_{in} = 20.7 m/s$, the blockage ratio was gradually increased according to what is described in Table 5.1 and the corresponding case was simulated and the results were post-processed, up to numerically predict suppression of vortex shedding. In particular, after having predicted vortex shedding for BR=0.420, higher values of BR were tested, namely the value of BR=0.550. For that value, vortex shedding not only was not suppressed, but an important enhancement of its amplitude was predicted compared to the BR=0.420 case. This led to several numerical simulations and related trial-and-error efforts, in order to actually find the value of BR for which vortex shedding is suppressed. This value was finally found to be BR=0.662, i.e. significantly higher than that predicted in [26].

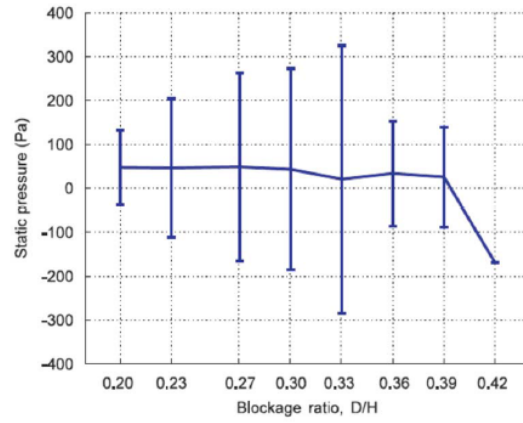


Figure 5.2. Change in mean value and amplitude of pressure at the center of the diaphragm with BR increase from [26].

		Vin = 20.7 m/s													
BR	0.24	0.27	0.33	0.33	0.36	0.39	0.42	0.55	0.65	0.655	0.66	0.661	0.662	0.663	
Re	5443	6024	6804	7484	8164	8845	9525	12473	14741	14854	14968	14991	15013	15025	

Table 5.1. BR and Reynolds numbers with constant $V_{in} = 20.7\text{m/s}$

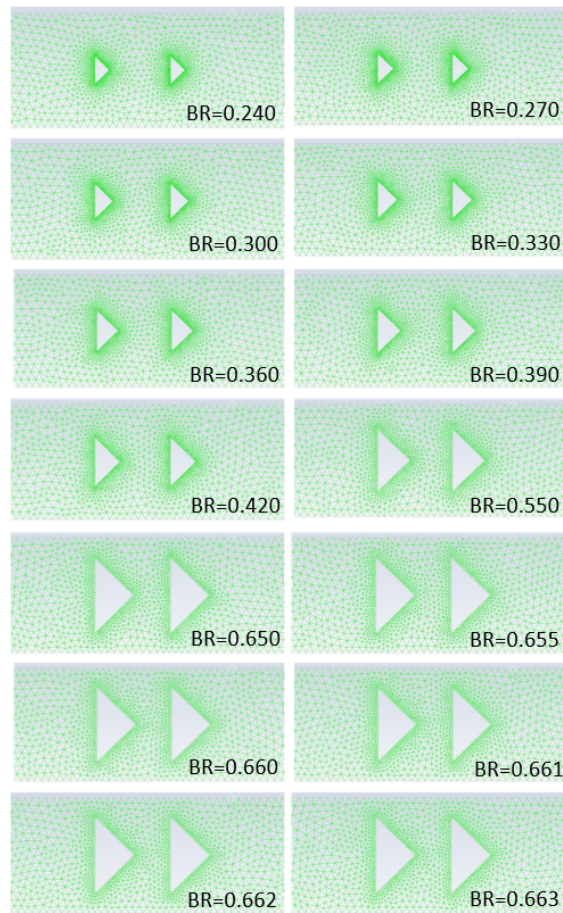


Figure 5.3. Generated grids for vortex shedding suppression study

The grids generated for these cases are shown in Figure 5.3. It is important to note that a grid size of $G_{1,0}$ was used for all cases, as opposed to $G_{0,3}$ which was used in studies of the previous chapter. This was done in order to ensure that the results will be consistent and comparable to those illustrated in Figure 5.2. It is also noted that the time step selection for this investigation was based on what is discussed in Section 3.8.

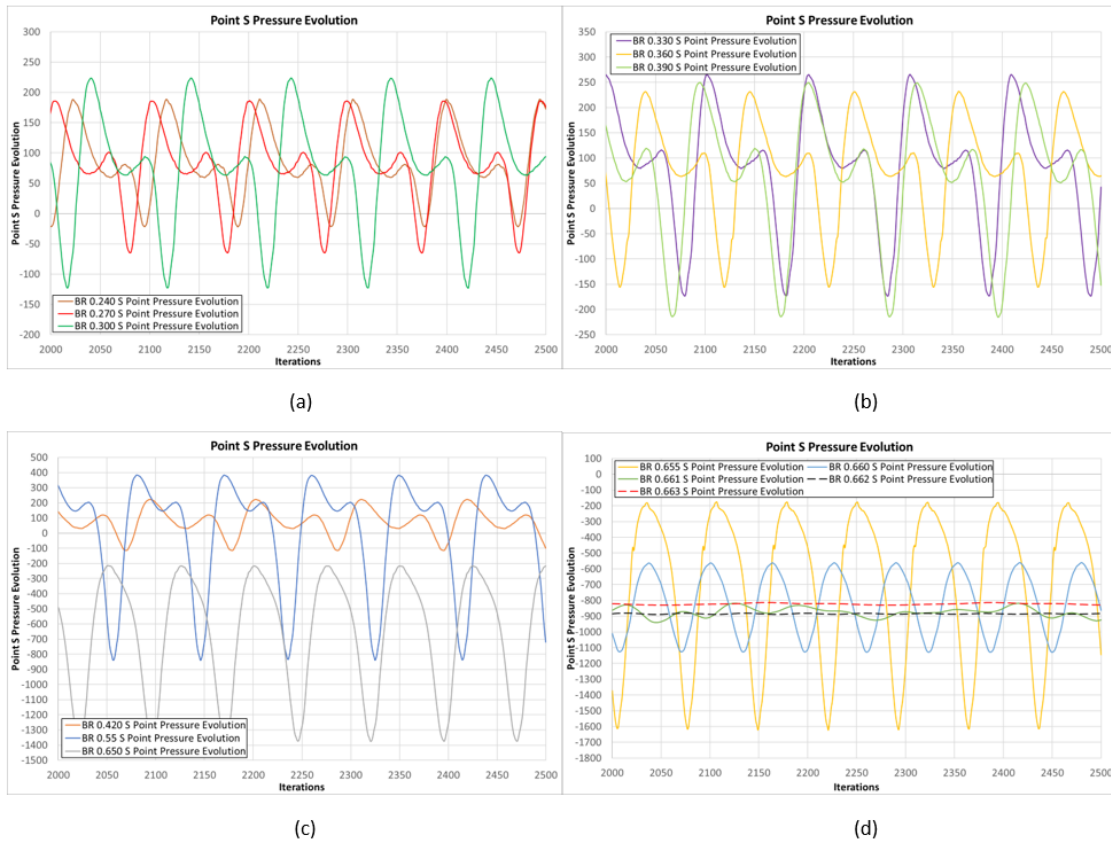


Figure 5.4. (a) BR 0.240 - BR 0.300 S Point Pressure Evolution, (b) BR 0.330 - BR 0.390 S Point Pressure Evolution (c) BR 0.420 - BR 0.650 S Point Pressure Evolution, (d) BR 0.655 - BR 0.663 S Point Pressure Evolution

In Figure 5.4, the pressure changes over time after the establishment of periodicity are shown for different blockage ratios ranging from 0.240 to 0.663. Each subfigure, (a)-(d), includes three pressure evolution curves for different blockage ratios. The frequency and Strouhal number for each signal were calculated using the methods described in Section 3.10. As we can observe from Figure 5.4 (d), the pressure changes (signal amplitude) are minimal for a blockage ratio of around $BR = 0.662$, indicating that vortex shedding suppression has occurred in the channel.

Figure 5.5 (a) – (c) depicts the results of the iso-velocity field at 25ms. Specifically, Figure 5.5 (a) shows the velocity field using a BR value of 0.420, Figure 5.5 (b) displays the velocity field using a BR value of 0.550, and Figure 5.5 (c) illustrates the velocity field using a BR value of 0.662 where vortex shedding suppression was observed. It can be seen in Figure 5.5 (c) that there is no vortex shedding present past the bluff bodies, which agrees with the results shown in Figure 5.4 (d) which shows the pressure evolution over time for a BR value of 0.662.

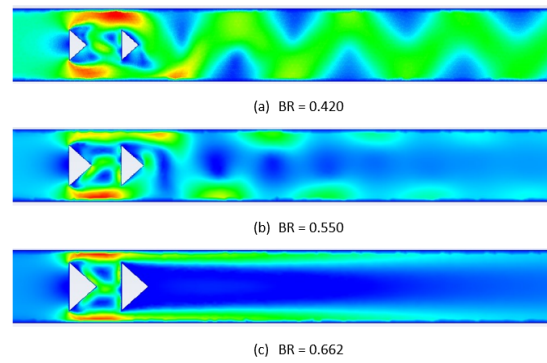


Figure 5.5. Iso-velocity field on 25ms. (a) BR=0.420, (b) BR=0.550, (c) BR=0.662. $V_{in} = 20.7m/s$ const.

Figure 5.6 shows the results from the present investigation in a form similar to that of Figure 5.2, i.e. change in mean value and amplitude of pressure at the center of the diaphragm with BR increase. Figure 5.7 focuses on the range of BR values near the one that causes vortex shedding suppression. According to them, the decrease in amplitude in that region is rather abrupt.

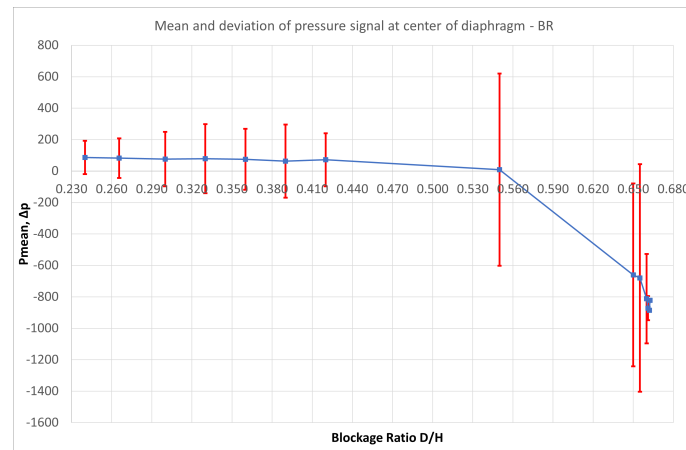


Figure 5.6. Change in mean value and amplitude of pressure at the center of the diaphragm with BR increase by the present method.

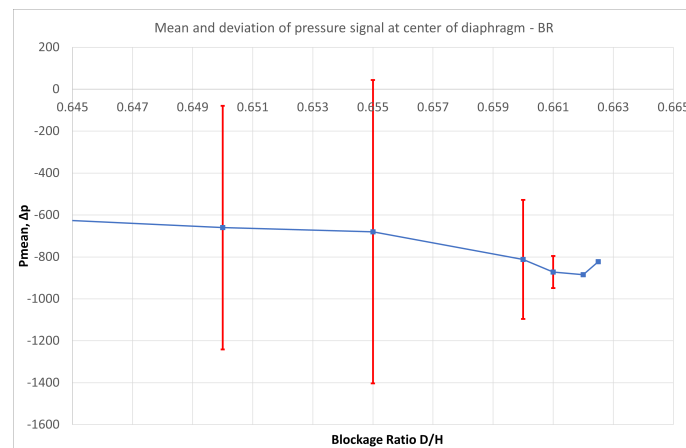


Figure 5.7. Focus on the range of BR values near that leading to vortex shedding suppression.

To further clarify the predicted behavior, Figure 5.8 plots the pressure amplitude on the center of the diaphragm as a function of BR for constant inlet velocity (i.e. the lengths of red bars in Figure 5.6). As shown in this figure, pressure amplitude increases with the increase of BR, attaining a maximum for BR=0.655. Then an abrupt decrease occurs and becomes zero for BR=0.662, in a very small region of BR increase. This behavior of attaining a maximum and then decreasing to zero is the same as that of Figure 5.2 predicted in [26]. However, this behavior is predicted for significantly greater values of BR and in a much more pronounced way, i.e. the maximum is greater than double and the decrease towards suppression is very abrupt.

In the same diagram of Figure 5.8, the corresponding change of average pressure drop in the channel with the increase of BR has been plotted. The comparative view of the two curves, namely that of pressure amplitude (for which a high value is desired) and that of pressure drop (that a high value is unwanted) may be useful for the designer. Their comparison shows that the increase in pressure amplitude due to the increase of the body width comes in the cost of about a similar pressure drop up to the value of BR=0.420. Then the two curves diverge and they come close again at BR=0.650, where amplitude becomes maximum, but drop also becomes maximum. From a designer's point of view, if these results could be validated by experiments, the value of $BR = 0.550$ seems to provide a great value of amplitude at the expense of a moderate pressure drop.

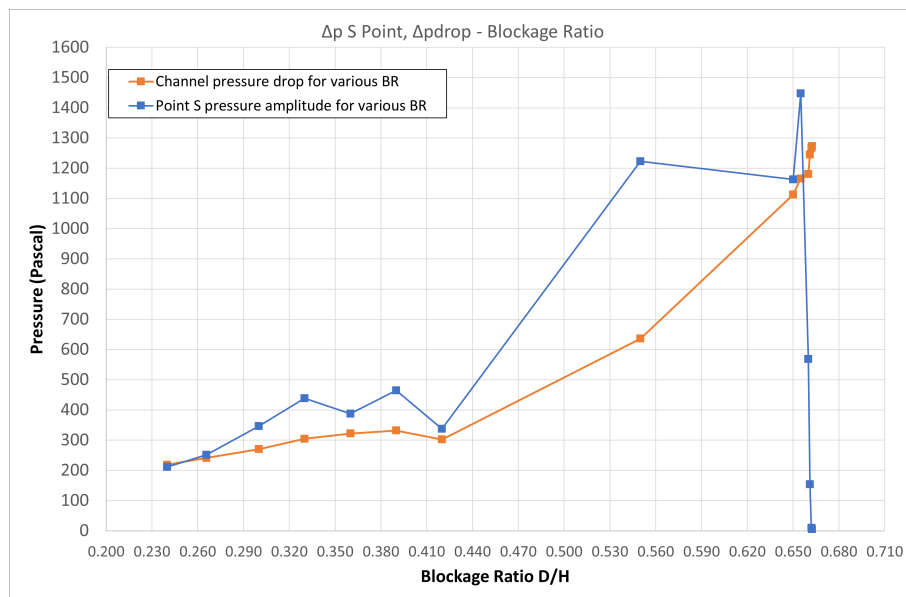


Figure 5.8. Pressure amplitude on the center of the diaphragm and average channel pressure drop as functions of BR for constant inlet velocity.

Finally, Figures 5.9 and 5.10 present the plot of the frequency and the Strouhal number, respectively, of the pressure signal at the center of the diaphragm as functions of BR for constant inlet velocity. They both follow the behavior described for the pressure amplitude, i.e. they predict vortex shedding beyond the value of BR=0.42 that becomes more intense up to the value of BR=0.655, where it is maximized and then exhibit a steep decrease.

The explanation about the difference between the present results with those of [26] is not at all obvious, since the same numerical approach has been implemented (same code, similar grids, and time step selection). In [26], neither more information about the simulations nor relevant experimental results concerning the suppression of vortex shedding, is contained.

However, for the validity of the present results, experimental evidence was found, as it is explained in what follows. In parallel with the present Diploma Thesis, another one was conducted at the same time in the University of West Attica. This concerned an experimental approach for the

device under consideration and relevant measurements about its performance. (It is the Diploma Thesis of Ioannis Matsoukas with the title “Development of an airflow measurement device employing a piezoelectric membrane and a 3D printed structure containing a piezoresistor”, under the supervision of Professor D. Pagonis [17].)

The experimentalists (Mr Matsoukas and Prof. Pagonis) were asked for a particular experiment for $V_{in} = 20.7m/s$ and $BR = 0.55$ in order to see if their measurements are compatible with the occurrence of vortex shedding in this case. The latter is well in a BR-region where the present numerical results predict vortex shedding, while in those of [26] suppression of vortex shedding has already been noticed from the value of $BR = 0.42$. The group experimentalists, after performing the desired experiment twice, using a different piezoelectric membrane each time, verified both times that the measured voltage corresponds to a flow exhibiting vortex shedding. This is considered to be a positive information concerning the quality of the present results.

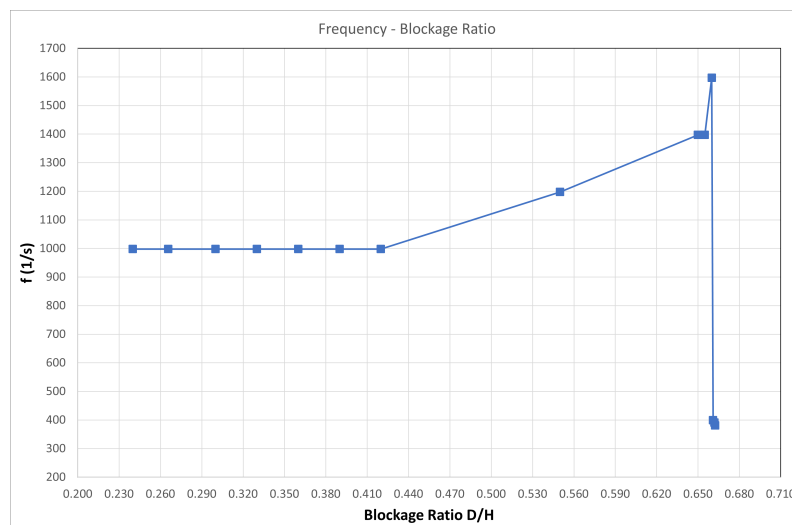


Figure 5.9. Frequency of the pressure signal at the center of the diaphragm as functions of BR for constant inlet velocity.

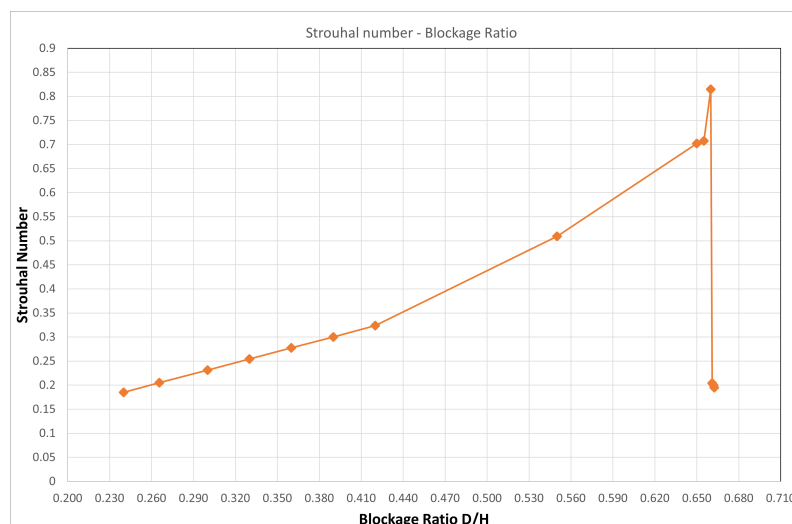


Figure 5.10. Strouhal number of the pressure signal at the center of the diaphragm as functions of BR for constant inlet velocity.

Chapter 6

Conclusions and future research

6.1 Conclusions

A CFD model, originally set up in [21] for the numerical simulation of a millimeter-scale flow energy harvesting device proposed in the literature [26], is further developed herein. The device contains two bluff bodies installed in a very small flow channel and exploits vortex shedding to cause oscillations on a flexible diaphragm above them and convert flow energy to electrical by means of the piezoelectric phenomenon. In [21], different body shapes were numerically investigated for a fixed flow Reynolds number and the achieved vortex shedding severity was assessed in terms of the unsteady pressure fluctuation. For the most efficient configuration found in [21], the study was continued herein by further testing the CFD model and performing parametric studies to understand the effect of various parameters on the expected performance of the device.

In particular, after performing the necessary grid independence study and investigation of the appropriate time step, the device performance was numerically assessed in a range of different inlet Reynolds numbers and blockage ratios. Furthermore, vortex shedding behavior with respect to blockage ratio increase was extensively studied and the critical value of BR, for which vortex shedding suppression occurs, was found. The latter was not in accordance with previous numerical results in the literature obtained by a similar method and approach. Specifically, the critical value of BR causing vortex shedding suppression was found herein to be significantly greater. The conclusions drawn in the present work are summarized in what follows.

The position of maximum pressure fluctuation amplitude (Δp_{max}) for all cases was found at a distance of $8mm$ from the beginning of the diaphragm, i.e. at point P5. This means that in order to maximize the effect of vortex shedding on the diaphragm in terms of pressure fluctuation, **the diaphragm should be placed in a way that the center is located at point P5, i.e at a length of 12mm upwind its current position.**

Δp_{max} (found at point P5) increases almost linearly with the inlet velocity for all the values of blockage ratio (BR). In particular, the greater the BR, the more abrupt the increase (greater line inclination). This means that, **the greater the inlet velocity and the greater the blockage ratio, the maximum the pressure fluctuation amplitude is.**

The fundamental frequency f of pressure evolution at point P5 increases almost linearly with the inlet velocity for all the values of blockage ratio and the inclination of the linear increase remains almost about the same for all BR. This frequency slightly decreases with the increase of BR for the same Reynolds number.

The average pressure drop (Δp_{drop}) increases with the square of inlet velocity for all values of BR. For the same inlet velocity, **pressure drop increases with BR.**

The non-dimensional quantities corresponding to Δp_{max} , f and Δp_{drop} , namely Cp_{max} , Strouhal number and Cp_{drop} , respectively, all exhibit the same behavior, i.e. they are almost constant irrespective the Reynolds number for the same value of blockage ratio. Their constant value is an

increasing function of BR. For each of these quantities, the almost constant value for each BR was found as an average among the values in the Reynolds range (for example see Figure 4.11 for Cp_{max}). Figure 6.1 presents the variation of the averaged values of Cp_{max} , St and Cp_{drop} versus BR. It clearly demonstrates that the increase in BR causes all three quantities to increase. Furthermore, it seems that the rate of increase in Cp_{max} is greater than that of Cp_{drop} , which dictates that **the increase in BR can be an efficient way to enhance the vortex-shedding effect on the piezoelectric membrane.**

The ratio of pressure fluctuation amplitude Δp_{max} (computed at the position of its maximum value, i.e. at P5) to the amplitude of pressure fluctuation at the center of the diaphragm Δp_S versus Reynolds number, was calculated for the various values of BR. The results presented in Figure 6.2 show that this ratio slightly decreases with Reynolds and for each Reynolds it increases with BR. Similarly, the ratio of the maximum pressure amplitude (at P5) to the average channel pressure drop versus Reynolds, for the various BR values, was calculated and plotted in Figure 6.3. According to this figure, the ratio slightly depends on the Reynolds number and mainly depends on BR (an increasing function of BR). The average value in the Reynolds range for the two above-presented pressure ratios was calculated for each value of BR and has been plotted in Figure 6.4. According to the information that can be extracted from this figure, Δp_{max} is in average about double the value of Δp_S (ranging from 1.4 to 2.8). The same is valid for Δp_{drop} (ranging from about 1.3 to 2.6). **This means that if the diaphragm was positioned with its center at S at point P5, the achieved pressure amplitude could be doubled.**

Contrary to a similar previous research work in the literature [26], the critical blockage ratio for which vortex shedding suppression occurs for a given inlet velocity, was found in the present study to have a significantly greater value. It has to be mentioned that this fact has been validated by corresponding experiments [17]. Based on this fact and according to Figure 5.8 the greater the BR, the greater the enhancement of Δp_S , for BR values lower than the critical one. In particular, for an increase of BR from the baseline value BR = 0.270 to BR = 0.390 (44.4% increase) the increase in Δp_S is $\approx 125\%$. However, beyond the value of BR = 0.420 that the authors in [26] claim vortex suppression to take place the increase in Δp_S is much more significant, i.e. from 0.390 to 0.550 (41% increase) the increase in Δp_S is $\approx 167\%$. By further considering the claim that $\Delta p_{max} \approx 2\Delta p_S$ it is concluded that for BR=0.550, a value of about 2400Pa could be attained if the center of the membrane was placed at point P5 (this case corresponds to Re=12473 which is outside the range studied in Figure 6.4).

As a contribution of this work, from a designer point of view, and under the prerequisite that these results would be further validated by experiments, a great BR but lower than its critical value, seems to provide a significant enhancement in pressure fluctuation amplitude in the expense of a moderate pressure drop.

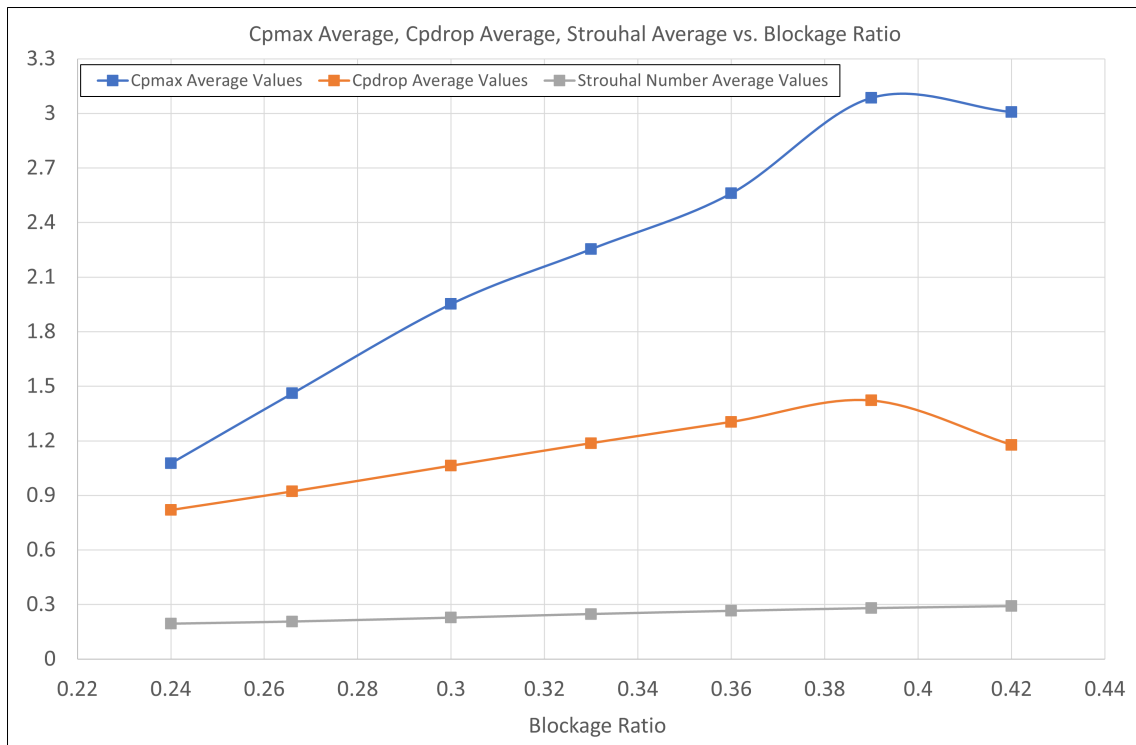


Figure 6.1. Average values of: Cp_{max} , Cp_{drop} , St with respect to Blockage Ratio

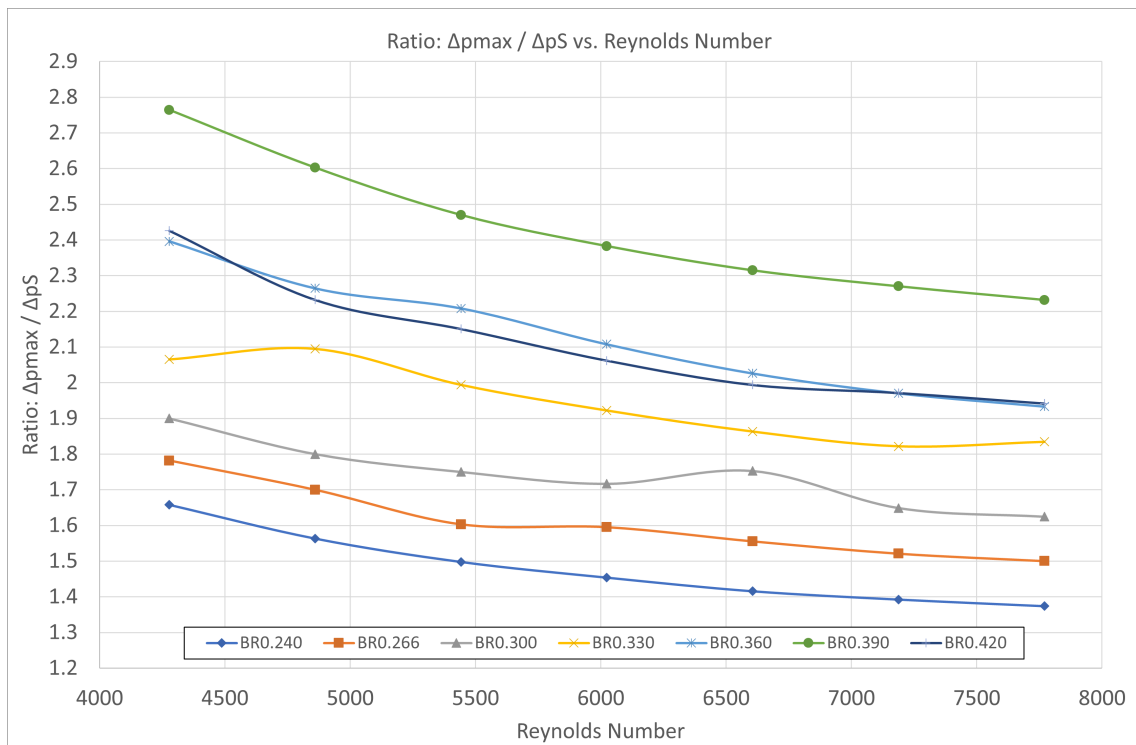


Figure 6.2. Ratio of Δp_{max} to Δp_S with respect to Reynolds Number

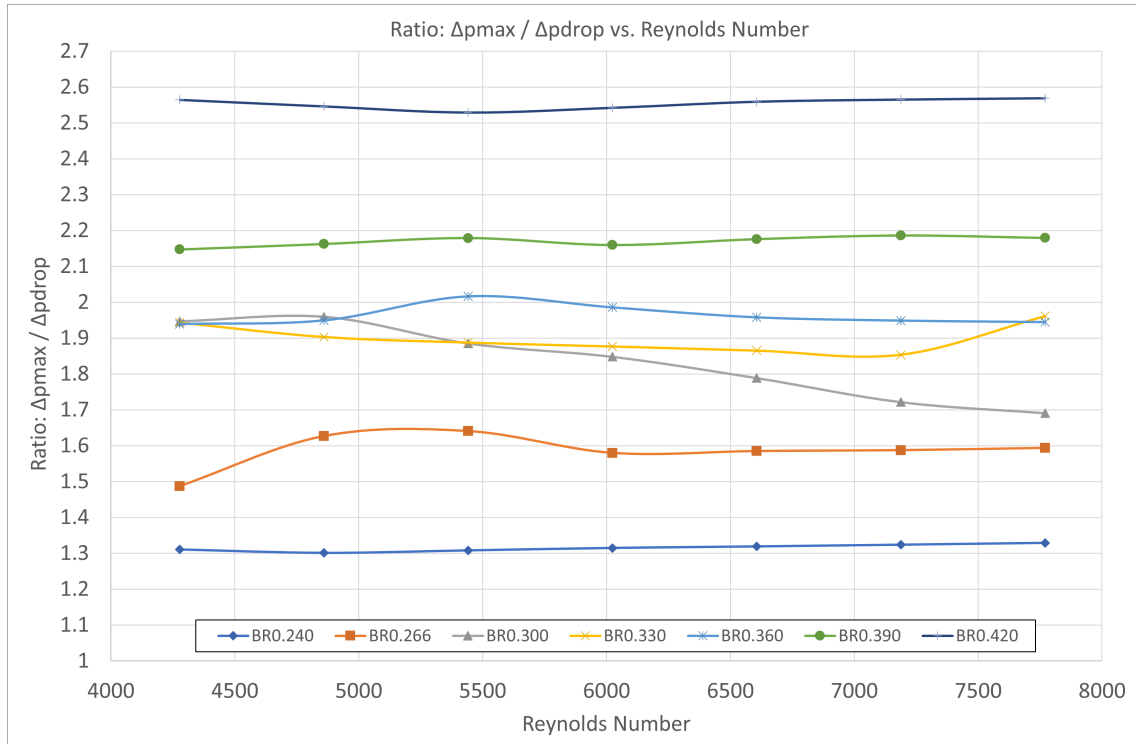


Figure 6.3. Ratio of Δp_{max} to Δp_{drop} with respect to Reynolds Number

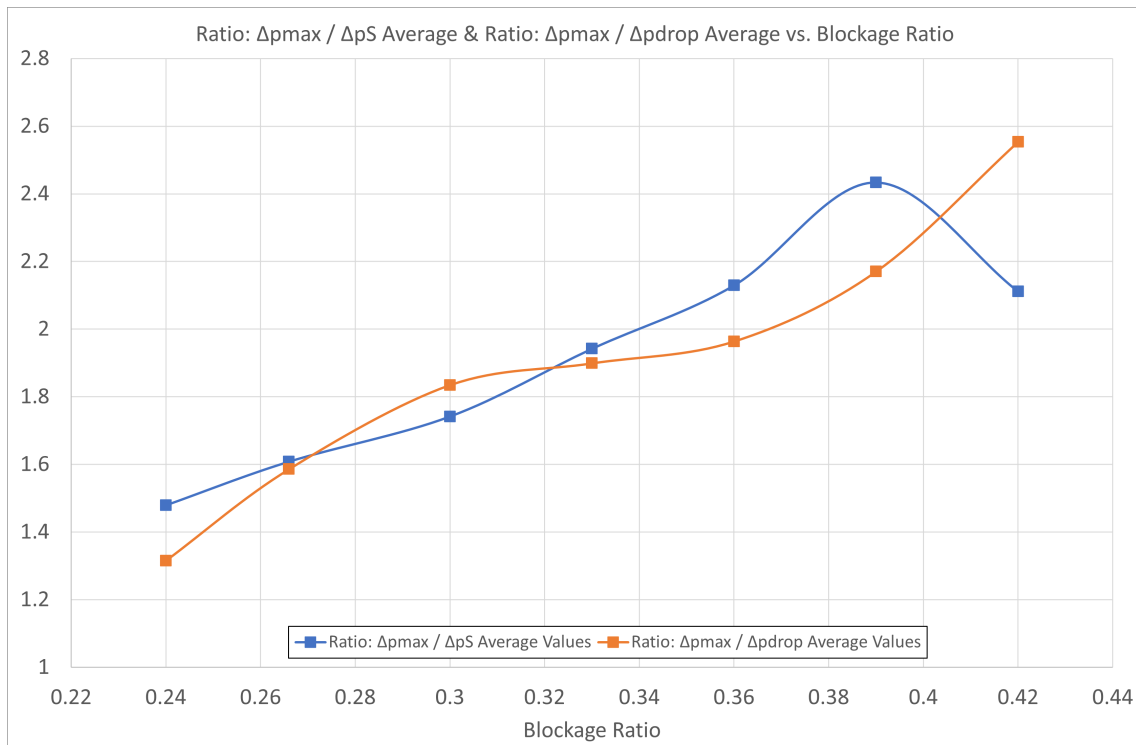


Figure 6.4. Average values of ratios: $\Delta p_{max} / \Delta p_S$ and $\Delta p_{max} / \Delta p_{drop}$, with respect to Blockage Ratio

6.2 Future research

In light of the above, aiming to further develop the research on the study and design of flow energy piezoelectric harvesting micro-devices, the following issues are proposed for ongoing and future work (continuing the present study):

- Study of vortex shedding suppression in a flow confined by the walls of a channel. To this end, more values of BR could be simulated and a more detailed curve could be plotted in Figure 5.8. This investigation should be combined with corresponding experiments for validation. The dependence of critical BR value as a function of inlet velocity could be an output of such a study.
- Study of the effect of the location and distance of the two bluff bodies on the performance of the device, since there is already experimental evidence [17] that different distance between the bodies leads to a greater pressure amplitude.
- Study of the link between pressure fluctuation amplitude and electric power production and understanding what is crucial for performance enhancement, (for example maximizing pressure amplitude in conjunction with a resonant frequency of the membrane). Possible correlations between maximum pressure fluctuation and produced voltage, i.e. the operational curve of a device using a particular membrane, could be extracted, based on combined numerical and experimental studies.
- Attempt to create a simple model for the piezoelectric phenomenon in order to correlate pressure fluctuations with the electric power (i.e. to model the actual performance of the device and assess it against experimental results).
- Perform design optimization studies with respect to characteristic geometric quantities (location and distance between the two bodies, location of the diaphragm, channel blockage ratio, etc). To this end, a stochastic-based approach could be implemented. The solution of a multiobjective problem could be sought in this case, e.g. maximization of Δp_{max} and, at the same time, minimization of Δp_{drop} . Furthermore, this could be constrained, e.g. the frequency should be in the neighborhood of the resonant frequency of the membrane.
- Perform 3D simulations and compare them against 2D simulations.
- Implementation of various turbulence models and compare their results in the case under consideration.
- Model the membrane dynamics and consider fluid-structure interaction in the simulations.

Bibliography

- [1] H. D. Akaydin, N. Elvin, and Y. Andreopoulos. “Wake of a cylinder: A paradigm for energy harvesting with piezoelectric materials.” In: *Experiments in Fluids* 49 (1 July 2010), pp. 291–304. ISSN: 07234864. DOI: [10.1007/s00348-010-0871-7](https://doi.org/10.1007/s00348-010-0871-7).
- [2] I. F. Akyildiz, W. Su, Y. Sankarasubramaniam, and E. Cayirci. “Wireless sensor networks: A survey.” In: *Computer Networks* 38 (4 Mar. 2002), pp. 393–422. ISSN: 13891286. DOI: [10.1016/S1389-1286\(01\)00302-4](https://doi.org/10.1016/S1389-1286(01)00302-4).
- [3] Giancarlo Alfonsi. “Reynolds-averaged Navier-Stokes equations for turbulence modeling.” In: *Applied Mechanics Reviews* 62 (4 July 2009), pp. 1–20. ISSN: 00036900. DOI: [10.1115/1.3124648](https://doi.org/10.1115/1.3124648).
- [4] J J Allen and A J Smits. “ENERGY HARVESTING EEL.” In: *Journal of Fluids and Structures* 15 (2001), pp. 629–640. DOI: [10.1006/j#s.2000.0355](https://doi.org/10.1006/j#s.2000.0355).
- [5] G. Altena, D. Hohlfeld, R. Elfrink, M. H. Goedbloed, and R. Van Schaijk. “Design, modeling, fabrication and characterization of an electret-based MEMS electrostatic energy harvester.” In: *2011 16th International Solid-State Sensors, Actuators and Microsystems Conference, TRANSDUCERS’11* (2011), pp. 739–742. DOI: [10.1109/TRANSDUCERS.2011.5969847](https://doi.org/10.1109/TRANSDUCERS.2011.5969847).
- [6] “ANSYS Fluent Theory Guide 15.” In: ().
- [7] “ANSYS Fluent Users Guide.” In: ().
- [8] Ahmed B. Atrah, Mohd Syuhaimi Ab-Rahman, Hanim Salleh, Mohd Zaki Nuawi, Mohd Jailani Mohd Nor, and Nordin Bin Jamaludin. “Karman vortex creation using cylinder for flutter energy harvester device.” In: *Micromachines* 8 (7 July 2017). ISSN: 2072666X. DOI: [10.3390/mi8070227](https://doi.org/10.3390/mi8070227).
- [9] Antonio Baptista et al. *Towards a multi-purpose forecast system for the Columbia River estuary Economic modeling of long-term preservation View project Cascadia Submarine Paleoseismology View project TOWARDS A MULTI-PURPOSE FORECAST SYSTEM FOR THE COLUMBIA RIVER ESTUARY*. 1998. URL: <http://www.ccalmr.orgi.edu/CORIE>.
- [10] Marios-Vasileios N Benetatos and Dimitrios G Koubogiannis. *NUMERICAL INVESTIGATION OF THE ENERGY HARVESTING POTENTIAL FROM A MICRO-CHANNEL FLOW*. 2022.
- [11] Edoardo Biagioni. “Pods: Issues in the Design of Practical Ad-Hoc Wireless Sensor Networks.” In: ().
- [12] Philippe Bonnet, Johannes Gehrke, and Praveen Seshadri. “Querying the physical world.” In: *IEEE Personal Communications* 7 (5 Oct. 2000), pp. 10–15. ISSN: 10709916. DOI: [10.1109/98.878531](https://doi.org/10.1109/98.878531).

- [13] Athanassios Boulis, Chih Chieh Han, and Mani B. Srivastava. "Design and implementation of a framework for efficient and programmable sensor networks." In: *Proceedings of the 1st International Conference on Mobile Systems, Applications and Services, MobiSys 2003* (May 2003), pp. 187–200. DOI: [10.1145/1066116.1066121](https://doi.org/10.1145/1066116.1066121).
- [14] E. Dick. "Introduction to finite volume methods in computational fluid dynamics." In: *Computational Fluid Dynamics* (2009), pp. 275–301. DOI: [10.1007/978-3-540-85056-4_11/COVER](https://doi.org/10.1007/978-3-540-85056-4_11/COVER). URL: https://link.springer.com/chapter/10.1007/978-3-540-85056-4_11.
- [15] Wendi B. Heinzelman, Amy L. Murphy, Hervaldo Sampaio Carvalho, and Mark A. Perillo. "Middleware to support sensor network applications." In: *IEEE Network* 18 (1 Jan. 2004), pp. 6–14. ISSN: 08908044. DOI: [10.1109/MNET.2004.1265828](https://doi.org/10.1109/MNET.2004.1265828).
- [16] Christopher A. Howells. "Piezoelectric energy harvesting." In: *Energy Conversion and Management* 50 (7 July 2009), pp. 1847–1850. ISSN: 01968904. DOI: [10.1016/j.enconman.2009.02.020](https://doi.org/10.1016/j.enconman.2009.02.020).
- [17] Matsoukas Ioannis. "Development of an air flow measurement device employing a piezoelectric membrane and a 3D printed structure containing a piezoresistor." University Of West Attica, Feb. 2023.
- [18] "2 - Vibration Induced by Cross-Flow." In: *Flow Induced Vibrations*. Ed. by Shigehiko Kaneko, Tomomichi Nakamura, Fumio Inada, and Minoru Kato. Amsterdam: Elsevier, 2008, pp. 29–106. ISBN: 978-0-08-044954-8. DOI: <https://doi.org/10.1016/B978-0-08-044954-8.00002-4>. URL: <https://www.sciencedirect.com/science/article/pii/B9780080449548000024>.
- [19] Nikolaos D. Katopodes. "Chapter 5 - Viscous Fluid Flow." In: *Free-Surface Flow*. Ed. by Nikolaos D. Katopodes. Butterworth-Heinemann, 2019, pp. 324–426. ISBN: 978-0-12-815489-2. DOI: <https://doi.org/10.1016/B978-0-12-815489-2.00005-8>. URL: <https://www.sciencedirect.com/science/article/pii/B9780128154892000058>.
- [20] Kamaldeep Kaur, Parneet Kaur, and Er Sharanjit Singh. *Wireless Sensor Network: Architecture, Design Issues and Applications*. URL: www.ijser.in.
- [21] Dimitrios G. Koubogiannis. "Parametric CFD study of micro-energy harvesting in a flow channel exploiting vortex shedding." In: *Open Engineering* 6 (1 2016), pp. 135–144. ISSN: 23915439. DOI: [10.1515/eng-2016-0016](https://doi.org/10.1515/eng-2016-0016).
- [22] Mauri Kuorilehto. *A Survey of Application Distribution in Wireless Sensor Networks*. 2005, pp. 774–788.
- [23] Alan Mainwaring, Joseph Polastre, Robert Szewczyk, David Culler, and John Anderson. "Wireless Sensor Networks for Habitat Monitoring." In: (2002).
- [24] Henry O. Marcy, Jonathan R. Agre, Charles Chien, Loren P. Clare, Nikolai Romanov, and Allen Twarowski. "Wireless sensor networks for area monitoring and integrated vehicle health management applications." In: *Space Technology Conference and Exposition* (1999). DOI: [10.2514/6.1999-4557](https://doi.org/10.2514/6.1999-4557). URL: <https://arc.aiaa.org/doi/10.2514/6.1999-4557>.
- [25] Robert Myers, Mike Vickers, Hyeoungwoo Kim, and Shashank Priya. "Small scale wind-mill." In: *Applied Physics Letters* 90 (5 Jan. 2007), p. 054106. ISSN: 0003-6951. DOI: [10.1063/1.2435346](https://doi.org/10.1063/1.2435346). URL: <https://aip.scitation.org/doi/abs/10.1063/1.2435346>.
- [26] Hai Dang Tam Nguyen, Huy Tuan Pham, and Dung An Wang. "A miniature pneumatic energy generator using Kármán vortex street." In: *Journal of Wind Engineering and Industrial Aerodynamics* 116 (2013), pp. 40–48. ISSN: 01676105. DOI: [10.1016/j.jweia.2013.03.002](https://doi.org/10.1016/j.jweia.2013.03.002).

- [27] Jiegang Peng, Xin Fu, and Ying Chen. “Flow measurement by a new type vortex flowmeter of dual triangulate bluff body.” In: *Sensors and Actuators, A: Physical* 115 (1 Sept. 2004), pp. 53–59. ISSN: 09244247. DOI: [10.1016/j.sna.2004.03.020](https://doi.org/10.1016/j.sna.2004.03.020).
- [28] Arian Rahimi, Özge Zorlu, Ali Muhtaroglu, and Haluk Kùlah. “A vibration-based electromagnetic energy harvester system with highly efficient interface electronics.” In: *2011 16th International Solid-State Sensors, Actuators and Microsystems Conference, TRANSDUCERS'11* (2011), pp. 2650–2653. DOI: [10.1109/TRANSDUCERS.2011.5969876](https://doi.org/10.1109/TRANSDUCERS.2011.5969876).
- [29] Kay Römer. “Tracking real-world phenomena with smart dust.” In: *Lecture Notes in Computer Science (including subseries Lecture Notes in Artificial Intelligence and Lecture Notes in Bioinformatics)* 2920 (2004), pp. 28–43. ISSN: 16113349. DOI: [10.1007/978-3-540-24606-0_3](https://doi.org/10.1007/978-3-540-24606-0_3).
- [30] Anatol Roshko. “On the Development of Turbulent Wakes from Vortex Streets.” In: (1954). URL: <https://resolver.caltech.edu/CaltechAUTHORS:ROSnacarpt1191>.
- [31] Shad Roundy, Paul K Wright, and Jan Rabaey. *A study of low level vibrations as a power source for wireless sensor nodes*. 2002. URL: www.elsevier.com/locate/comcom.
- [32] Salem Saadon and Othman Sidek. “A review of vibration-based MEMS piezoelectric energy harvesters.” In: *Energy Conversion and Management* 52 (1 Jan. 2011), pp. 500–504. ISSN: 0196-8904. DOI: [10.1016/J.ENCONMAN.2010.07.024](https://doi.org/10.1016/J.ENCONMAN.2010.07.024).
- [33] L. Schwiebert, S. K.S. Gupta, and J. Weinmann. “Research challenges in wireless networks of biomedical sensors.” In: *Proceedings of the Annual International Conference on Mobile Computing and Networking, MOBICOM* (2001), pp. 151–165. DOI: [10.1145/381677.381692](https://doi.org/10.1145/381677.381692). URL: <https://dl.acm.org/doi/10.1145/381677.381692>.
- [34] C. C. Shen, C. Srisathapornphat, and C. Jaikao. “Sensor information networking architecture and applications.” In: *IEEE Personal Communications* 8 (4 Aug. 2001), pp. 52–59. ISSN: 10709916. DOI: [10.1109/98.944004](https://doi.org/10.1109/98.944004).
- [35] Nathan S. Shenck and Joseph A. Paradiso. “Energy scavenging with shoe-mounted piezoelectrics.” In: *IEEE Micro* 21 (3 May 2001), pp. 30–42. ISSN: 02721732. DOI: [10.1109/40.928763](https://doi.org/10.1109/40.928763).
- [36] Geeng Jen Sheu, Shih Ming Yang, and Tehsi Lee. “Development of a low frequency electrostatic comb-drive energy harvester compatible to SoC design by CMOS process.” In: *Sensors and Actuators, A: Physical* 167 (1 May 2011), pp. 70–76. ISSN: 09244247. DOI: [10.1016/j.sna.2010.07.013](https://doi.org/10.1016/j.sna.2010.07.013).
- [37] Yi Chung Shu. *Performance evaluation of vibration-based piezoelectric energy scavengers*. 2009. DOI: [10.1007/978-0-387-76464-1_3](https://doi.org/10.1007/978-0-387-76464-1_3).
- [38] Othman Sidek, Muhammad Afif Khalid, Mohammad Zulfikar Ishak, and Muhamad Azman Miskam. “Design and simulation of SOI-MEMS electrostatic vibration energy harvester for micro power generation.” In: 2011, pp. 207–212. ISBN: 9781612842288. DOI: [10.1109/INECCE.2011.5953877](https://doi.org/10.1109/INECCE.2011.5953877).
- [39] Shuyu Sun and Tao Zhang. “Introduction.” In: *Reservoir Simulations* (Jan. 2020), pp. 1–22. DOI: [10.1016/B978-0-12-820957-8.00001-0](https://doi.org/10.1016/B978-0-12-820957-8.00001-0).
- [40] S. R. Kamel Tabbakh, R. Maarefdoust, Ng Chee Kyun, and B. Mohd Ali. “Environmental taxonomy of power scavenging techniques for autonomous self powered wireless sensors.” In: *IEEE Asia-Pacific Conference on Circuits and Systems, Proceedings, APCCAS* (2010), pp. 1031–1034. DOI: [10.1109/APCCAS.2010.5774812](https://doi.org/10.1109/APCCAS.2010.5774812).

- [41] Y. K. Tan and S. K. Panda. “A novel piezoelectric based wind energy harvester for low-power autonomous wind speed sensor.” In: *IECON Proceedings (Industrial Electronics Conference)* (2007), pp. 2175–2180. DOI: [10.1109/IECON.2007.4460120](https://doi.org/10.1109/IECON.2007.4460120).
- [42] Yen Kheng Tan and Sanjib Kumar Panda. *Review of Energy Harvesting Technologies for Sustainable Wireless Sensor Network 15 0 Review of Energy Harvesting Technologies for Sustainable Wireless Sensor Network*. URL: www.intechopen.com.
- [43] Liaosha Tang, Michael P. Païdoussis, and Jin Jiang. “Cantilevered flexible plates in axial flow: Energy transfer and the concept of flutter-mill.” In: *Journal of Sound and Vibration* 326 (1-2 Sept. 2009), pp. 263–276. ISSN: 0022460X. DOI: [10.1016/j.jsv.2009.04.041](https://doi.org/10.1016/j.jsv.2009.04.041).
- [44] K. Tao, G. Ding, P. Wang, Z. Yang, and Y. Wang. “Fully integrated micro electromagnetic vibration energy harvesters with micro-patterning of bonded magnets.” In: *Proceedings of the IEEE International Conference on Micro Electro Mechanical Systems (MEMS)* (2012), pp. 1237–1240. ISSN: 10846999. DOI: [10.1109/MEMSYS.2012.6170413](https://doi.org/10.1109/MEMSYS.2012.6170413).
- [45] Kuniyoshi Tashiro, Hiroyuki Wakiwaka, Shin Ichiro Inoue, and Yu Uchiyama. “Energy harvesting of magnetic power-line noise.” In: *IEEE Transactions on Magnetics* 47 (10 2011), pp. 4441–4444. ISSN: 00189464. DOI: [10.1109/TMAG.2011.2158190](https://doi.org/10.1109/TMAG.2011.2158190).
- [46] George W Taylor, Joseph R Burns, Sean M Kammann, William B Powers, and Thomas R Welsh. *The Energy Harvesting Eel: A Small Subsurface Ocean/River Power Generator*. 2001, p. 539.
- [47] D. Vatansever, R. L. Hadimani, T. Shah, and E. Siores. “An investigation of energy harvesting from renewable sources with PVDF and PZT.” In: *Smart Materials and Structures* 20 (5 May 2011). ISSN: 09641726. DOI: [10.1088/0964-1726/20/5/055019](https://doi.org/10.1088/0964-1726/20/5/055019).
- [48] A. Venugopal, Amit Agrawal, and S. V. Prabhu. “Influence of blockage and shape of a bluff body on the performance of vortex flowmeter with wall pressure measurement.” In: *Measurement: Journal of the International Measurement Confederation* 44 (5 June 2011), pp. 954–964. ISSN: 02632241. DOI: [10.1016/j.measurement.2011.02.015](https://doi.org/10.1016/j.measurement.2011.02.015).
- [49] R. J.M. Vullers, R. van Schaijk, I. Doms, C. Van Hoof, and R. Mertens. “Micropower energy harvesting.” In: *Solid-State Electronics* 53 (7 July 2009), pp. 684–693. ISSN: 00381101. DOI: [10.1016/j.sse.2008.12.011](https://doi.org/10.1016/j.sse.2008.12.011).
- [50] Dung An Wang and Nine Zeng Liu. “A shear mode piezoelectric energy harvester based on a pressurized water flow.” In: *Sensors and Actuators, A: Physical* 167 (2 June 2011), pp. 449–458. ISSN: 09244247. DOI: [10.1016/J.SNA.2011.03.003](https://doi.org/10.1016/J.SNA.2011.03.003).
- [51] Stephen S. Yau, Fariaz Karim, Wang Yu, Wang Bin, and Sandeep K.S. Gupta. “Reconfigurable Context-Sensitive Middleware for pervasive computing.” In: *IEEE Pervasive Computing* 1 (3 2002), pp. 33–40. ISSN: 15361268. DOI: [10.1109/MPRV.2002.1037720](https://doi.org/10.1109/MPRV.2002.1037720).
- [52] Gongbo Zhou, Linghua Huang, Wei Li, and Zhencai Zhu. *Harvesting ambient environmental energy for wireless sensor networks: A survey*. 2014. DOI: [10.1155/2014/815467](https://doi.org/10.1155/2014/815467).
- [53] Dibin Zhu, Steve Beeby, John Tudor, Neil White, and Nick Harris. *A Novel Miniature Wind Generator for Wireless Sensing Applications*.
- [54] Özge Zorlu, Emre Tan Topal, and Haluk Külah. “A vibration-based electromagnetic energy harvester using mechanical frequency up-conversion method.” In: *IEEE Sensors Journal* 11 (2 2011), pp. 481–488. ISSN: 1530437X. DOI: [10.1109/JSEN.2010.2059007](https://doi.org/10.1109/JSEN.2010.2059007).